Naval Information Warfare Center
PACIFIC

Wideband HF Surface-Wave Channels: Measurements to Fading Models

Erica Daly
Michael Daly
John Meloling
Jake Rissmiller
Jeffery C. Allen

NIWC Pacific
San Diego, CA 92152

10-April-2023

DISTRIBUTION STATEMENT A. Approved for public release: distribution unlimited.

Naval Information Warfare Center Pacific (NIWC Pacific)
San Diego, CA 92152-5001

Signatures

ALLEN.JEFFERY.C.1231835268

Digitally signed by ALLEN.JEFFERY.C.1231835268
Date: 2023.05.23 13:18:59 -07'00'

DALY.MICHAEL.PATRICK.1394627689

Digitally signed by DALY.MICHAEL.PATRICK.1394627689
Date: 2023.05.24 08:25:42 -07'00'

Executive Summary

This report analyzes High-Frequency (HF) ship-to-shore surface-wave channels measured off the coast of San Diego, California during the first week of June 2020. The results break across theory and experiment for surface-wave identification, modeling, analysis, and propagation.

Surface-Wave Identification: This report *identifies* the surface-wave channels as Rician so that the received signal $\{s_R(t)\}$ is a *delayed* and *faded* copy of the transmitted signal $\{s_T(t)\}$:

$$s_R(t) = h(t)s_T(t - \tau_G), \tag{1}$$

where τ_G denotes the *delay* between transmitter and receiver and the fading $\{h(t)\}$ is *Rician*:

$$h(t) = e^{j2\pi f_D t}\left\{s_{\mathsf{LOS}} + g(t)\right\}. \tag{2}$$

The linear *Doppler shift* f_D modulates both the strong *specular component* s_{LOS} and the weaker *diffuse component* $\{g(t)\}$ that is a Gaussian random process. This Rician fading is a credible surface-wave fading model for HF networks operating on the sea surface with distances limited to 200 km.

Surface-Wave Modeling: This report *parameterizes* the Rician fading measured in these surface-wave channels. The table to the right lists typical Rician fading parameters extracted from these measurements and listed in the *HF Channel Emulator User's Manual* [78]. This surface-wave fading supports testing a single HF link using the HF Channel Emulator. This report *recommends* combining this surface-wave fading with surface-wave propagation (See Appendix C) and HF shipboard noise measurements [36] to emulate an HF network operating on the sea surface. This report *recommends* documenting the technical details of this surface-wave HF network in the *HF Channel Emulator's Technical Report* [77].

05-June-2020 21:35 UTC; 4.23 MHz	
Rician Parameters	**Ray # 1**
Delay	0.56 (ms)
RMS Bandwidth	3.8 (Hz)
Rician *K* Factor	21 (dB)
Relative Power	0 (dB)
Doppler Shift	0.0635 (Hz)
Doppler Shift Variation	0 (Hz/sec)

Surface-Wave Analysis: This report develops three Rician estimators to *extract* the fading observed in the measurements. The biggest gap between the theory and measurements is the diffuse process $\{g(t)\}$. Standard Rician fading and the Rician estimators assume the diffuse process has power spectrum

$$P_{gg}(f) \sim \exp\left(-\frac{f^2}{2f_{\mathsf{RMS}}^2}\right)$$

parameterized by the RMS bandwidth f_{RMS}. Although low-noise measurements show this Gaussian spectrum, this spectrum does not model high-noise measurements. This report *recommends* deriving the diffuse power spectrum from the propagation over the sea surface. This physics-based derivation should explain the diffuse spectrum's transition from the Gaussian shape observed in the low frequencies to the unknown spectral shape observed in the higher frequencies.

Surface-Wave Propagation: This report compares the surface-wave measurements to selected *surface-wave propagation* codes. This comparison is limited by the gaps in the soundings caused by the ship's operations, the unknown antennas patterns, and calibrations. This report *recommends* low-cost experiments comparing surface-wave measurements to theoretical predictions generated by propagation codes. These experiments encompass ship-to-ship and ship-to-shore links associated with littoral operations. The propagation codes must encompass mixed paths, the reflection region (See Figure 1) and the over-the-horizon region (See Figure 2). These experiments benchmark mission planning using the HF surface-wave channels.

Organization: Section 1 defines the surface wave and reviews surface-wave modeling. Section 2 describes the channel sounding: transmitter, receiver, and signal processing. Section 3 presents a channel analysis template. This template eliminates repetitive text when discussing each day's experiments. Section 4 contains the channel analysis. Each day's experiment is analyzed and the surface-wave fading channels are tabulated at the end of each section. Section 5 summarizes the fading analysis and emphasizes the need for a physics-based fading model rather than identification based only measurements.

Appendices: Rician fading and estimators are reviewed in Appendix A. Appendix B archives the technical computations for the Rician estimators. Appendix C compares surface-wave propagation codes to the received power at selected ship locations. Because the antennas are not calibrated, only relative comparisons between frequencies are possible. To the first order, both theory and measurements show the correct ordering: increasing frequency increases transmission loss; increasing range increases transmission loss. However, measurements show greater relative loss than the propagation codes using standard salinity and and sea states. Therefore, a low-cost propagation experiment using calibrated antennas, sea-state information, and recording shipboard noise is proposed. The payoffs from this experiment enable network emulation of surface vessels connected by their time-varying HF surface-wave channels.

Acknowledgments

Support by John Waterston, Program Sponsor of DARPA's *Ocean of Things Program*, is acknowledged. Support from Patrick Earley and Leslie Bolick from NIWC Pacific is also acknowledged. Permission from the ITU is acknowledged to use [32, Figure 1]. Permission from Frank Ryan is acknowledged to use [56, Figure 6]. Discussions with Anirudha Suripuram, NIWC Pacific, are gratefully acknowledged. Encouragement by Michael Daly, NIWC Pacific, to include surface-wave propagation is also acknowledged. The substantial review by David Hurdsman, NIWC Pacific, upgraded this report.

Contents

Signatures i

Executive Summary ii

Acknowledgments iv

1 Surface-Wave Preliminaries 1

2 Transmitter, Receiver, Signal Processing 5
2.1 Transmitter at NIWC . . . 6
2.2 Shipboard Receiver . . . 8
2.3 Channel Sounding . . . 11
2.3.1 PN Signal . . . 11
2.3.2 HF Channel . . . 11
2.3.3 Inverse Filter . . . 12

3 A Fading Analysis Template 13
3.1 Power-Delay Profile . . . 14
3.2 Rician Fading . . . 15
3.3 Rician Estimators . . . 16
3.4 Rician Parameters . . . 17
3.5 Rician Spectrum . . . 19
3.6 Rician Simulations . . . 22

4 Soundings 29
4.1 01-June-2020 . . . 30
4.1.1 4.23 MHz . . . 34
4.1.2 8.456 MHz . . . 38
4.1.3 12.45 MHz . . . 43
4.1.4 18.474 MHz . . . 46
4.1.5 23.1 MHz . . . 49
4.1.6 Discussion . . . 53
4.2 02-June-2020 . . . 56
4.2.1 4.23 MHz . . . 60
4.2.2 8.456 MHz . . . 65
4.2.3 12.45 MHz . . . 69
4.2.4 18.474 MHz . . . 69
4.2.5 23.1 MHz . . . 69
4.2.6 Discussion . . . 73
4.3 04-June-2020 . . . 75

4.4 05-June-2020 . . . 79
4.4.1 4.23 MHz . . . 82
4.4.2 8.456 MHz . . . 84
4.4.3 12.45 MHz . . . 86
4.4.4 18.474 MHz . . . 88
4.4.5 23.1 MHz . . . 88
4.4.6 Discussion . . . 88
4.5 06-June-2020 . . . 90
4.5.1 4.23 MHz . . . 93
4.5.2 8.456 MHz . . . 95
4.5.3 12.45 MHz . . . 97
4.5.4 18.474 MHz . . . 99
4.5.5 23.1 MHz . . . 99
4.5.6 Discussion . . . 99

5 Conclusions 101

References 104

A Rician Fading and Estimation 111
A.1 Envelope Power . . . 112
A.2 Doppler Shift . . . 113
A.3 Rician K Factor . . . 114
A.3.1 Moments . . . 114
A.3.2 Histogram . . . 114
A.3.3 Maximum-Likelihood . . . 117
A.3.4 Filtering . . . 118
A.4 RMS Bandwidth . . . 121
A.4.1 Moments . . . 121
A.4.2 Level Crossings . . . 122

B Gaussian Notebook 124
B.1 Doppler Moment . . . 126
B.2 K Factor Moments . . . 127
B.3 RMS Bandwidth Moment . . . 129

C Propagation: theory and measurements 131
C.1 Transmit Antenna Modeling . . . 134
C.2 Receive Antenna Modeling . . . 135
C.3 05-June-2020 . . . 136
C.3.1 LFMFSmoothEarth . . . 137

C.3.2 Booker-Lugannani 138
C.3.3 AREPS 141
C.4 06-June-2020 143
C.4.1 LFMFSmoothEarth 143
C.4.2 FCCGW 144
C.5 Reconciling Theory and Measurements 145
C.6 The Surface Wave in Context 147

List of Figures

1 LOS Region at HF: Ray trace model; skywaves omitted. 1
2 BLOS Region at HF: Surface wave propagation beyond the horizon; skywaves omitted. Adapted from [35]. 2
3 Surface-wave propagation at 3, 10, 30 MHz; Propagation from vertically polarized monopoles [33, Figure 1], [24], [74]. 3
4 Losses along the radio circuit [32, Figure 1] (Reproduced with the ITU's permission). 4
5 *Acoustic Explorer's* track on 03-June-2020. 5
6 Land-based transmitter schematic. 6
7 Elevation patterns (dBi) for the TCI-619 operating in low-angle mode over a perfect earth (Courtesy of TCI). 6
8 Transmitter kit. 7
9 Transmitter's antenna on Building 40, NIWC Pacific. 7
10 Shipboard receiver schematic. 8
11 Receiver kit on the *Acoustic Explorer*. 9
12 The *Acoustic Explorer*. 9
13 The HF receive antenna mounted on *Acoustic Explorer*. 10
14 Block diagram showing the PN signal sounding the channel and the inverse filter extracting the channel. 11
15 Power-delay profile on 02-June-2020 06:02:01 UTC at 12.45 MHz. . 14
16 Fading phase on 02-June-2020 06:02:01 UTC at 12.45 MHz. 15
17 Fading on 02-June-2020 06:02:01 UTC at 12.45 MHz. 17
18 Histogram and Rician estimates; 02-June-2020 06:02:01 UTC at 12.45 MHz; Rician estimates overlay. 18
19 Fading spectrum on 02-June-2020 06:02:01 UTC at 12.45 MHz; $\widehat{K} =$ 18.6 dB; $\widehat{f}_{\mathsf{RMS}} = 1.15$ Hz. 20
20 HF skywave's power spectrum models. 21
21 Synthetic Rician Fading; amplitude and phase; $f_{\mathsf{RMS}} = 1.15$ Hz. . . 22
22 Synthetic Rician Fading; complex phase; $f_{\mathsf{RMS}} = 1.15$ Hz. 23
23 Synthetic Rician Fading; power spectrum; $f_{\mathsf{RMS}} = 1.15$ Hz. 24
24 Synthetic Rician Fading; amplitude and phase; $f_{\mathsf{RMS}} = 0.1$ Hz. . . 25
25 Synthetic Rician Fading; complex phase; $f_{\mathsf{RMS}} = 0.1$ Hz. 26
26 Synthetic Rician Fading; power spectrum; $f_{\mathsf{RMS}} = 0.1$ Hz. 27
27 Fading spectrum on 01-June-2020 23:57 UTC at 12.45 MHz; $\widehat{K} =$ 26.1 dB; $\widehat{f}_{\mathsf{RMS}} = 0.355$ Hz. 28
28 *Acoustic Explorer's* track on 01-June-2020. 30
29 Spectrograms on 01-June-2020. 31
30 Delay spread functions on 01-June-2020. 32

31 *Acoustic Explorer's* annotated track on 01-June-2020. The transmitter's location is marked with the circle in the upper right. 33
32 Power-delay profile on 01-June-2020 23:55 UTC at 4.23 MHz. . . . 34
33 Fading on 01-June-2020 23:55 UTC at 4.23 MHz. 35
34 Fading phase on 01-June-2020 23:55 UTC at 4.23 MHz showing forward and backward rotations. 35
35 Histograms and Rician estimates; 01-June-2020 23:55 UTC at 4.23 MHz. 36
36 Fading spectrum on 01-June-2020 23:56 UTC at 4.23 MHz. 37
37 Power-delay profile on 01-June-2020 23:56 UTC at 8.456 MHz . . . 38
38 Fading on 01-June-2020 23:56 UTC at 8.456 MHz. 39
39 Histogram and Rician estimates; 01-June-2020 23:56 UTC at 8.456 MHz. 40
40 Fading phase on 01-June-2020 23:56 UTC at 8.456 MHz. 40
41 Fading spectrum on 01-June-2020 23:56 UTC at 8.456 MHz. 41
42 Close-up of the diffuse spectrum on 01-June-2020 23:56 UTC at 8.456 MHz. The red curve is a Gaussian fitted by hand. 42
43 Power-delay profile on 01-June-2020 23:57 UTC at 12.456 MHz. . . 43
44 Fading on 01-June-2020 23:57 UTC at 12.456 MHz. 44
45 Histogram and Rician estimates; 01-June-2020 23:57 UTC at 12.456 MHz; Rician estimates overlay. 44
46 Fading phase on 01-June-2020 23:57 UTC at 12.45 MHz 45
47 Fading spectrum on 01-June-2020 23:57 UTC at 12.45 MHz 45
48 Power-delay profile on 01-June-2020 23:58 UTC at 18.474 MHz. . . 46
49 Fading on 01-June-2020 23:58 UTC at 18.474 MHz. 47
50 Fading spectrum on 01-June-2020 23:58 UTC at 18.474 MHz. . . . 47
51 Histogram and Rician estimates; 01-June-2020 23:58 UTC at 18.474 MHz; Rician estimates overlay. 48
52 Fading phase on 01-June-2020 23:58 UTC at 18.474 MHz. 48
53 Power-delay profile on 01-June-2020 23:59 UTC at 23.1 MHz. . . . 49
54 Fading on 01-June-2020 23:59 UTC at 23.1 MHz. 50
55 Fading spectrum on 01-June-2020 23:59 UTC at 23.1 MHz. 50
56 Fading densities on 01-June-2020 23:59 UTC at 23.1 MHz; Rician estimates almost overlay. 51
57 Histogram and Rician estimates; 01-June-2020 23:59 UTC at 23.1 MHz. 52
58 *Acoustic Explorer's* track on 02-June-2020. 56
59 Spectrograms measured on 02-June-2020. 57
60 Delay spread functions measured on 02-June-2020. 58

61 *Acoustic Explorer's* annotated track on 02-June-2020. Transmitter is the circle in the upper right. 59
62 Power-delay profile on 02-June-2020 06:00 UTC at 4.23 MHz. . . . 60
63 Ionogram at Point Arguello, CA; 02-June-2020 at 06:00 UTC. . . . 61
64 Fading on 02-June-2020 06:00 UTC at 4.23 MHz. 62
65 Fading spectrum on 02-June-2020 06:00 UTC at 4.23 MHz. 63
66 Histogram and Rician estimates; 02-June-2020 06:00 UTC at 4.23 MHz; Rician estimates overlay. 64
67 Fading phase on 02-June-2020 06:01 UTC at 4.23 MHz. 64
68 Power-delay profile on 02-June-2020 06:01:01 UTC at 8.446 MHz. . 65
69 Fading on 02-June-2020 06:01:01 UTC at 8.446 MHz. 66
70 Fading spectrum on 02-June-2020 06:01:01 UTC at 8.456 MHz. . . 66
71 Histogram and Rician estimates; 02-June-2020 06:01:01 at 8.456 MHz; Rician estimates almost overlay. 67
72 Fading phase on 02-June-2020 06:01 UTC at 8.456 MHz. 68
73 Power-delay profile on 02-June-2020 06:04 UTC at 23.10 MHz. . . . 69
74 Fading on 02-June-2020 06:04 UTC at 23.1 MHz. 70
75 Fading spectrum on 02-June-2020 06:04 UTC at 23.1 MHz 71
76 Histogram and Rician estimates; 02-June-2020 06:04 UTC at 23.1 MHz; Rician estimates almost overlay. 72
77 Fading phase at 23.1 MHz on 02-June-2020 06:04 UTC. 72
78 *Acoustic Explorer's* track on 04-June-2020. 75
79 Spectrograms on 04-June-2020. 76
80 *Acoustic Explorer's* annotated track on 04-June-2020. Transmitter is the circle in the upper right. 77
81 Power-delay profile on 04-June-2020 03:00 UTC at 4.23 MHz 78
82 Ionogram at Point Arguello, CA; 04-June-2020 03:00 UTC. 78
83 *Acoustic Explorer's* track on 05-June-2020. 79
84 Delay spreads on 05-June-2020. 80
85 *Acoustic Explorer's* annotated track on 05-June-2020. Transmitter is the circle in the upper right. 81
86 Power-delay profile on 05-June-2020 21:35 UTC at 4.23 MHz. . . . 82
87 Fading summary on 05-June-2020 21:35 UTC at 4.23 MHz. 83
88 Power-delay profile on 05-June-2020 21:36 UTC at 8.456 MHz. . . . 84
89 Fading summary on 05-June-2020 21:36 UTC on 8.456 MHz. 85
90 Power-delay profile on 05-June-2020 21:37 UTC at 12.45 MHz. . . . 86
91 Fading summary on 05-June-2020 21:37 UTC at 12.45 MHz. 87
92 *Acoustic Explorer's* track on 06-June-2020. 90
93 Spectrograms at 4.23, 8.456, and 12.45 MHz on 06-June-2020. . . . 91
94 Delay spread functions at 4.23, 8.456, and 12.45 MHz on 06-June-2020. 91

95 *Acoustic Explorer's* annotated track on 06-June-2020. Transmitter is the circle in the upper right. 92
96 Power-delay profile on 06-June-2020 05:05:00 UTC at 4.23 MHz. . . 93
97 Fading summary on 06-June-2020 05:05 UTC at 4.23 MHz. 94
98 Power-delay profile on 06-June-2020 05:06 UTC at 8.456 MHz. . . . 95
99 Fading summary on 06-June-2020 05:06 UTC at 8.456 MHz. 96
100 Power-delay profile on 06-June-2020 05:05:07 UTC at 12.45 MHz. . 97
101 Fading summary on 06-June-2020 05:07 UTC at 12.45 MHz. 98
102 Trends in the ship velocity computed from the Doppler shifts. . . . 102
103 Shipboard HF Networks: Mesh → Relay → Disconnect. 103
104 Surface-wave propagation at 3, 10, 30 MHz; Propagation from vertically polarized monopoles [33, Figure 1]. 103
105 Doppler shift estimates $\widehat{f_D}$ as a function of K for envelope power $p_E = 0$ dB and RMS bandwidth $f_N = 10$ Hz. 113
106 Performance of the moment estimator of $\widehat{K}$ as a function of K and RMS bandwidths f_N for the envelope power $p_E = 0$ dB and $f_D = 5$ Hz. 115
107 Performance of the Histogram estimator of $\widehat{K}$ as a function of K and RMS bandwidths f_N for the envelope power $p_E = 0$ dB and $f_D = 5$ Hz. 116
108 Performance of the p_E-constrained maximum-likelihood estimator of $\widehat{K}$ as a function of K and RMS bandwidths f_N for the envelope power $p_E = 0$ dB and $f_D = 5$ Hz. 118
109 Performance of the f_D-filter estimate $\widehat{K}$ as a function of K and RMS bandwidths f_N for envelope power $p_E = 0$ dB and $f_D = 5$ Hz. . . . 120
110 Moment estimator's performance for $\widehat{f_N}$ as a function of K and RMS bandwidths f_N for envelope power $p_E = 0$ dB and $f_D = 5$ Hz. 121
111 Rician level-crossing performance for $\widehat{f_N}$ as a function of K and RMS bandwidths f_N for envelope power $p_E = 0$ dB and $f_D = 5$ Hz. 123
112 TCI Model 619 antenna gain; interpolated from Table 17. 134
113 Shipboard receive antenna gain; monopole model. 135
114 Comparing LFMFSmoothEarth (curves) to relative Day 05 measurements (circles). 137
115 Comparing $L_g^{(1)}(f, r)$ predictions (curves) to Day 05 measurements (circles). 139
116 Additional transmission loss $L_g^{(2)}(f, r)$ caused by the rough ocean surface; Phillips spectrum. 140
117 Additional transmission loss $L_g^{(2)}(f, r)$ caused by the rough ocean surface; Neumann-Person spectrum; direction of propagation is parallel to the wind. 140

118 AREPS propagation loss at 12.450 MHz along 248.9° azimuth from the transmitter located on Building 40, NIWC. 141
119 AREPS transmission loss along 248.9° azimuth starting from the transmitter located on Building 40, NIWC to a shipboard receive antenna $h_R = 21$ feet above the sea surface. 142
120 Comparing LFMFSmoothEarth (curves) to relative Day 06 measurements (circles). 143
121 Comparing FCCGW (curves) to Day 06 measurements (circles). . . 144
122 Surface-wave diffraction from an incident ray. 147
123 HF propagation at 8 MHz; keyhole antenna (Permission courtesy of Frank Ryan [56]). 148

List of Tables

1 Surface-wave fading; 05-June-2020 at 21:35:00 UTC. 29
2 Rician fading estimates on 01-June-2020 23:55:00 UTC; 4.23 MHz. . 54
3 Rician fading estimates on 01-June-2020 23:56:00 UTC; 8.456 MHz. 54
4 Rician fading estimates on 01-June-2020 23:57:00 UTC; 12.45 MHz. 55
5 Rician fading estimates on 01-June-2020 23:58:00 UTC; 18.474 MHz. 55
6 Rician fading estimates on 01-June-2020 23:59:00 UTC; 23.1 MHz. . 55
7 Rician fading estimates on 02-June-2020 06:00:00 UTC; 4.23 MHz. . 74
8 Rician fading estimates on 02-June-2020 06:01:01 UTC; 8.456 MHz. 74
9 Rician fading estimates on 02-June-2020 06:02:01 UTC; 12.45 MHz. 74
10 Rician fading estimates on 02-June-2020 06:04:01 UTC; 23.1 MHz. . 74
11 Rician fading estimates on 05-June-2020 21:35:00 UTC; 4.23 MHz. . 89
12 Rician fading estimates on 05-June-2020 21:36:00 UTC; 8.456 MHz. 89
13 Rician fading estimates on 05-June-2020 21:37:00 UTC; 12.45 MHz. 89
14 Rician fading estimates on 06-June-2020 05:05:00 UTC; 4.23 MHz. . 100
15 Rician fading estimates on 06-June-2020 05:06:00 UTC; 8.456 MHz. 100
16 Rician fading estimates on 06-June-2020 05:07:00 UTC; 12.45 MHz. 100
17 TCI Model 619; low-angle mode [68]. 134

1 Surface-Wave Preliminaries

This section reviews surface-wave propagation to discuss these shore-to-ship experiments. The *surface-wave* definition is extracted from Norton [42]:

> "The ground wave is that component of the total received field which has not been reflected (or scattered) from either the ionosphere or the troposphere. It is convenient to divide the ground wave into two components: a space wave and a surface wave. The space wave is the sum of a direct wave and a ground-reflected wave."

Norton's definition splits ground-wave propagation into the *Line-of-Sight* (LOS) region and the *Beyond Line-of-Sight* (BLOS) region.

LOS Region: Figure 1 illustrates these ground wave components in a ray trace model over a flat earth. The *direct* and *reflected* waves travel between the elevated dipoles [42, Figure 1]. The *surface* wave starts from the reflection point and propagates along the surface [13, Figure 8-11]. The receive antenna's height governs the intercept of the surface wave. Field effects caused by the continuous reflections along the surface are omitted. No HF skywaves refract from the ionosphere or scatter in the troposphere.

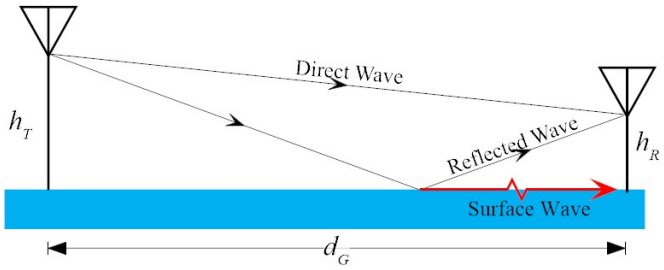


Figure 1: LOS Region at HF: Ray trace model; skywaves omitted.

The distance to the horizon is basic to surface-wave discussions. The transmitter's antenna height h_T and the receiver's antenna height h_R determine the distance d_H to the horizon. Specific for this report [34, page 114], [38, page 97]:

$$d_H = \sqrt{2h_T}\Big|_{411\text{feet}} + \sqrt{2h_R}\Big|_{21\text{feet}} \approx 57 \quad [\text{km}],$$

assuming a 4/3 earth. When the antenna heights are small, Norton points out that [42, Page 625]:

> "Consider the transmission from a transmitting antenna near the ground. When the receiving antenna is also near the ground, the received field is a surface wave only; ..."

Equivalently, the distance to the horizon is almost zero. Propagation beyond the horizon is described by Norton [42, Page 625]:

> The surface wave at large distances is a diffracted wave; i.e., the waves are prevented by the bulge of the earth from passing directly into this region and so must reach it by a process of bending around the curved surface of the earth; the portion of this bending which is not due to refraction is called diffraction.

BLOS Region: Figure 2 shows simplified propagation beyond the horizon, assuming the antennas are connected to the earth, the antenna heights relatively low, and [64, page 1593]:"non-flat longitudinal paths with obstacles not higher than a wavelength, and not closer than 8–10 km either to the transmitter or receiver." The figure shows the ground wave incident at the *point of attachment* Q_1 [35]:

> "One part of the ray continues straight on as predicted by geometrical optics, a second part follows the surface into the shadow region as a surface ray shedding diffracted rays tangentially as it propagates."

The surface wave travels from Q_1 along the surface shedding tangent rays. When the surface wave arrives at the *point of detachment* Q_2, the figure shows a tangent ray traveling to the receive antenna.

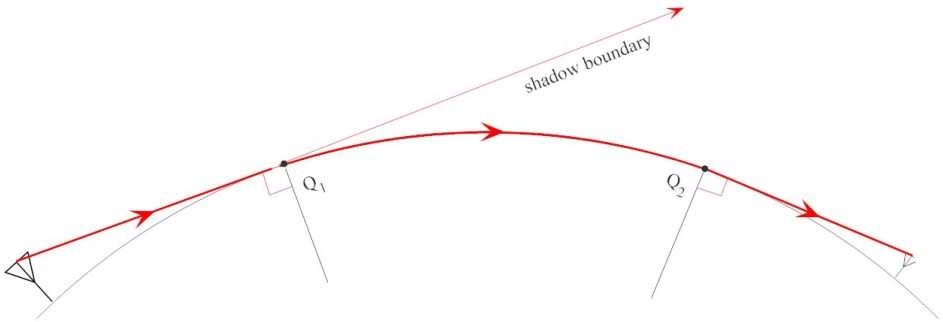


Figure 2: BLOS Region at HF: Surface wave propagation beyond the horizon; skywaves omitted. Adapted from [35].

Figure 2 shows the surface wave does not admit multiple paths. Surface-wave measurements verify fading is well-modeled as single-ray Rician fading. Therefore, the Rician model in Equations 1 and 2 makes physical sense. This report's main objective is identifying the fading in the surface-wave channel. This goal is delivered in Tables 2 to 16 where Rician fading parameters are tabulated for multiple frequencies and ranges.

This fading analysis does not model the surface-wave propagation to predict the received power. Although propagation modeling was not in the original experimental plans, Appendix C augments the original plans by comparing *measured* channel gain to *theoretical* surface-wave propagation codes. The comparison assumes the received power p_R is a scaled version of the transmitter's power p_T as

$$p_R = p_T \; g_T \; g_R \; |h|^2, \tag{3}$$

where g_T denotes the transmit antenna's gain, g_R denotes the receive antenna's gain, and $|h|^2$ denotes the channel gain. This equation assumes perfect matching circuits, vertical polarization, and no other circuits losses. Figure 3 presents a ground-wave model that best matches the measurements from this experiment. This model predicts *Basic Transmission Loss* as a function of range and frequency—assuming a smooth earth, low-salinity sea water, and vertical monopoles mounted on the ground with antenna heights limited to 50 meters. Basic transmission loss is defined in Figure 4.

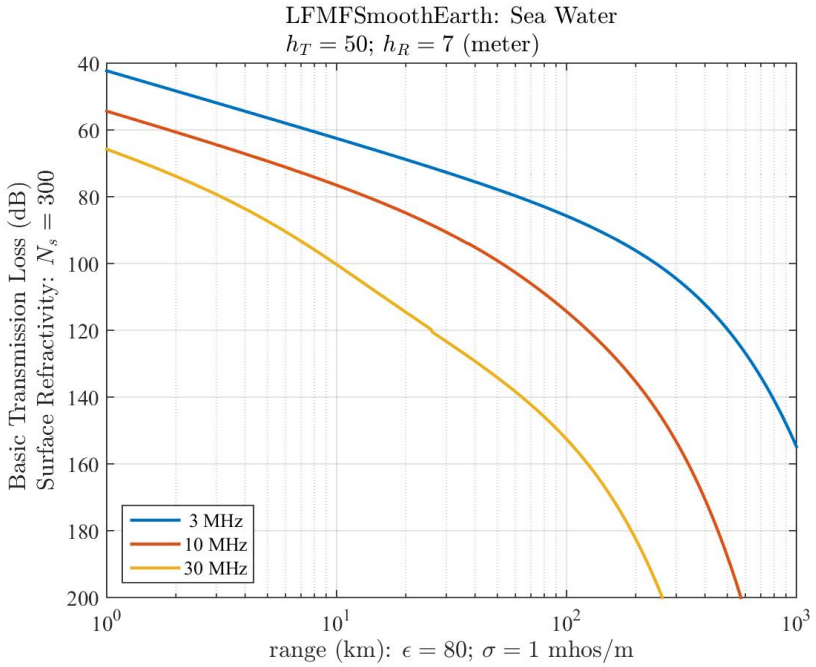


Figure 3: Surface-wave propagation at 3, 10, 30 MHz; Propagation from vertically polarized monopoles [33, Figure 1], [24], [74].

Figure 4 defines multiple losses between the transmitter and receiver [32]. The figure defines *Basic Transmission Loss* as the loss from transmitter's antenna surface to the receiver's antenna surface. The figure shows this loss is independent of the antennas and their associated circuits. In terms of Equation 3, the basic transmission loss is the reciprocal of the channel gain $|h|^2$. The free-space loss equation assumes *isotropic* antennas [32, Section 1.1]. Other antennas determine different free-space loss formulas [37].

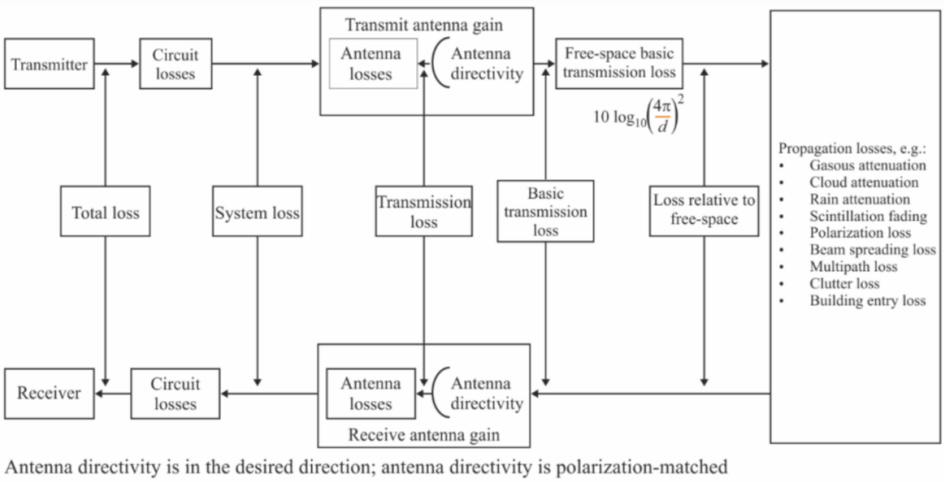


Figure 4: Losses along the radio circuit [32, Figure 1] (Reproduced with the ITU's permission).

Summary: Figure 2 shows the surface-wave model that approximates these HF channels sounded in these experiments. This surface-wave model makes credible the hypothesis that the fading in a surface-wave channel is Rician fading. The experiments show strong Rician fading (i.e., K factor exceeding 10 dB).

Reader's Guide: Section 2 reviews the channel sounding by correlation. The reader familiar with correlation sounding can skip this section. Section 3 reviews the Rician fading using a "template" specific to these channels. The reader familiar with Rician fading can skip this section and start the Rician fading analysis in Section 4. The reader programming an HF Emulator can skip the fading analysis and use the Rician fading tables in this section. The reader estimating a link budget for a surface-wave HF network can skip to Appendix C.

2 Transmitter, Receiver, Signal Processing

This section documents the hardware and signal processing used in these shore-to-ship experiments during {01–06}-June-2020. The transmitter was located in San Diego, CA. The receiver was carried on the Research Vessel (R/V) *Acoustic Explorer*. Figure 5 shows the ship's track on 03-June-2020 in the experiment's region southwest of the transmitter.



Figure 5: *Acoustic Explorer's* track on 03-June-2020.

As the ship traveled along its daily track, the ship's receiver recorded the channel soundings broadcast from the San Diego transmitter. The transmitter and receiver were GPS synchronized to record each channel sounding and its corresponding ship's location simultaneously. This GPS distance between the transmitter and ship's location determines the surface wave's time delay (See Equation 1). This simultaneous recording allows the surface-wave channel to be identified in channel sounding and not confused with HF skywaves that arrive later.

Sections 2.1 and 2.2 describe the transmitter and receiver, respectively. Both sections describe the GPS hardware to locate the ship's position and synchronize the channel sounding between the transmitter and receiver. Section 2.3 reviews the channel-sounding waveform and the signal processing to extract the HF channel.

2.1 Transmitter at NIWC

NIWC Pacific programmed custom waveforms into commercial off-the-shelf (COTS) software-defined radios (SDRs) for the purposes of measuring the HF channel and signal-to-noise ratio (SNR) in low SNR environments (down to roughly −30 dB SNR). Figure 6 is an exploded view of the custom transmitter kit. A laptop running a custom LabVIEW virtual instrument controls an Ettus SDR. The SDR connects to a Global Positioning System (GPS) antenna to synchronize frequency and timing with all receivers to measure both absolute delay and channel Doppler spread. A variable attenuator keeps the power amplifier in its linear region at 100 Watts. A power meter records power and voltage standing wave ratio (VSWR) to the transmitter's HF antenna.



Figure 6: Land-based transmitter schematic.

These experiments employed TCI's Dual Mode Compact HF Antenna (TCI Model 619) operating in low-angle mode (i.e., 40.5-foot vertical monopole). Figure 7 reports the elevation patterns for the low-angle mode [68]. The patterns show the maximum gain at the horizon starts to decrease at 10 MHz.

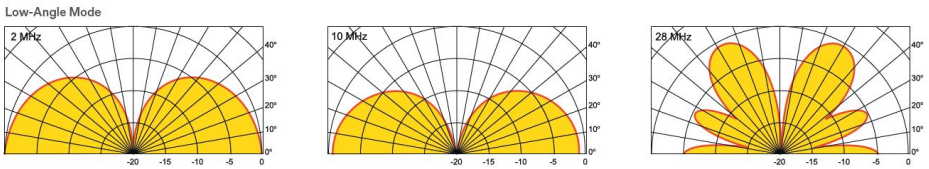


Figure 7: Elevation patterns (dBi) for the TCI-619 operating in low-angle mode over a perfect earth (Courtesy of TCI).

Figure 8 shows an open transmitter kit. Figure 9 shows the transmit antenna's location on Building 40 at NIWC Pacific. This antenna was located on the northwest corner approximately 411 feet above sea level.

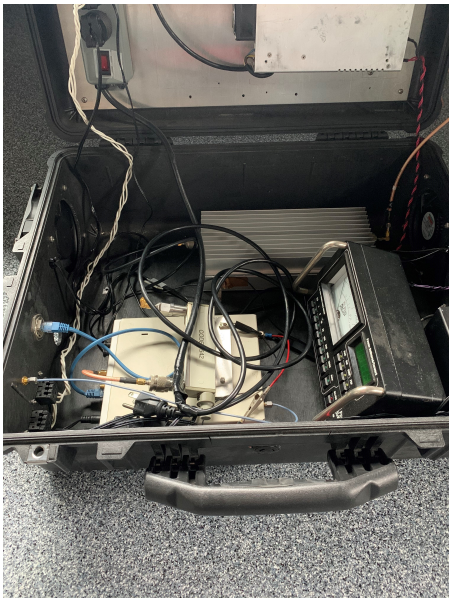


Figure 8: Transmitter kit.



Figure 9: Transmitter's antenna on Building 40, NIWC Pacific.

2.2 Shipboard Receiver

Figure 10 shows an exploded view of the SDR-based receiver kits. An RFSPACE SDR obtains a 1 pulse-per-second (PPS) reference from a Novus GPS-disciplined oscillator (GPSDO) from a GPS antenna operating at 10 MHz. The HF receive antenna is connected to RF analog conditioning hardware that feeds the RFSPACE SDR. The SDR streams complex I/Q packets to a laptop running the free Spectravue software that also controls the SDR. Each channel sounding has a duration of one minute. The laptop saves the I/Q of the channel sounding in .WAV files that are time stamped and frequency stamped for post-processing. The Windows clock was synchronized with the GPS so the time stamps are accurate to a second. This system guarantees the channel sounding signals are located at the ship's position with a time-stamp error of less than one second.

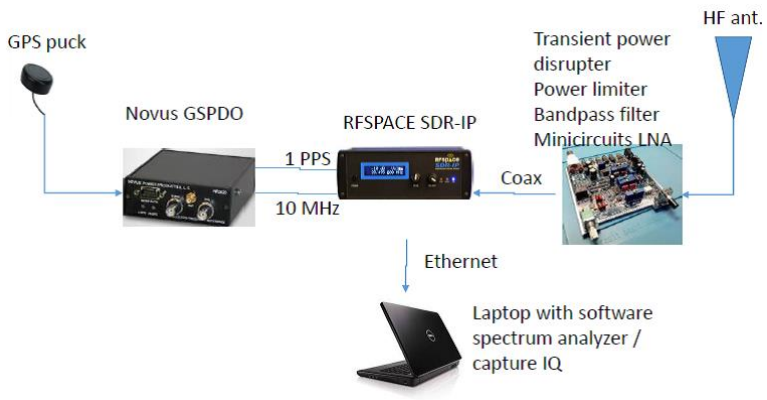


Figure 10: Shipboard receiver schematic.

Figure 11 shows this receiver aboard the Research Vessel (R/V) *Acoustic Explorer*. Figure 12 shows the *Acoustic Explorer*. This vessel is based at Pt. Loma, San Diego, CA and described as follows [50]:

> "The R/V Acoustic Explorer is a steel hull, twin screw, house forward, oceanographic research vessel built in 1981 and refitted by the Navy in 1988. The length overall is 130 feet, the beam is 30 feet, the main deck is 58 feet by 24 feet, the vessel tonnage is 197 tons and berthing is available for 16 persons including crew and scientists."

The HF antenna carried on the ship is a vertical whip approximately 10 feet in length. Figure 13 shows the whip mounted approximately 21 feet above the sea surface on the ship's port side.

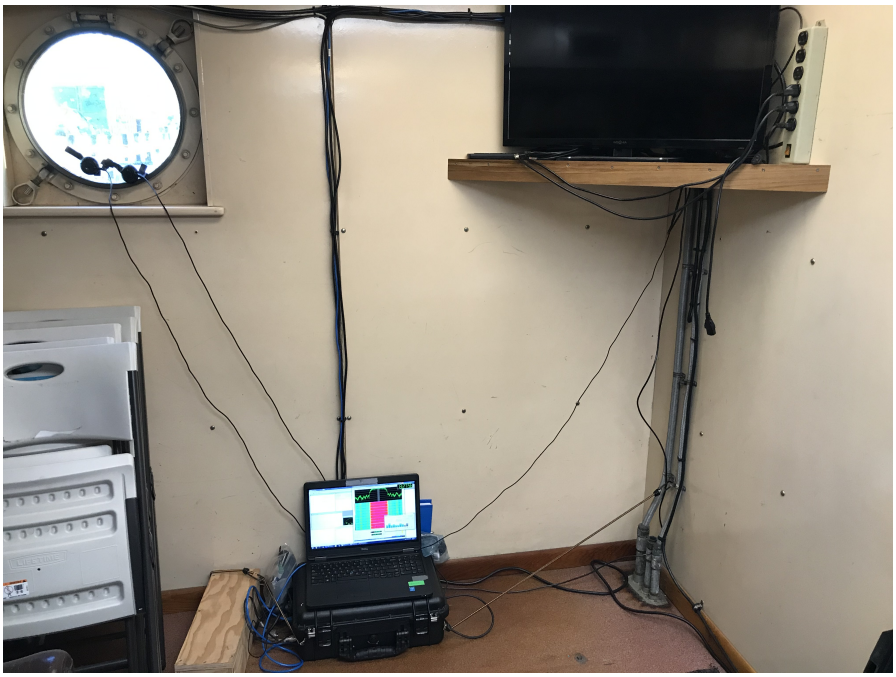


Figure 11: Receiver kit on the *Acoustic Explorer*.



Figure 12: The *Acoustic Explorer*.



Figure 13: The HF receive antenna mounted on *Acoustic Explorer*.

2.3 Channel Sounding

This section reviews the channel-sounding signal processing that extracts the surface-wave HF channel. Figure 14 is a system-level block diagram. The channel-sounding signal $s_{\mathsf{PN}}(t)$ is a Pseudo-Noise (PN) signal transmitted into the HF channel. The time-varying HF channel $h(t,\tau)$ filters this PN signal. The three-tap channel on top of the HF channel block represents an HF channel. This filtered signal is fed into the inverse filter to extract the HF channel. The three-tap channel at the inverse filter's output represents the extracted HF channel. The signal processing in each system-level block is described in the following paragraphs.

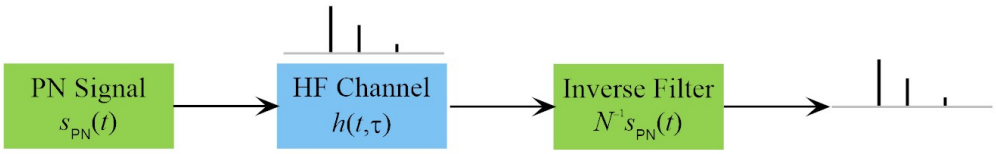


Figure 14: Block diagram showing the PN signal sounding the channel and the inverse filter extracting the channel.

2.3.1 PN Signal

The HF channel is sounded using a PN10 sequence modulated onto a root-raised cosine:

$$s_{\mathsf{PN}}(t) = \sum_{n=1}^{N} b_n s_{\sqrt{\mathsf{RC}}}(t - t_n); \quad t_n = nT_{\mathrm{SYM}},$$

where $T_{\mathrm{SYM}} = 40$ μs is the duration of the symbol corresponding to the symbol rate of 25 kHz, $b_n = \pm 1$ is a PN10 sequence of length $N = 1023$, and $s_{\sqrt{\mathsf{RC}}}(t)$ is the root-raised cosine using 0.35 roll-off factor.

2.3.2 HF Channel

The *delay spread function* $h(t,\tau)$ is one representation of time-varying channel that maps a transmitted signal $s_T(t)$ onto a received signal $s_R(t)$ as [8]:

$$s_R(t) = \int_{-\infty}^{\infty} h(t, t-\tau) s_T(\tau)\, d\tau.$$

A classic delay spread function has fading processes $\{h_\ell(t)\}$ at delays τ_ℓ [51, Eq. 14-5-6]:

$$h(t,\tau) = \sum_{\ell=1}^{L} h_\ell(t)\delta(\tau - \tau_\ell).$$

If the PN signal is pushed through this channel, the received signal is the sum of delayed and faded copies of the PN signal:

$$s_R(t) = \sum_{\ell=1}^{L} h_\ell(t) s_{\mathsf{PN}}(t - \tau_\ell).$$

2.3.3 Inverse Filter

The PN10 sequence $\{b_n\}$ itself is an approximate inverse filter under correlation:

$$\widetilde{\mathbf{b}} * \mathbf{b} \approx N \times \delta(t)$$

where "*" denotes linear convolution and the tilde denotes reversing the index so that the convolution becomes a correlation. The complex conjugate is omitted because the b_n's are real. The PN signal $s_{\mathsf{PN}}(t)$ inherits this approximate inverse filter under convolution:

$$\widetilde{s}_{\mathsf{PN}}(t) * s_{\mathsf{PN}}(t) \approx N \times \delta(t),$$

where $\widetilde{s}_{\mathsf{PN}}(t) = s_{\mathsf{PN}}(-t)$. If the channel is *stationary* so that each fading process is constant (i.e., $h_\ell(t) = \text{constant}$), the channel is extracted by correlating the PN signal with the received signal:

$$(N^{-1}\widetilde{s}_{\mathsf{PN}}) * s_R(t) \approx \sum_{\ell=1}^{L} h_\ell \delta(t - \tau_\ell). \tag{4}$$

Channel estimators assume a *slowly varying* channel so that a *stationary* channel is a good approximation during the PN signal's duration. If the transmitted signal consists of a *sequence* PN signals, the received signal is a *sequence* of filtered PN signals. Correlation with the PN signal extracts a *sequence* of *slowly varying* channels recording the fading $\{h_\ell(t)\}$ at each tap τ_ℓ. Details of this channel estimator are found in [16]. Quantification of "slowly varying" is found in [18]. For this report, knowing that correlation gain is approximately 30 dB is sufficient to explain that the surface-wave channel is extracted when buried in noise.

3 A Fading Analysis Template

The next section analyzes fading on multiple days and multiple frequencies. This section analyzes a representative experiment in detail. This fading analysis "template" avoids repeating the same text for each day and each frequency.

Section 3.1 uses the power-delay profile to verify the surface-wave's delay. Section 3.2 observes Rician characteristics in the surface-wave's complex phase. These characteristics are modeled by the Rician parameters: the Doppler shift f_D, the K factor, and the RMS bandwidth f_{RMS}. Section 3.3 reviews the moment-based estimators that extract these Rician parameters from the measurements. Estimating these Rician parameters raises the fundamental question of stochastic modeling:

> *How can a stochastic model—such as Rician fading—be verified from measurements?*

The moment-based estimators assume a Rician model. Assuming a Rician model to extract Rician parameters is a splendid example of circular reasoning. Absent a physics-based model of Rician fading, Section 3.4 mitigates this *circular reasoning* by the direct observations:

- The phase is almost linear so that a Doppler shift makes sense,
- The complex phase exhibits a rotating specular component perturbed by a small diffuse component so the large K factor makes sense,
- The diffuse component exhibits a Rician distribution so claiming the diffuse component is a Gaussian random process makes sense,
- The diffuse component exhibits a Gaussian power spectrum in the low-noise measurements.

Section 3.4 discusses each Rician feature in detail. This detailed discussion avoids repetitive text in Section 4. Section 3.5 reports the Gaussian power spectrum is still visible in high-noise measurements but corrupted by a nearly flat noise floor. This observation implies either the noise is an experimental artifact or the Gaussian power spectrum must be generalized. Section 3.6 uses *synthetic* Rician simulations to argue noise arises from the experiment and is not a surface-wave characteristic. This argument concludes by showing a low-noise measurement exhibiting a textbook Gaussian power spectrum. Nevertheless, without a physics-based model Rician fading, Section 4 reports the RMS bandwidth estimates and observes when the estimate is biased high.

3.1 Power-Delay Profile

Even when the spectrograms do not show the channel sounding signal, the PN sequence's *correlation gain* pulls the channel out of the noise (See Section 2.3.3). The resulting surface-wave channels $\{h_{\mathsf{SW}}(t,\tau)\}$ have the delay spread function [8]:

$$h_{\mathsf{SW}}(t,\tau) = h(t)\delta(\tau - \tau_G); \quad \tau_G = d_G c_0^{-1},$$

where $\{h(t)\}$ is the fading of the surface wave, d_G is the ground range between the transmitter and receiver, and c_0 is the speed of light. All measurements show excellent agreement between the delay τ_G and the ground range d_G. Averaging over time produces the power-delay profile:

$$E_t\left[|h_{\mathsf{SW}}(t,\tau)|^2\right] = E\left[|h(t)|^2\right]\ \delta(\tau - \tau_G).$$

All measured power-delay profiles show a single spike at delay τ_G corresponding to the ground range between the ship and the transmitter. Figure 15 shows a typical power-delay profile. The "0.23 ms" printed next to the spike matches the ground range delay τ_G determined from the ship's location (Figure 61) by the GPS files. The close agreement between the measured delay and the theoretical delay argues that this spike is the surface wave.

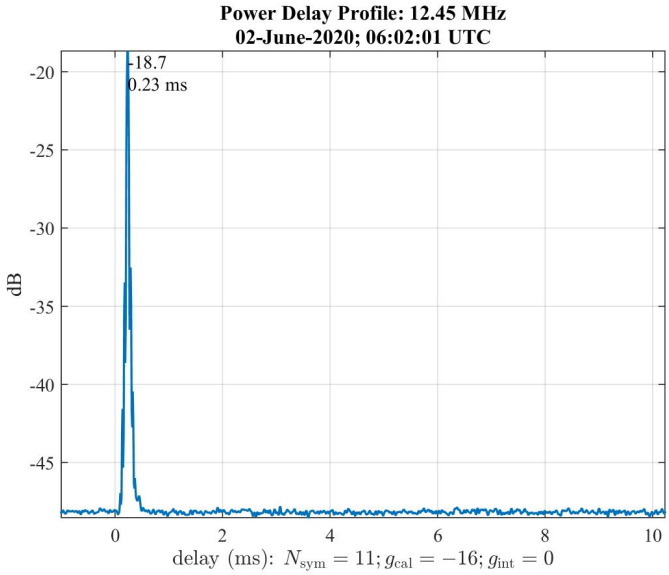


Figure 15: Power-delay profile on 02-June-2020 06:02:01 UTC at 12.45 MHz.

3.2 Rician Fading

Once the surface-wave delay is known, the surface-wave fading $\{h(t)\}$ is extracted from the delay spread function. Figure 16 is a phase plot typical of surface-wave fading. The plot shows the fading slowly rotating around the origin subject to small perturbations. That is, the surface-wave fading $\{h(t)\}$ is *Rician*

$$h(t) = e^{j\phi(t)}\{s_{\mathsf{LOS}} + g(t)\}; \quad |s_{\mathsf{LOS}}|^2 \gg \sigma_g^2 = E\left[|g(t)|^2\right], \tag{5}$$

where the phase $\{\phi(t)\}$ performs the rotation, the *specular component* s_{LOS} models the average radius, and the *diffuse component* $\{g(t)\}$ models the small perturbations as a zero-mean, wide-sense stationary random process with variance σ_g^2.

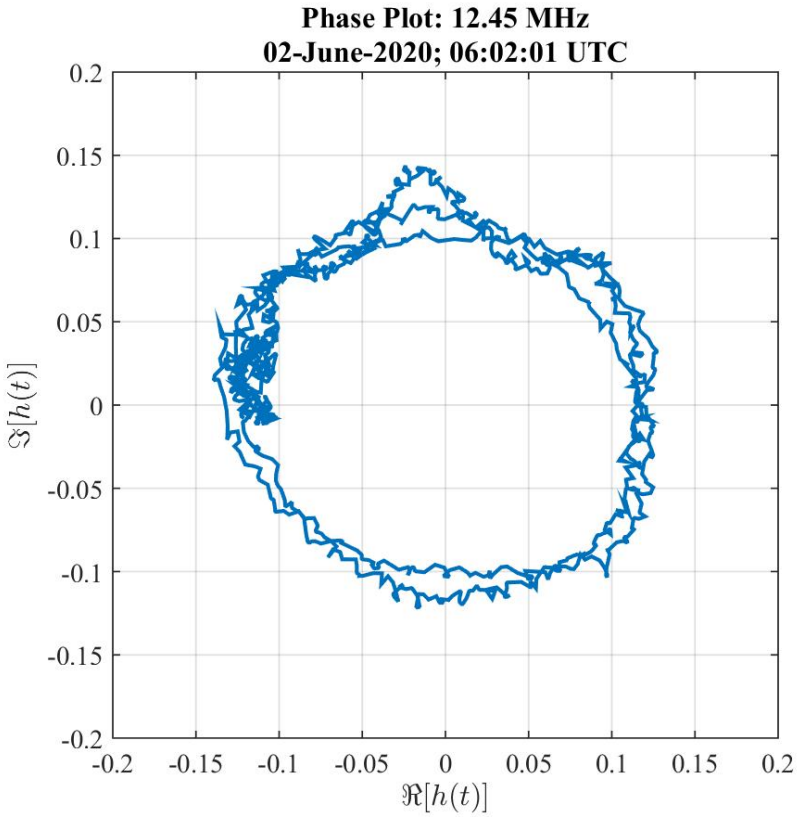


Figure 16: Fading phase on 02-June-2020 06:02:01 UTC at 12.45 MHz.

All experiments report that the ratio K of the specular power to the diffuse power is large:

$$K = 10\ \log_{10}\left(\frac{|s_{\mathsf{LOS}}|^2}{\sigma_g^2}\right) > 10 \quad [\text{dB}]. \tag{6}$$

The power p_E in the fading envelope is

$$p_E = E[|h(t)|^2] = |s_{\mathsf{LOS}}|^2 + \sigma_g^2. \tag{7}$$

The Rician fading is parameterized using p_E and K rather than s_{LOS} and σ_g^2 because the fading envelope admits the immediate estimate:

$$p_E \approx \widehat{p}_E = \frac{1}{N}\sum_{n=1}^{N} |h(t_n)|^2.$$

The "hat" is standard notation marking the parameter is an estimate from the measurements. In almost all the experiments, the phase is nearly linear

$$\phi(t) = \phi(0) + 2\pi f_D t \quad + \quad \text{small higher-order terms}$$

so modeling the surface-wave fading with the Doppler shift f_D makes sense:

$$h(t) = e^{j2\pi f_D t}\{s_{\mathsf{LOS}} + g(t)\}; \quad |s_{\mathsf{LOS}}|^2 \gg \sigma_g^2. \tag{8}$$

The fading is called *Rician* provided the diffuse component $\{g(t)\}$ is a wide-sense stationary, zero-mean random process that is *circular Gaussian* [66]. The final parameter is the diffuse component's power spectrum. Standard Rician fading models the power spectrum as

$$P_{gg}(f) = \frac{\sigma_g^2}{\sqrt{2\pi} f_{\mathsf{RMS}}} \exp\left(-\frac{f^2}{2f_{\mathsf{RMS}}^2}\right), \tag{9}$$

using *RMS bandwidth* f_{RMS}. This report models the surface-wave fading using the Rician parameters $\{f_D, K, f_{\mathsf{RMS}}\}$ leaving the envelope power p_E and delay τ_G to be specified by location. Section A reviews the Rician parameters in detail and derives three classes of Rician estimators. The next section summarizes the moment estimation of $\{f_D, K, f_{\mathsf{RMS}}\}$.

3.3 Rician Estimators

The Rician parameters $\{f_D, K, f_{\mathsf{RMS}}\}$ are amenable to moment-based estimates:

$$E[\dot{h}(t)\overline{h(t)}]/p_E = -j2\pi f_D, \tag{10}$$

$$\mathsf{Var}[|h(t)|^2]/p_E^2 = \frac{2K+1}{(K+1)^2}, \tag{11}$$

$$E[|\dot{h}(t)|^2]/p_E = 4\pi^2 f_D^2 + \frac{4\pi^2}{K+1} f_{\mathsf{RMS}}^2, \tag{12}$$

where the "dot" denotes the derivative $\dot{h}(t)$ and the "overline" $\overline{h(t)}$ denotes the complex conjugate. Section A illustrates the performance of these estimators in Rician simulations. The simulations show these moment-based estimators recover the Rician parameters $\{f_D, K, f_{\mathsf{RMS}}\}$ using values encountered in the experiments. Section 4 applies these moment-based estimators to extract the Rician parameters.

3.4 Rician Parameters

Figure 17 shows the surface-wave's fading $\{h(t)\}$ in amplitude and phase. The upper panel lists the date, time, and frequency of the sounding. The lower panel lists the moment-based estimates $\{\widehat{f}_D, \widehat{K}, \widehat{f}_{\mathsf{RMS}}\}$. The transient at the beginning of the sounding is removed from the estimates. These estimates are tabulated and compared to other Rician estimators that summarize each day's experiment. Section A discusses the technical details of the Rician estimators.

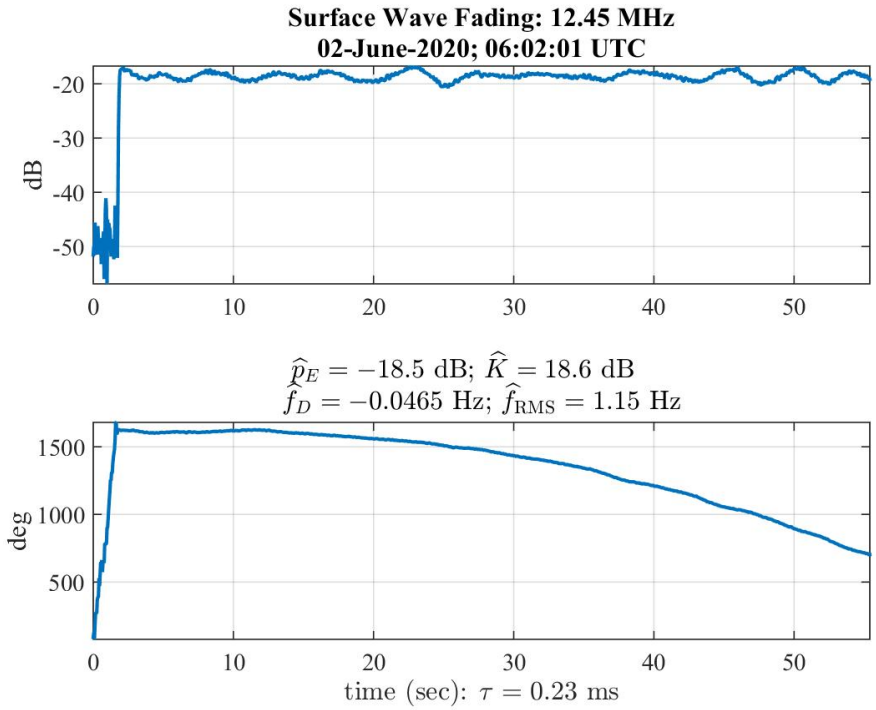


Figure 17: Fading on 02-June-2020 06:02:01 UTC at 12.45 MHz.

Because the diffuse component $\{g(t)\}$ is complex-valued, circular, zero-mean Gaussian, the fading amplitude $\{|h(t)|\}$ has a Rician probability density [66, Eq. 2.45]:

$$p_{\mathsf{RICE}}(r) = \frac{2r}{\sigma_g^2} \exp\left(-\frac{r^2 + |s_{\mathsf{LOS}}|^2}{\sigma_g^2}\right) I_0\left(\frac{2r|s_{\mathsf{LOS}}|}{\sigma_g^2}\right); \quad r = |h(t)| \geq 0,$$

where σ_g^2 replaces the standard "$2\sigma^2$". Proving $\{g(t)\}$ has a Gaussian distribution from measurements alone is impossible. Instead, arguments must be based on physical models and comparisons with the measured fading.

Figure 18 illustrates such a comparison. The figure shows the distribution of $\{|h(t)|\}$ estimated by the Average-Shifted Histogram (ASH) developed by Scott [57].

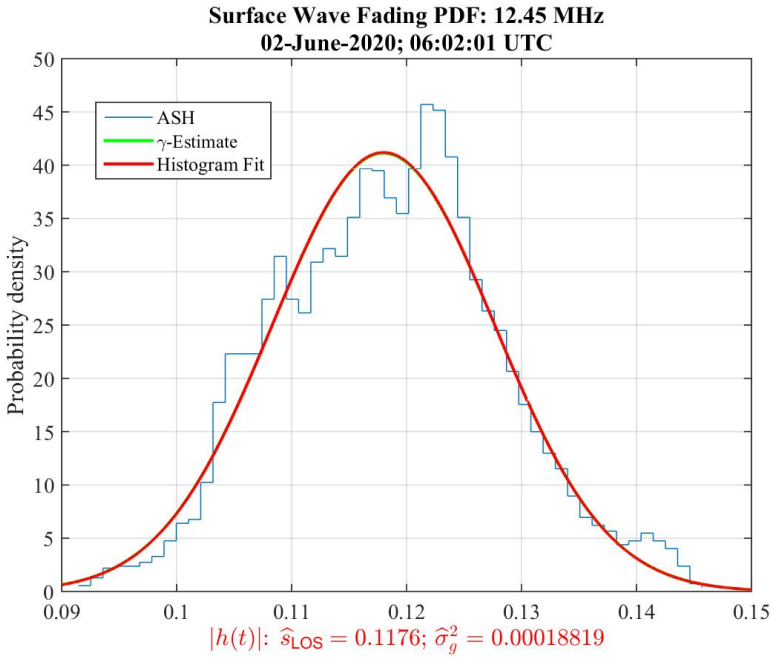


Figure 18: Histogram and Rician estimates; 02-June-2020 06:02:01 UTC at 12.45 MHz; Rician estimates overlay.

The figure also includes two Rician densities. The first density is obtained from the moment-based estimates of $\widehat{p}_E$ and $\widehat{K}$ that parameterize the Rician distribution (γ-Estimate). The second density is obtained by minimizing the *Kullback-Liebler divergence* between the ASH and the Rician densities (Histogram Fit) [53, Eq. 1.17]

$$d(p_{\mathsf{ASH}}||p_{\mathsf{RICE}}) = \sum_{n=1}^{N} p_{\mathsf{ASH}}(r_n) \log\left(\frac{p_{\mathsf{ASH}}(r_n)}{p_{\mathsf{RICE}}(r_n)}\right); \quad r_n = |h(t_n)|, \tag{13}$$

subject to the constraint that the Rician parameters satisfy the measured power:

$$E[|h(t)|^2] \approx \frac{1}{N}\sum_{n=1}^{N} r_n = |s_{\mathsf{LOS}}|^2 + \sigma_g^2. \tag{14}$$

The resulting Rician parameters $\widehat{s}_{\mathsf{LOS}}$ and $\widehat{\sigma}_g^2$ are reported on the figure's x-label. Both Rician estimators are nearly identical so their distributions overlay on the

plot. The following equation compares both estimators using the K-factor:

$$18.6 = \widehat{K} \approx 10 \log_{10} \left(\frac{|\widehat{s}_{\mathsf{LOS}}|^2}{\widehat{\sigma}_g^2} \right) = 18.7 \quad [\text{dB}].$$

The leftmost term is the moment-based estimate reported on Figure 17. The rightmost term is the K-factor estimated using the Histogram Fit. An error not exceeding 0.1 dB is obtained by these two completely different K-factor estimators. All the experiments report excellent agreement between these two estimators with one exception (See Figure 35).

The histogram's deviations from the ideal Rician distributions are explained by the phase plot in Figure 16. This phase plot shows the measured fading makes less than three rotations: the Doppler shift $\widehat{f}_D = -0.0456$ Hz implies -2.6 rotations in 56 seconds. A closer examination of the phase plot shows the diffuse component exhibits both a slowly varying component and a fast-fading component generating the many little "loops". With only 2.6 rotations of the phase, the slowly varying component produces local "lumps" that do not average out with only a few rotations. The sampling issues of the ASH and other non-parametric density estimators are eliminated if there existed a physics-based argument identifying the fading distribution. Section 5 reiterates this observation in the concluding observations of this report.

3.5 Rician Spectrum

Figure 19 shows the surface-wave fading spectrum. The spectrum shows a "spike" characteristic of Rician fading that is offset by the negative Doppler shift. The narrow part of the spike is generated by the specular component because $\widehat{K} > 18$ dB. The spike widens at 20 dB down and the spectral width is visible down to 50 dB. The spike's low-frequency energy generates the *slowly varying* component observed in the phase plot (See Figure 16). The fading spectrum shows relatively flat wideband noise. This high-frequency energy generates the *rapidly varying* tiny loops in the phase plot. This wideband noise produces RMS bandwidth estimates that are biased high.

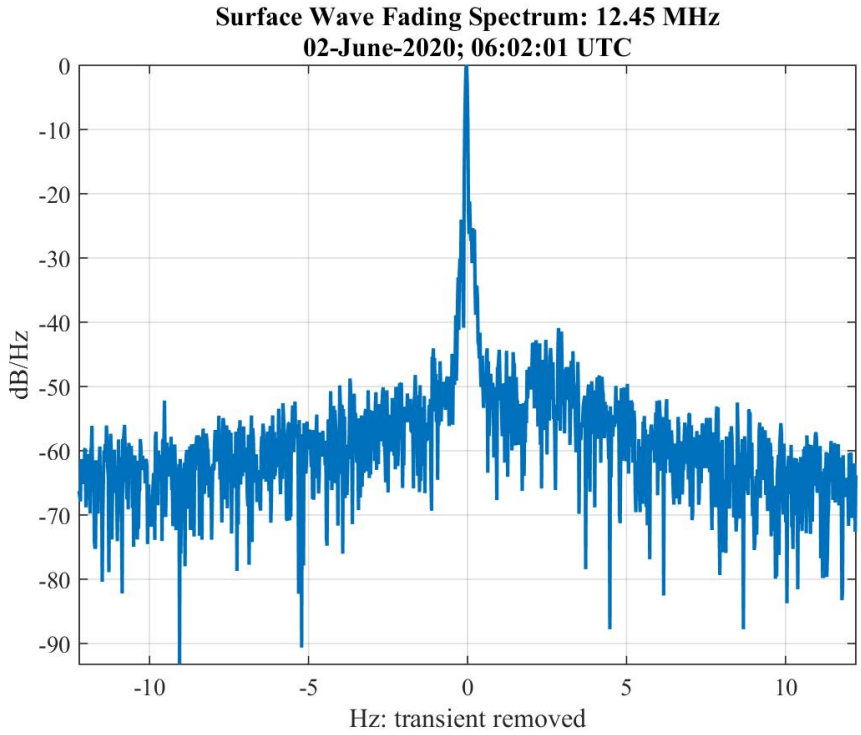


Figure 19: Fading spectrum on 02-June-2020 06:02:01 UTC at 12.45 MHz; $\widehat{K} = 18.6$ dB; $\widehat{f}_{\mathsf{RMS}} = 1.15$ Hz.

For concreteness, suppose the diffuse component $\{g(t)\}$ of a surface wave has the Gaussian power spectrum $P_{gg}(f)$ of Equation 9. If the measured diffuse component is contaminated with uncorrelated noise $\{w(t)\}$

$$\widetilde{g}(t) = g(t) + w(t),$$

the measured spectrum is a perturbation of the Gaussian spectrum:

$$P_{\widetilde{g}\widetilde{g}}(f) = P_{ww}(f) + P_{gg}(f).$$

Fitting this noisy spectrum with a Gaussian spectrum produces f_{RMS} estimates that are biased high. However, if the diffuse component is actually the sum of a low-frequency process $\{g(t)\}$ with a Gaussian spectrum and a wideband process $\{w(t)\}$ that really belongs to the diffuse component (i.e., $\{\widetilde{g}(t)\}$ is the true model), then fitting to the Gaussian spectrum is wrong.

The HF skywave literature handles this spectral modeling problem by introducing other spectral models. Figure 20 compares the Gaussian spectrum to the f^{-4} and f^{-6} spectrum developed by Dana [21]. These spectrums provide better fits to the measured spectrum observed in Sections 4.1.2 and 4.1.3.

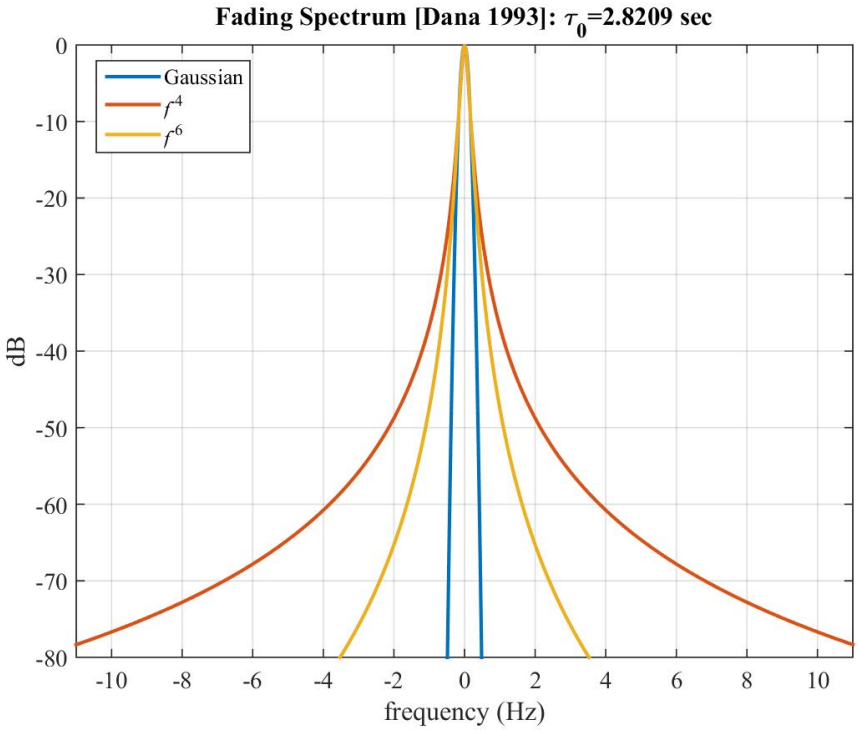


Figure 20: HF skywave's power spectrum models.

Although the Gaussian spectrum is a likely candidate for the low-frequency energy in the diffuse component, chasing measurements with a suite of spectrum-fitting tools does not advance engineering insight. Only a physics-based argument that derives the diffuse spectrum from the propagation over the sea surface—a model linking the spectrum to the parameters of the sea surface—reconciles the observed Gaussian spectrum in the low frequencies and the unknown shape of the high-frequency part of the spectrum. Therefore, Section 4 only reports the RMS bandwidth and remarks on the bias.

3.6 Rician Simulations

The preceding sections extracted individual Rician parameters from the measured fading. This section assesses the resulting Rician fading for use in NIWC's HF Channel Emulator. The assessment compares measurements to synthetic Rician fading generated as follows:

f_D Hz	K dB	f_{RMS} Hz
−0.0465	18.6	1.15
−0.0465	18.6	0.1

The simulations show the large K factor and the Doppler shift accurately model the measured specular component. The simulated diffuse component is less accurate because $\widehat{f}_{\mathsf{RMS}}$ is biased high. The bias is caused by the high noise floor.

Figure 21 plots the synthetic fading's amplitude and phase using the large RMS bandwidth. The upper panel reports the Rician parameters generating this synthetic fading. The lower panel reports near perfect estimates are extracted from this synthetic fading. Comparison to Figure 17 shows the synthetic phase is "too" linear and the synthetic amplitude lacks the measurement's slow modulations. The next plot shows this synthetic fading is too homogeneous in comparison to the measurements.

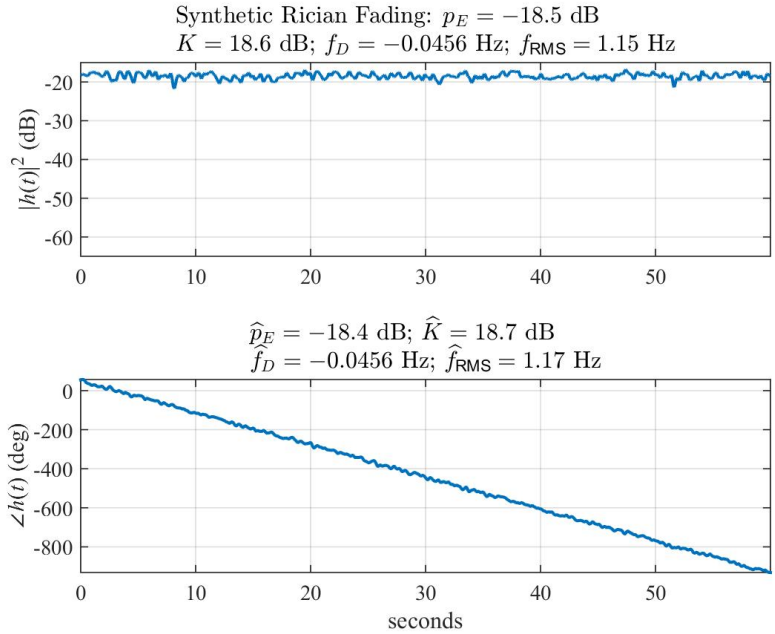


Figure 21: Synthetic Rician Fading; amplitude and phase; $f_{\mathsf{RMS}} = 1.15$ Hz.

Figure 22 plots the synthetic fading in the complex plane. The complex phase shows the large specular component rotating in perfect circles at the Doppler frequency. The diffuse component generates smaller loops at the end of the rotating specular component. Comparison with Figure 16 shows the measured diffuse component consists of a slowly varying component and a smaller high-frequency component generating tiny loops. The next plot shows the specular and diffuse components in different frequency bands to explain this synthetic fading.

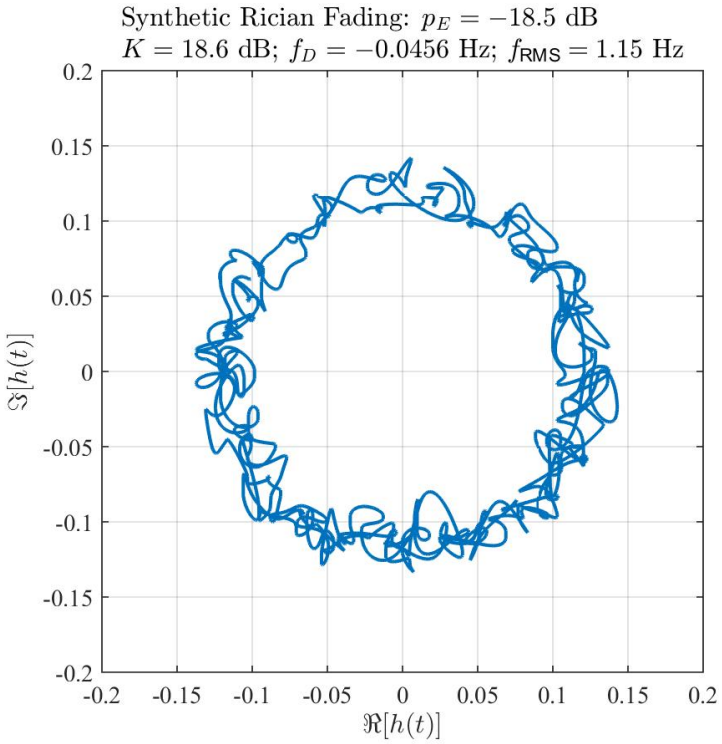


Figure 22: Synthetic Rician Fading; complex phase; $f_{\mathsf{RMS}} = 1.15$ Hz.

Figure 23 shows the synthetic fading's power spectrum separating the specular and diffuse components. The "spike" is generated by the specular component and shows the slight negative offset caused by the negative Doppler shift. The Gaussian power spectrum is generated by the diffuse component. The 3-dB level points to an RMS bandwidth of near 1 Hertz. Comparison with the measured spectrum in Figure 19 shows a "fatter" spike and a flat noise floor in the measured spectrum. The next plot shows the fat spike or, equivalently, the slow modulations are caused by the smaller RMS bandwidth.

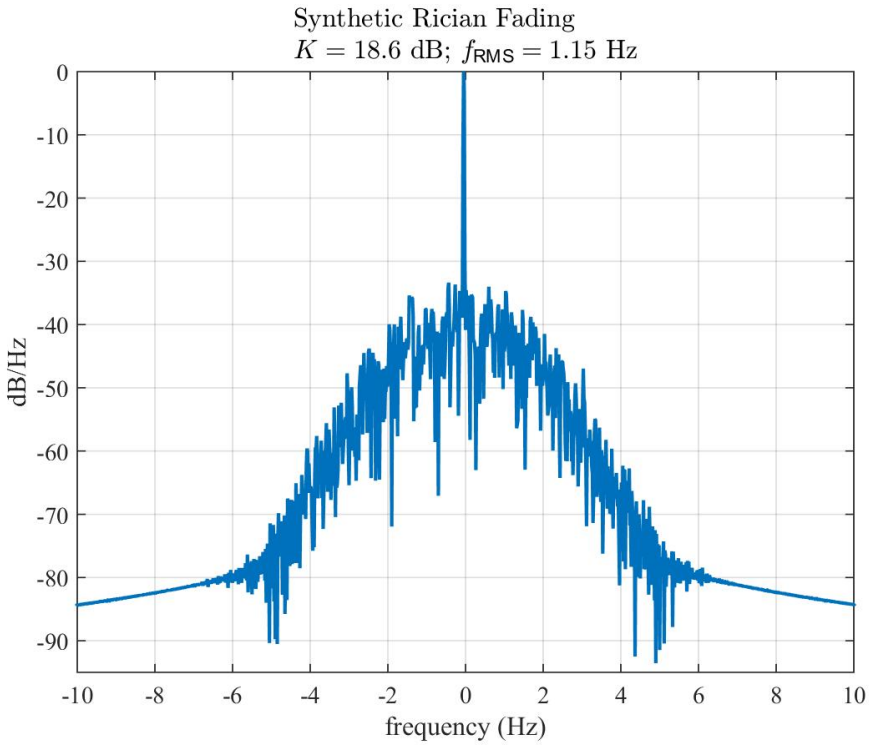


Figure 23: Synthetic Rician Fading; power spectrum; $f_{\mathsf{RMS}} = 1.15$ Hz.

Figure 24 shows the synthetic fading's amplitude and phase generated by the smaller RMS bandwidth. The Rician parameters and estimates are reported in the upper and lower panels, respectively. Although the synthetic fading's phase is too linear in comparison to the measurements, this amplitude exhibits slow modulations similar to measurements in Figure 17. These modulations are caused only by the smaller RMS bandwidth $f_{\mathsf{RMS}} = 0.1$ Hz. This observation is a warning to analysts attributing these modulations to the ship's motion. The next plot shows these slow modulations in the complex plane.

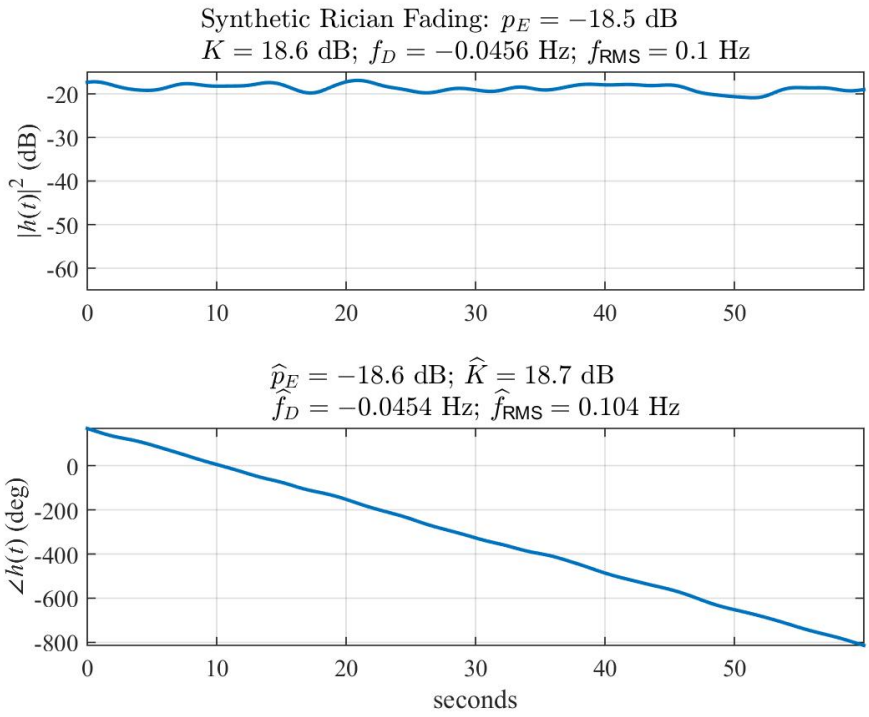


Figure 24: Synthetic Rician Fading; amplitude and phase; $f_{\mathsf{RMS}} = 0.1$ Hz.

Figure 25 plots the synthetic fading in the complex plane generated with $f_{\mathsf{RMS}} = 0.1$ Hz. The slow modulations appear to vary the specular component similar to the measurements in Figure 16. However, the measurements show tiny loops "riding" on these slow modualtions. The next plot shows the source of these tiny loops.

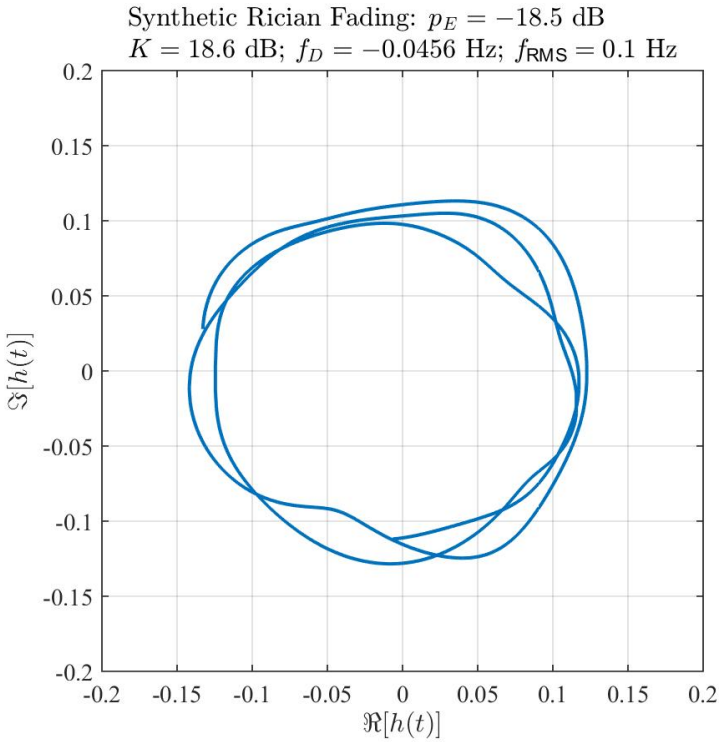


Figure 25: Synthetic Rician Fading; complex phase; $f_{\mathsf{RMS}} = 0.1$ Hz.

Figure 23 shows the synthetic fading's power spectrum using the smaller RMS bandwidth. This synthetic power spectrum shows the specular component slightly offset by the Doppler shift. The Gaussian spectrum is visible 25 dB down and spreading out 60 dB down into the Gaussian "tails". Consequently, the diffuse component will only show slow modulations. In contrast, the measured power spectrum shows a Gaussian spectrum immersed in flat noise (See Figure 19). This measured high-frequency noise causes the tiny loops observed "riding" on the slowly varying complex phase (See Figure 16). The next plot shows a power spectrum measured in low noise to reveal the Gaussian shape power spectrum.

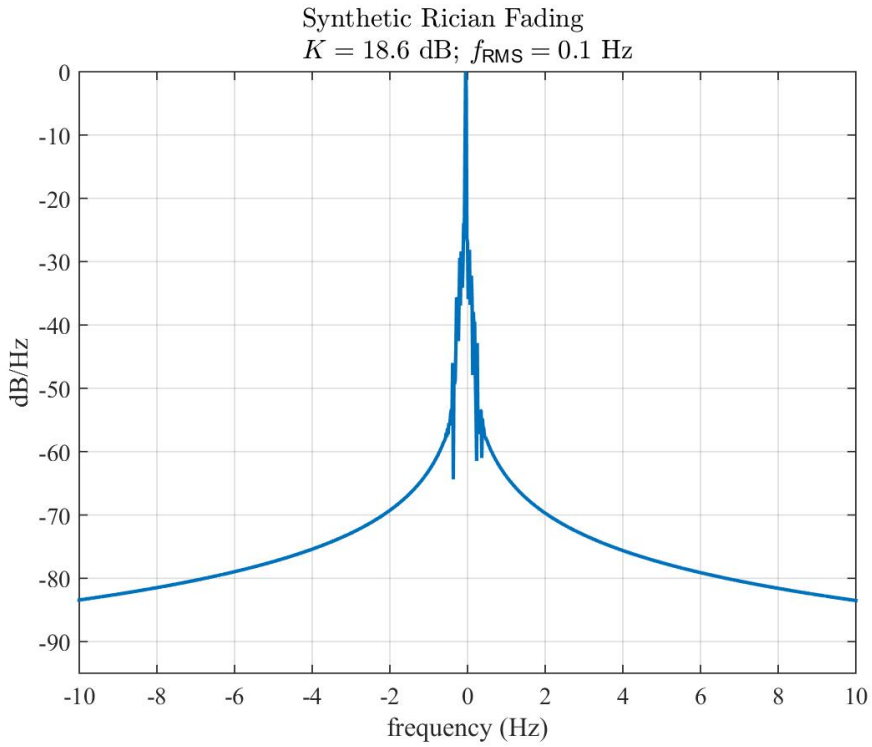


Figure 26: Synthetic Rician Fading; power spectrum; $f_{\mathsf{RMS}} = 0.1$ Hz.

Figure 27 shows a low-noise fading power spectrum. The Gaussian spectrum is visible down to 60 dB down where it spreads into the Gaussian "tails" and not the f^{-k} spectrum in Figure 20. The estimated RMS bandwidth is 0.355 Hz although the harmonics bias this estimate also. The excellent match between this measured power spectrum and the synthetic power spectrum (Figure 26) argue that surface-wave fading is Rician with Gaussian power spectrum, at least in the low-noise measurements.

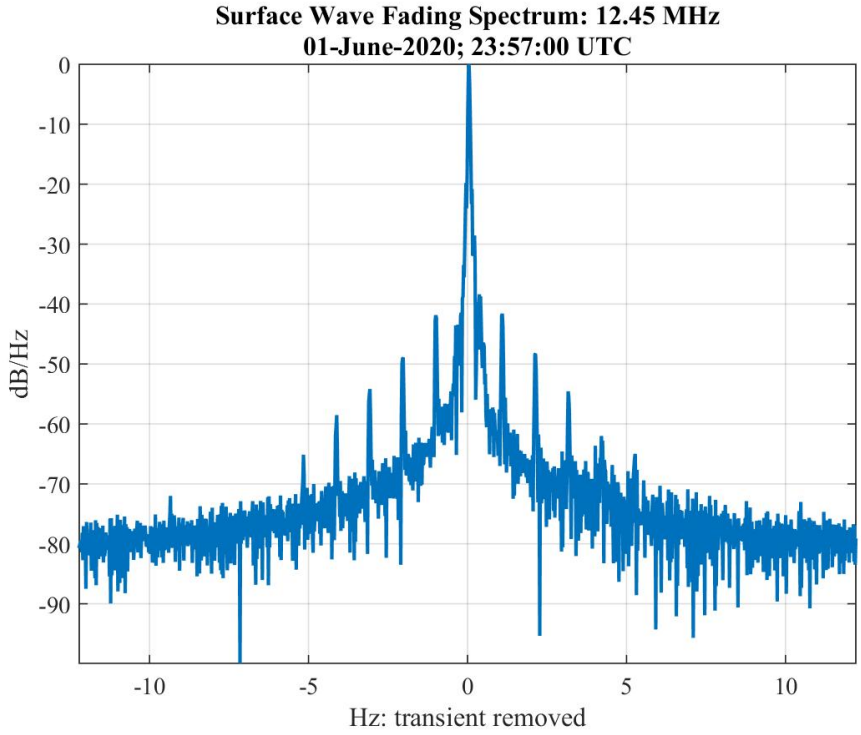


Figure 27: Fading spectrum on 01-June-2020 23:57 UTC at 12.45 MHz; $\widehat{K} = 26.1$ dB; $\widehat{f}_{\mathsf{RMS}} = 0.355$ Hz.

Summary: This fading template argues that the surface-wave fading—for these measurements—is well-modeled as Rician:

- The specular component is well-modeled by the K factor and Doppler shift estimates.
- The diffuse component is a Gaussian random process with Gaussian power spectrum—in the low-noise measurements.

High-noise measurements bias the RMS bandwidth estimate to the higher frequencies. This bias is called out in the experimental analysis of Section 4.

4 Soundings

The channel sounding signals were broadcast from the shore-base transmitter on Point Loma to the *Acoustic Explorer* on the following days:

$$\{1, 2, 3, 4, 5, 6\}\text{-June-2020}$$

This section organizes the fading analysis by day. Surface-wave channels are extracted from each day's experiments at the HF frequencies

$$4.23, 8.456, 12.45, 18.474, 23.1 \text{ MHz}$$

The fading at each frequency is analyzed using the fading "template" of Section 3. Each day concludes by tabulating the fading parameters to use in NIWC's HF channel emulator [18]. Table 1 is an example listing the fading parameters extracted from the surface-wave measurements on 05-June-2020 when the ship was almost 170 km from the transmitter. The HF channel emulator presented in the Executive Summary uses the parameters set out in 4.23-MHz column. The reader needing only surface-wave parameters can skip the analysis turn the tables.

Table 1: Surface-wave fading; 05-June-2020 at 21:35:00 UTC.

05-June-2020 21:35 UTC: Range 169.7 km; Delay 0.56 ms			
Frequency (MHz)	**4.23**	**8.456**	**12.1**
RMS Bandwidth (Hz)	3.8	1.58	4.23
Rician K Factor (dB)	21	18.8	16.5
Doppler Shift (Hz)	0.0635	0.102	0.135

4.1 01-June-2020

Figure 28 shows the ship starting in San Diego Bay, steaming west, and doubling back:

Start	13:20 UTC	1.5 km
End	23:59 UTC	40 km

These close distances allow the channel sounding signal to be received along the route as verified by the spectrograms and the delay spread functions. The gaps in the plots are caused ship operations necessitating shutting down the channel soundings across all frequencies.



Figure 28: *Acoustic Explorer's* track on 01-June-2020.

Figure 29 compares all spectrograms on 01-June-2020. The spectrograms show the channel-sounding signal decreasing as the ship steams away from the transmitter. The decrease of power as a function of distance is also present in the delay spread functions in Figure 30. Despite interference observed in all the spectrograms, the channel-sounding signal persists during the entire experiment out to the 40-km ranges from the transmitter.

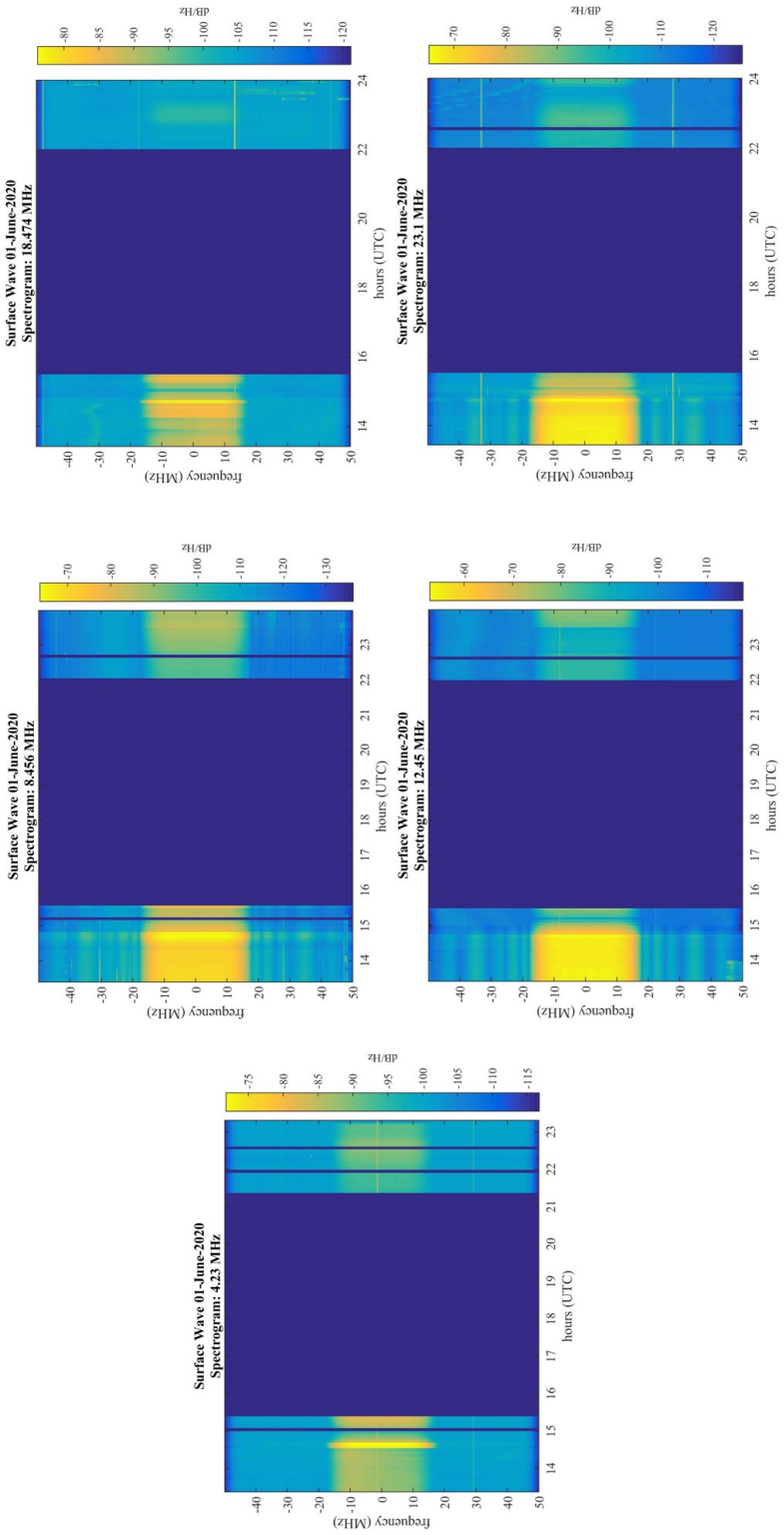


Figure 29: Spectrograms on 01-June-2020.

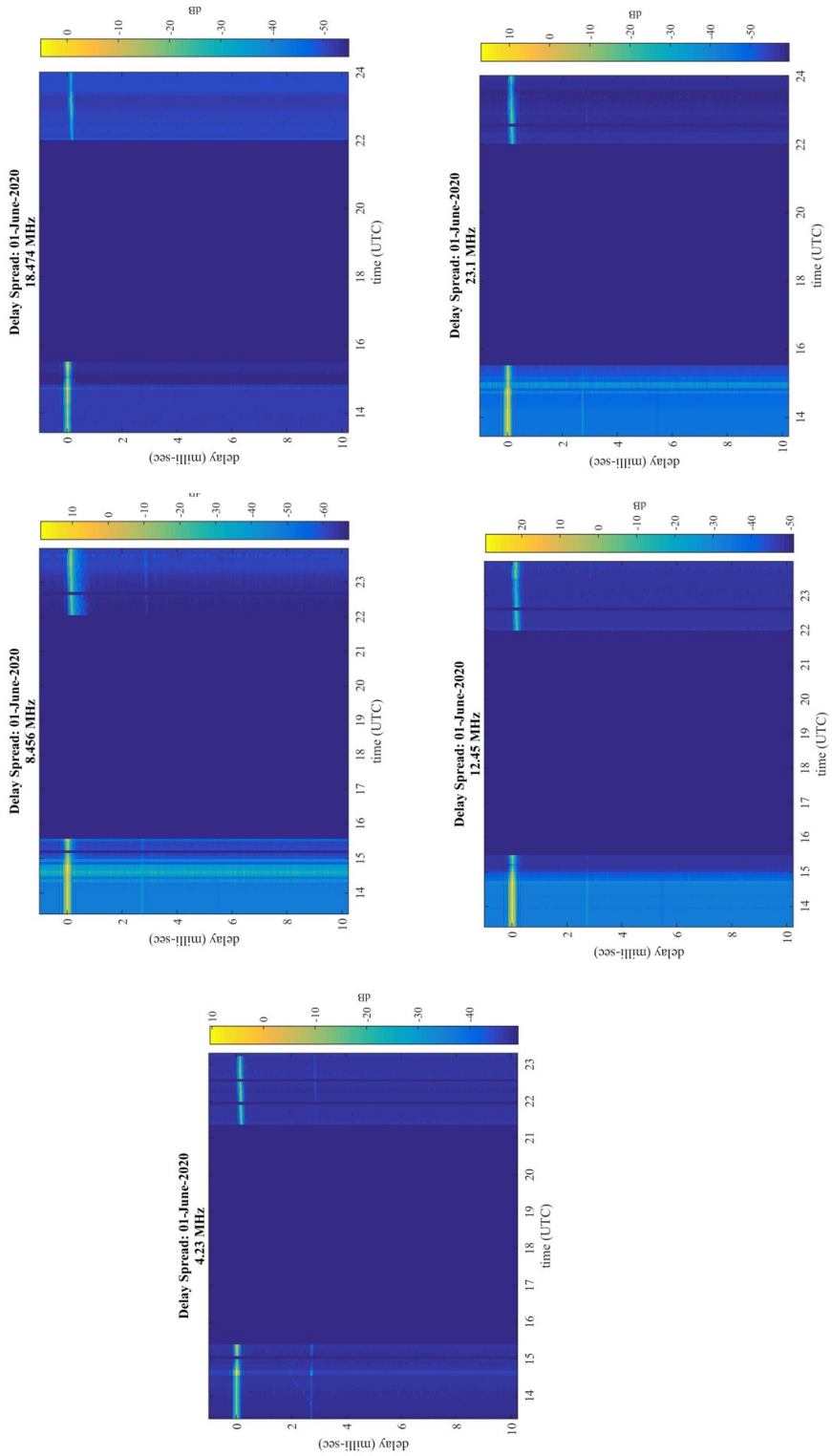


Figure 30: Delay spread functions on 01-June-2020.

Figure 31 locates the ship near the end of the track for the fading analysis. At this location, the GPS time is 23:56:17 UTC and the ship is approximately 40 km from the transmitter heading to the southeast. At this range, the theoretical delay computed from the ground range is

$$\tau_G = \left.\frac{d_G}{c_0}\right|_{d_G=40.1373} = 0.1338 \quad [\text{ms}].$$

The following sections report this theoretical delay agrees with the 0.14 ms delay measured at 4.23, 8.456, 12.45, 18.474, and 23.1 MHz.

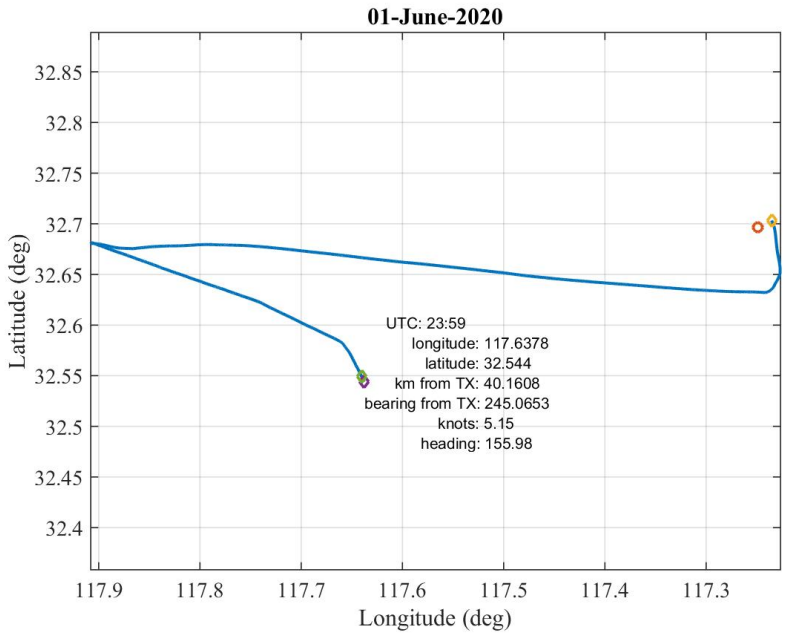


Figure 31: *Acoustic Explorer's* annotated track on 01-June-2020. The transmitter's location is marked with the circle in the upper right.

The following sections analyze the fading at the end of the track at each sounding frequency. Each frequency reports a strong K factor that characterizes the fading as the sum of a large specular component and a small diffuse component. The fading amplitude appears Rician in most of the measurements. The fading phase is linear in most of the measurements. The fading spectrum has a Gaussian shape, despite spectral contamination and noise. Therefore, Rician fading is a credible model for these measurements (See Definition 1). This day's analysis concludes by tabulating the Rician parameters.

4.1.1 4.23 MHz

Figure 32 shows the 4.23 MHz power-delay profile on the ship at 23:55 UTC approximately 40 km from the transmitter. The power-delay profile shows a spike at delay 0.14 ms corresponding to the ground range to the transmitter and identifies the surface wave. The tap is a thin spike approximately 35 dB above the noise and argues that only one ray constitutes this surface wave.

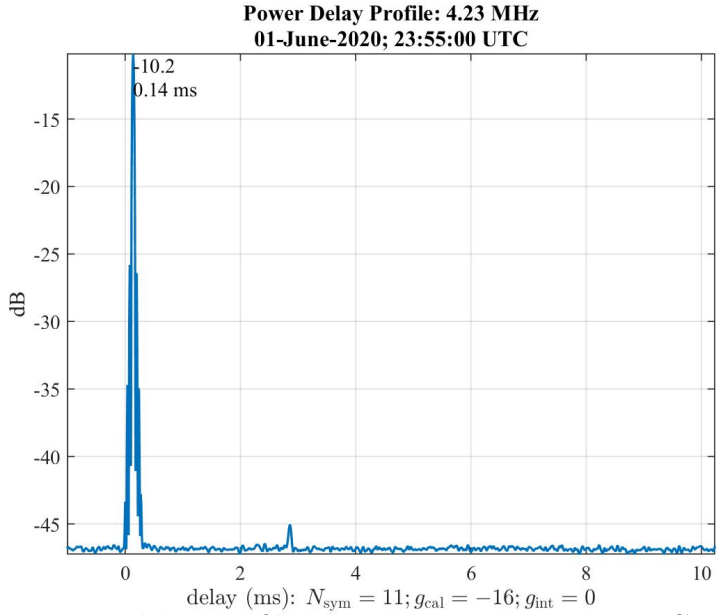


Figure 32: Power-delay profile on 01-June-2020 23:55 UTC at 4.23 MHz.

Figure 33 supports this single-ray conjecture by showing the fading $\{h(t)\}$ on this tap. The upper panel plots the fading amplitude $\{|h(t)|\}$. The amplitude does not show interference patterns characteristic of multiple rays. The lower panel plots the fading phase $\{\angle h(t)\}$ and the Rician parameters estimated by the moments (See Equations 10, 11, 12). The K factor exceeds 20 dB and is consistent with a strong specular component and a weak diffuse component. Therefore, the analysis up to this point supports the generalized Rician of Equation 5 repeated here for convenience:

$$h(t) = e^{j\phi(t)} \{s_{\mathsf{LOS}} + g(t)\} .$$

The phase $\{\phi(t)\}$ is piece-wise linear and a Doppler shift makes no sense. Figure 34 emphasizes that a linear phase does not model this fading by plotting the phase $\{\phi(t)\}$ in the complex plane. The plot shows the phase rotating in two different directions. The next modeling tasks are identifying the amplitude and the spectrum of $\{g(t)\}$.

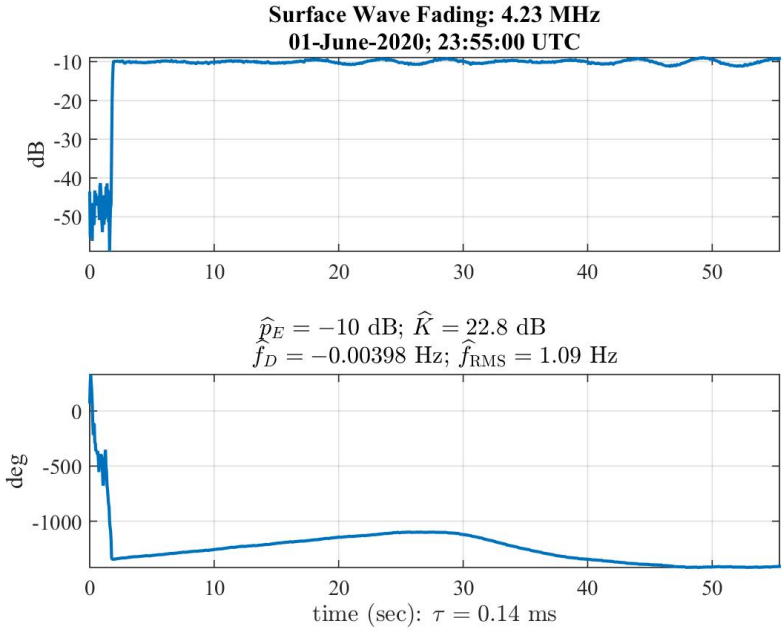


Figure 33: Fading on 01-June-2020 23:55 UTC at 4.23 MHz.

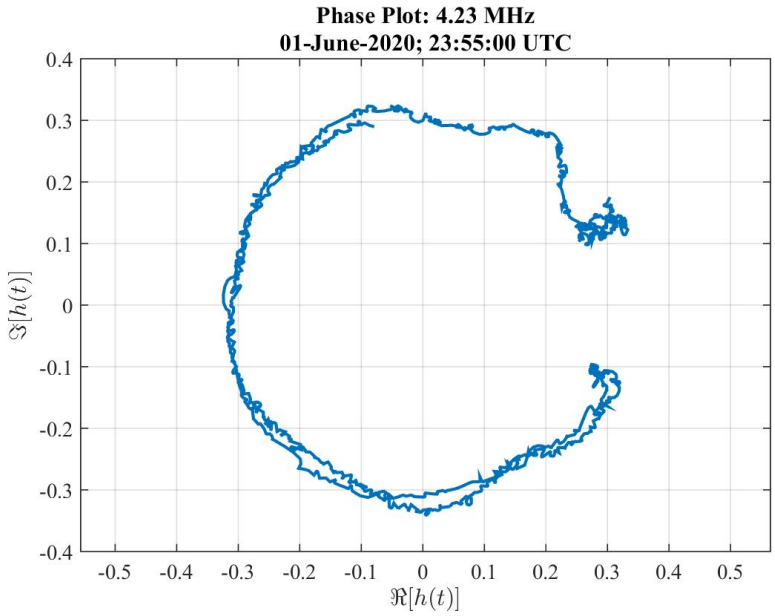


Figure 34: Fading phase on 01-June-2020 23:55 UTC at 4.23 MHz showing forward and backward rotations.

Figure 35 compares the histogram of the amplitude against Rician densities estimated using the moment-based method (γ-Estimate) and fitting to the histogram described in Section 3. The close fit of the Rician density estimated from the moments supports the claim that the fading is Rician. The plot also shows that fitting the histogram with a Rician distribution does get trapped in local minimum. This experiment is the only example showing the failure of the histogram fit.

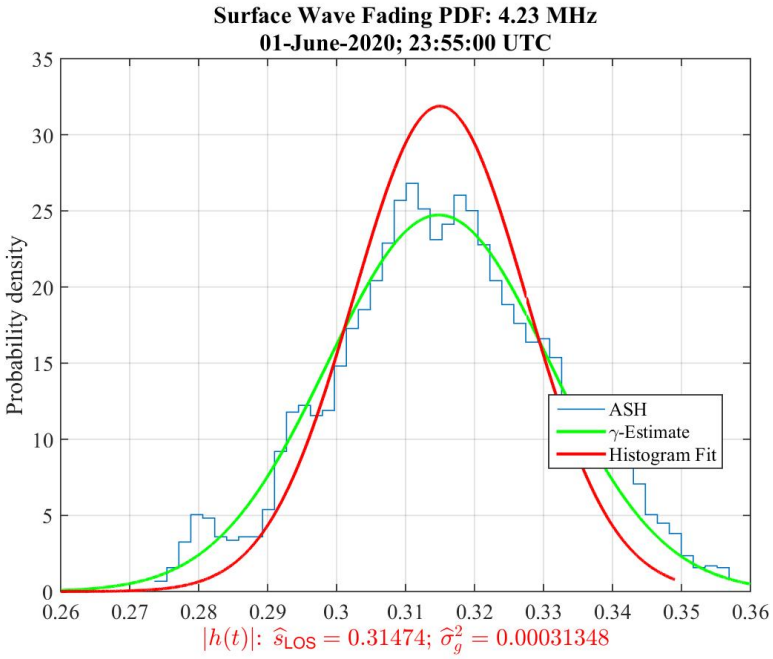


Figure 35: Histograms and Rician estimates; 01-June-2020 23:55 UTC at 4.23 MHz.

Figure 36 shows this fading has a strong spectral spike with spectral width observable down to 50 dB. Consequently, estimates of $\hat{f}_{\mathsf{RMS}}$ will be a good fit to the diffuse component's spectrum. This observation is developed in Section 4.1.2. The figure also hints that harmonics are present starting at 40 dB down and offset by ± 1 Hz. These harmonics are shown in Sections 4.1.2, 4.1.3, and 4.1.5 where the fading spectrum show less noise. The lower noise reveals the Rician spectrum in greater detail and shows the spectral shape f^{-k} of the high-frequency noise.

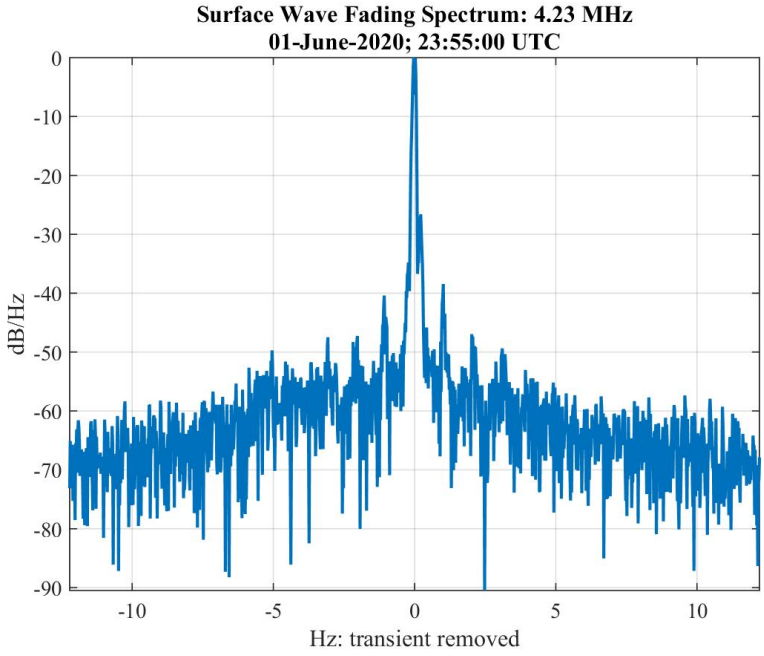


Figure 36: Fading spectrum on 01-June-2020 23:56 UTC at 4.23 MHz.

In summary, the large K factor, the Rician shape of the amplitude, the specular and diffuse components in the spectrum show the Rician process in Equation 5 is a credible fading model.

4.1.2 8.456 MHz

Figure 37 shows the 8.456 MHz power-delay profile measured at the end of the track at 23:56 UTC. The 0.14 ms delay is the same as reported on the power-delay profile at 4.23 MHz. The spike at 8.456 MHz appears "fatter" in comparison with the spike at 4.23 MHz. This fatter appearance is caused by the noise floor being almost 30 dB lower at 8.456 MHz than the noise floor at 4.23 MHz. The lower noise floor exposes more of the surface-wave spike.

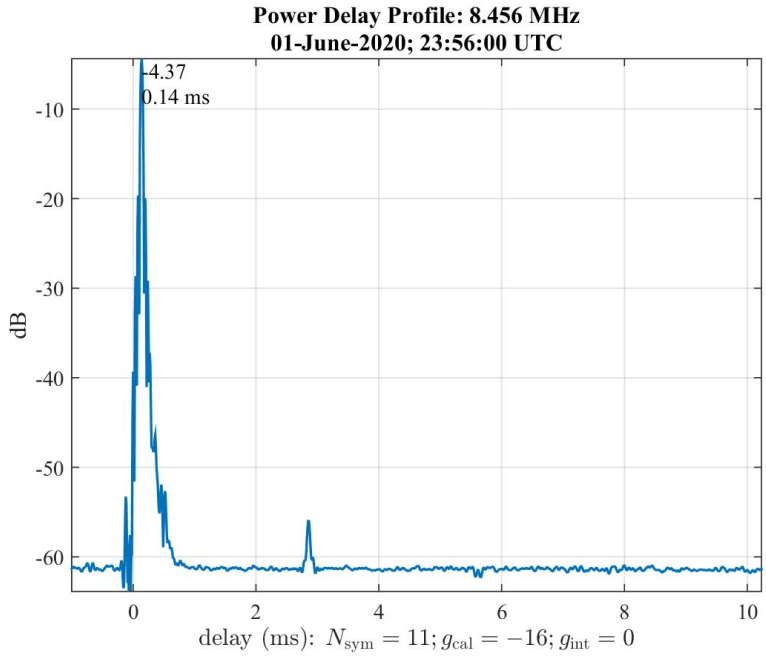


Figure 37: Power-delay profile on 01-June-2020 23:56 UTC at 8.456 MHz

The fading analysis for this surface wave will argue that only one ray constitutes this fading and that fading is Rician despite the *poor* fit to the Rician density. The most significant result from this low-noise experiment is that the spectral plot: the "needle" shape of specular component, the fatter diffuse component visible over 20 dB, and that the diffuse component is well modeled by the Gaussian power spectrum. Of interest to the system engineer are harmonics from an unknown source and the roll-off of the high-frequency noise.

Figure 38 supports the single-ray conjecture by showing the fading $\{h(t)\}$ at this 0.14 ms delay. The upper panel plots the fading amplitude $\{|h(t)|\}$. The amplitude does not show interference patterns characteristic of multiple rays. Instead, the amplitude is modulated by slow variations of the diffuse component $\{g(t)\}$. The lower panel plots the almost-linear phase $\{\angle h(t)\}$ and lists the Rician parameters estimated by the moment methods. The K factor exceeding 20 dB is consistent with a strong specular component and a weak diffuse component. Therefore, the analysis up to this point supports the standard Rician fading with linear phase:

$$h(t) = e^{j2\pi f_D t} \{s_{\mathsf{LOS}} + g(t)\} .$$

The next modeling tasks are identifying the amplitude and the spectrum of $\{g(t)\}$.

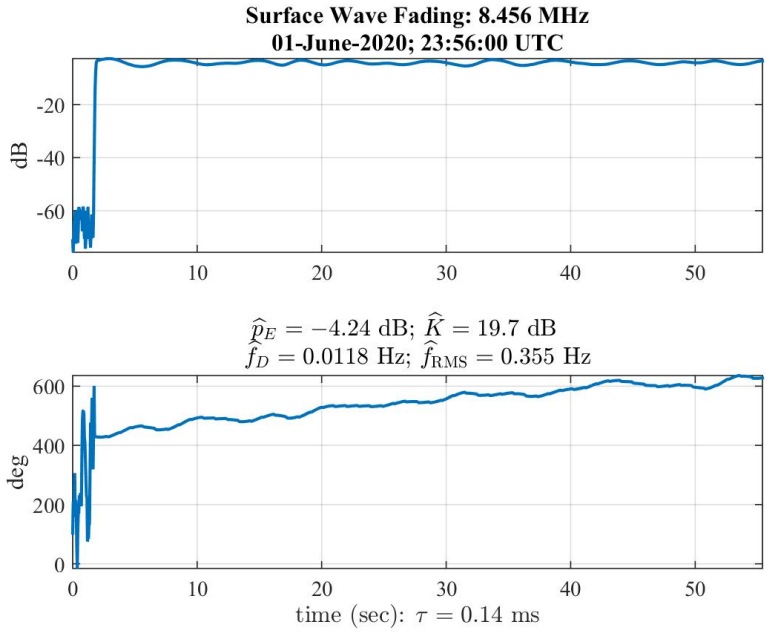


Figure 38: Fading on 01-June-2020 23:56 UTC at 8.456 MHz.

Figure 39 shows this surface-wave's histogram is not well-modeled by a Rician distribution. Figure 40 explains the "lumpy" histogram—the fading only makes half a rotation in the complex plane while the diffuse component is rotating faster to generate relatively wide multiple loops. This histogram and the phase plot show multiple representations of the data are necessary to avoid rejecting a model. In contrast to the non-parametric histogram, both Rician estimators arrive at the same solution.

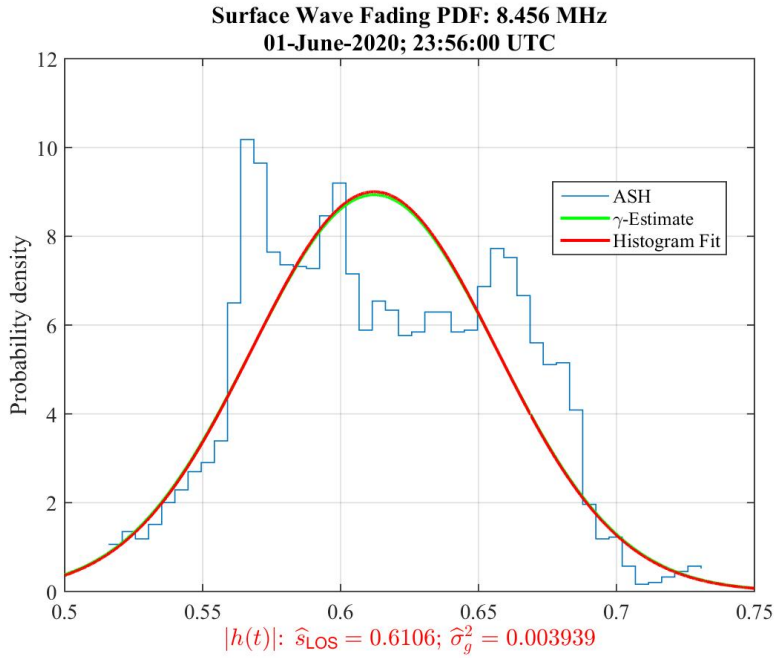


Figure 39: Histogram and Rician estimates; 01-June-2020 23:56 UTC at 8.456 MHz.

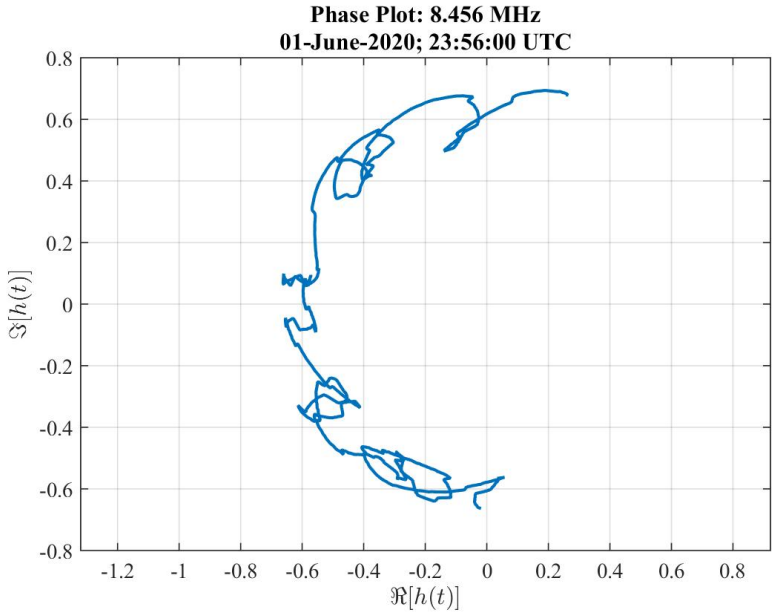


Figure 40: Fading phase on 01-June-2020 23:56 UTC at 8.456 MHz.

Figure 41 offers further insight to this fading. There is a sharp spectral spike marking a well-defined specular component. Approximately 20 dB down the spike ($\widehat{K} = 19.7$ dB), the spike widens to reveal the diffuse spectrum. At 50 dB down, there is a rolling off to the noise floor and ancillary harmonics.

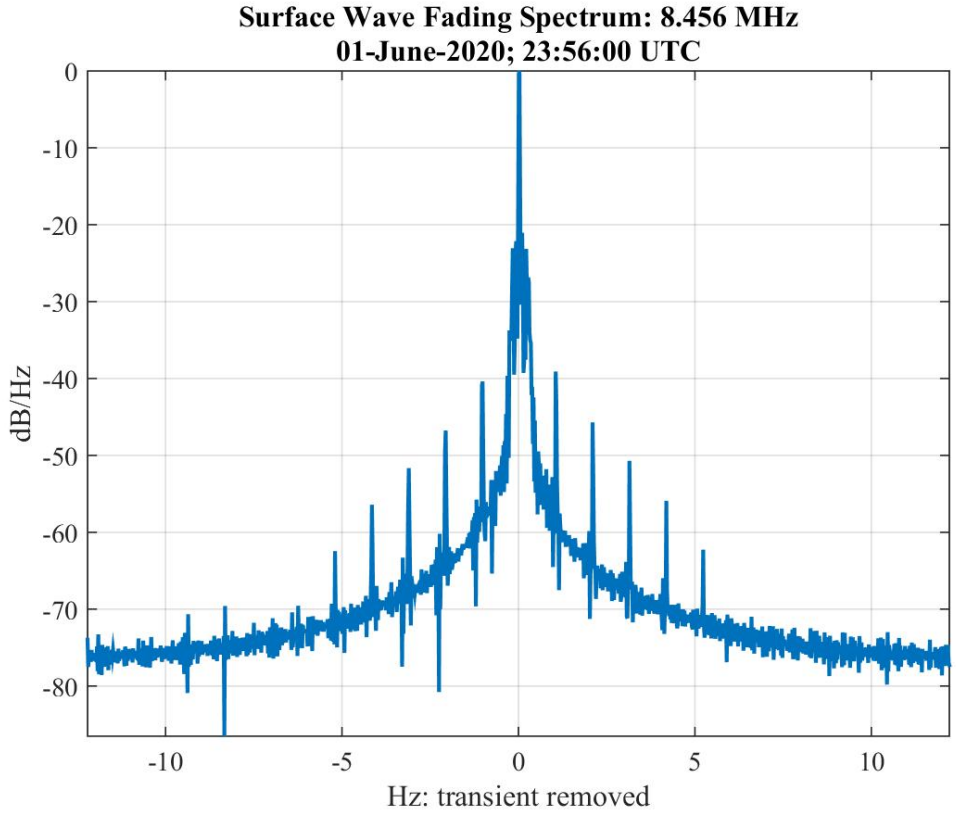


Figure 41: Fading spectrum on 01-June-2020 23:56 UTC at 8.456 MHz.

Figure 42 is a close-up of the diffuse power spectrum. The specular component is removed. The harmonics are labeled and spaced an average of 1.0445 Hz apart. The source of these harmonics is unknown. The close-up also shows a red curve that is a Gaussian function hand-fitted to the main spectral lobe. This Gaussian is a good fit to the low-frequency spectral energy but does not widen out to track the noise that is slowly rolling off with increasing frequency.

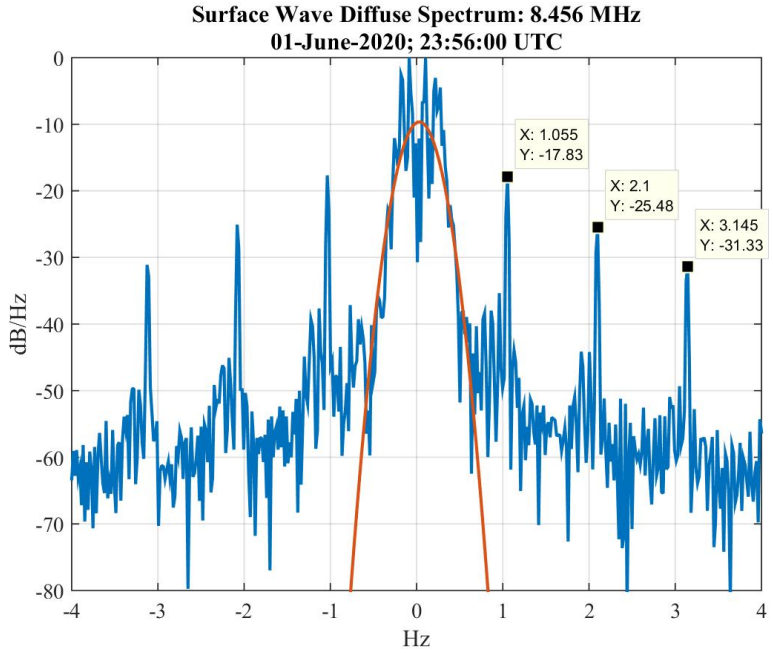


Figure 42: Close-up of the diffuse spectrum on 01-June-2020 23:56 UTC at 8.456 MHz. The red curve is a Gaussian fitted by hand.

Figures 41 and 42 illustrates three issues regarding the diffuse component:

1. The Gaussian spectrum (See Equation 19) is a good fit in the low-frequencies;
2. The noise rolls off as f^{-k} (See Figure 20);
3. The large power difference between the low-frequency energy ($|f| < 1$) and high-frequency energy makes the exact spectral shape a second-order effect when this diffuse component is already $\widehat{K} = 19.7$ dB down from the specular component.

Section 5 reiterates these observations in the summary when discussing surface-wave simulations.

4.1.3 12.45 MHz

Figure 43 plots the 12.45 MHz power-delay profile measured on the ship located 40 km from the transmitted at the end of the track at 23:57 UTC. The 0.14 ms delay is consistent with the ground range to the transmitter. The noise floor is 50 dB below the surface wave peak. The following discussion shows Rician fading is a credible model for this channel and the lower noise reveals the diffuse component's low-frequency bandwidth.

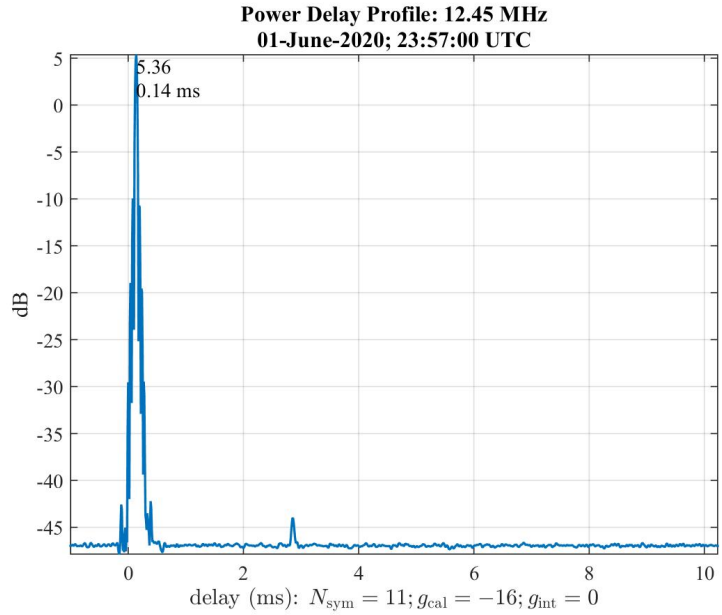


Figure 43: Power-delay profile on 01-June-2020 23:57 UTC at 12.456 MHz.

Figure 44 shows the surface-wave fading $\{h(t)\}$ extracted from the spike at 0.14 ms delay. The figure shows flat fading amplitude, almost linear fading phase, and $\widehat{K}$ exceeds 26 dB. These observations support Rician fading.

Figure 45 compares the fading amplitude's histogram against the Rician densities estimated from the moments and the direct fit to the histogram. Although both parametric fits are nearly identical, the histogram non-Rician.

Figure 46 explains this non-Rician histogram. The phase is subject to a slowly varying diffuse component that makes less than two rotations ($\widehat{f}_D = 0.0342$ Hz or 1.9 rotations). This limited sampling of the fading is not sufficient to smooth the "lumpy" histogram.

Figure 47 shows power spectrum of the fading consisting of a single spike that starts to widens 20 dB down and continues widening down to 60 dB. The harmonics are still present but noise is 60 dB below the peak. These plots argue that the fading is Rician with a slowly varying diffuse component.

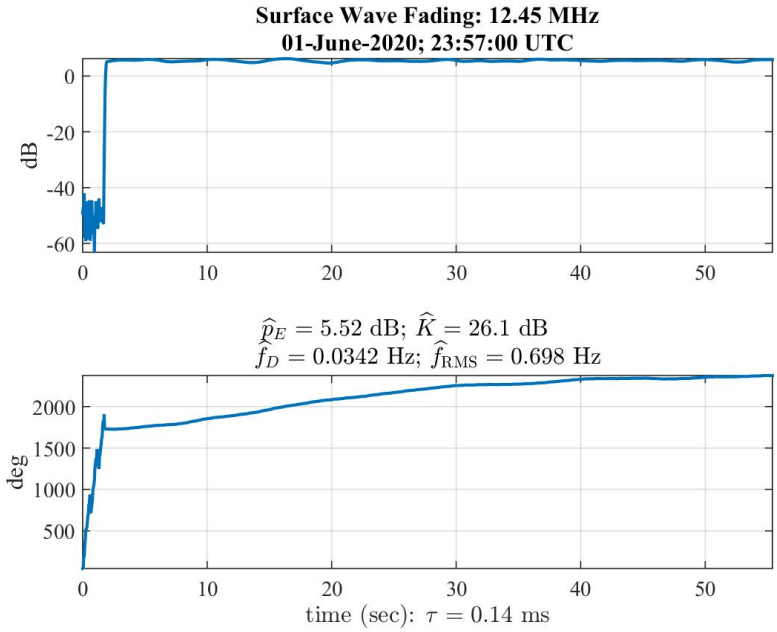


Figure 44: Fading on 01-June-2020 23:57 UTC at 12.456 MHz.

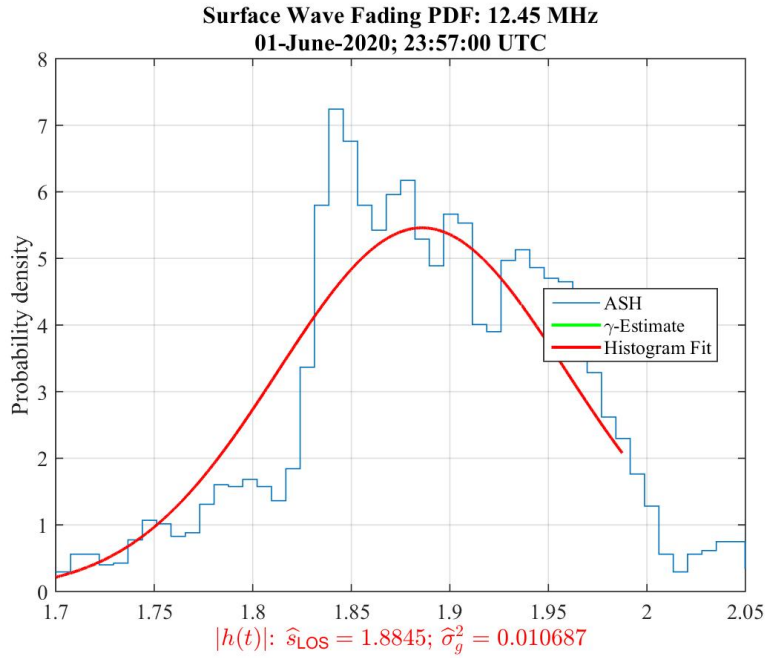


Figure 45: Histogram and Rician estimates; 01-June-2020 23:57 UTC at 12.456 MHz; Rician estimates overlay.

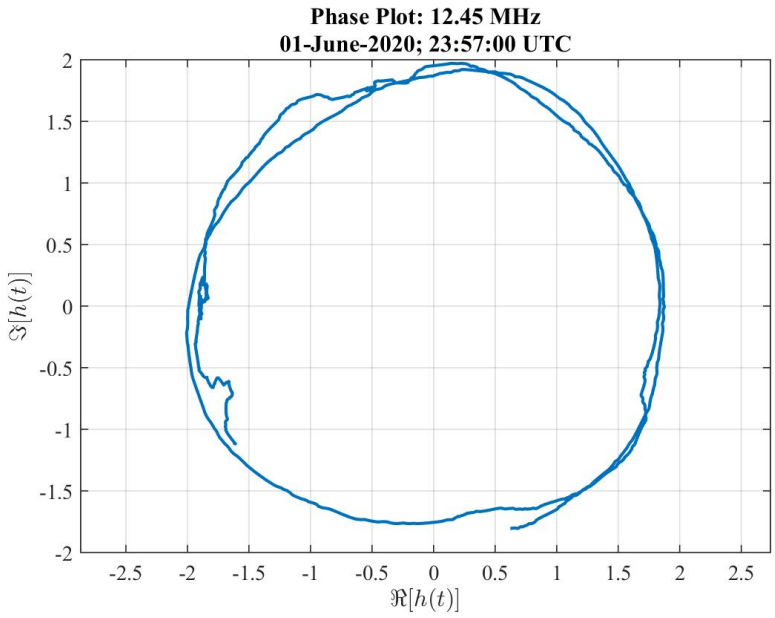


Figure 46: Fading phase on 01-June-2020 23:57 UTC at 12.45 MHz

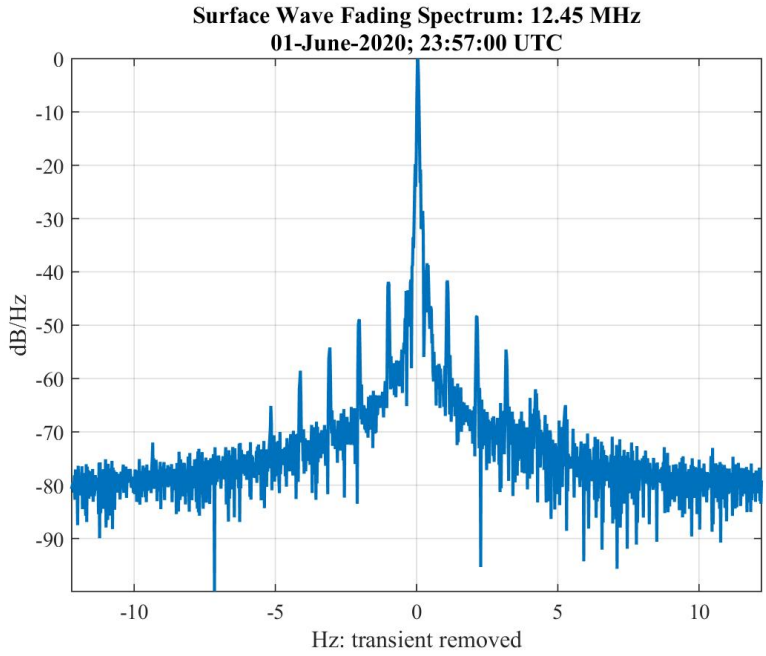


Figure 47: Fading spectrum on 01-June-2020 23:57 UTC at 12.45 MHz

4.1.4 18.474 MHz

Figure 48 plots the 18.474 MHz power-delay profile measured at the end of the track at 23:58 UTC approximately 40 km from the transmitter. Although the surface wave arrives at delay $\tau = 0.14$ ms consistent with the ground range the transmitter, the noise floor is only 25 dB below the surface-wave's peak. The fading analysis argues that this increased noise decreases the K factor, obscures the diffuse component in the spectrum, and produces a nearly ideal Rician histogram.

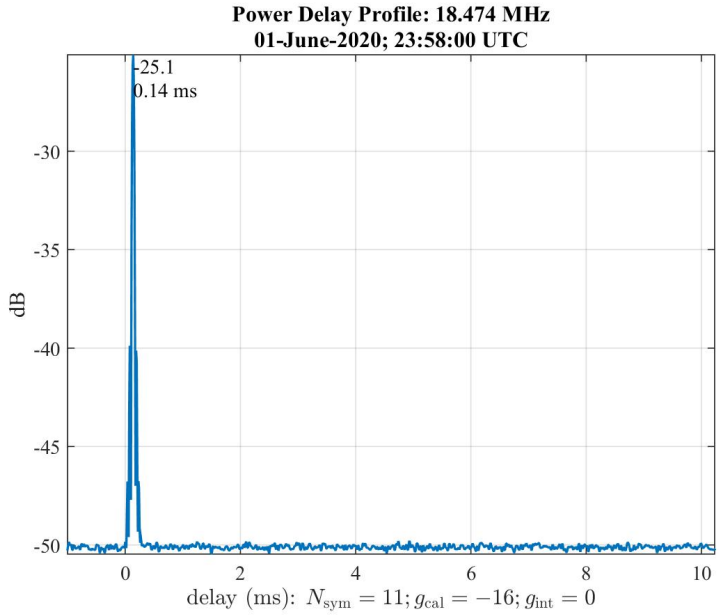


Figure 48: Power-delay profile on 01-June-2020 23:58 UTC at 18.474 MHz.

Figure 49 starts the analysis by showing the fading exhibits almost ideal Rician characteristics: the fading amplitude has a well-defined mean with $\widehat{K} \approx 17$ dB; variations around the mean are slowly varying with a period of approximately 5 seconds; the fading phase is almost linear so the Doppler shift $\widehat{f}_D$ makes sense modeling this phase.

Figure 50 shows power spectrum of the fading consists of a single spike that slightly widens at its base. This spike is consistent with a strong specular component and a weaker diffuse component. Some of the spectral width of the spike—the bandwidth of the diffuse component—is visible under the noise. If the diffuse component was generated by only the visible width of the spike, the RMS bandwidth would be less than 0.5 Hz. However, the moment-based estimate of the RMS bandwidth uses the entire spectrum—including the nearly flat noise—to estimate $\widehat{f}_{\mathsf{RMS}} \approx 2$ Hz. That is, the flat noise biases the RMS bandwidth estimate to the high side.

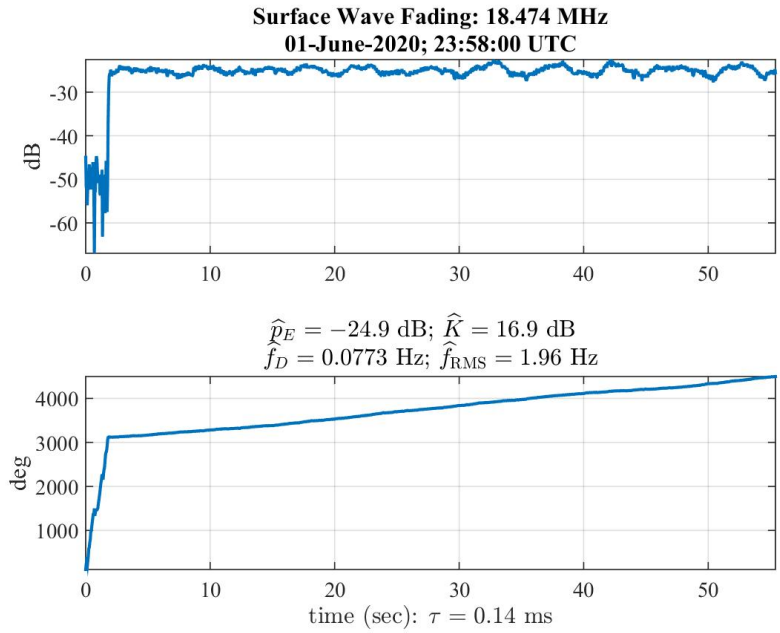


Figure 49: Fading on 01-June-2020 23:58 UTC at 18.474 MHz.

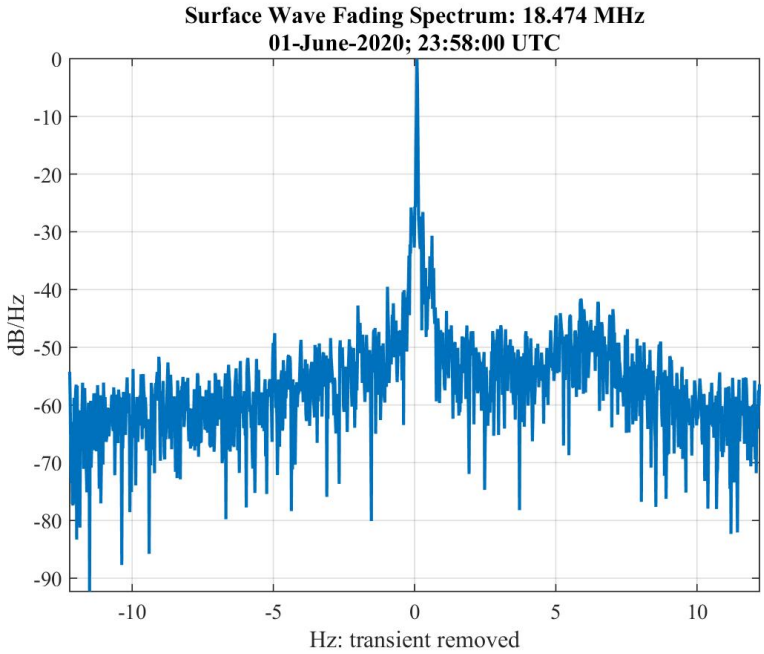


Figure 50: Fading spectrum on 01-June-2020 23:58 UTC at 18.474 MHz.

Figure 51 shows the fading amplitude's histogram is nearly Rician in comparison to the Rician distributions produced by the moment method and the direct fit to the histogram. Figure 52 shows the phase plot and explains this nearly ideal histogram. The figure shows the tight Rician "ring" formed by the phase of the fading. Although the phase only make 4.5 rotations ($\widehat{f}_D$=0.0773 Hz), the increased noise seen in the high-frequency "loops" fill in the gaps between the slowly varying loops. In summary, Rician fading is a credible model for this measurement provided the bias in the RMS bandwidth is recognized.

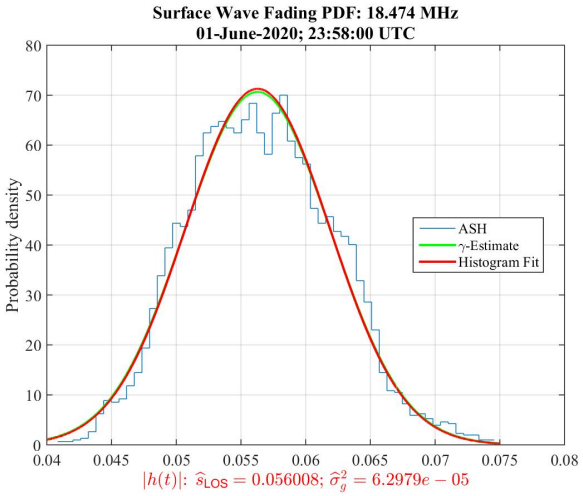


Figure 51: Histogram and Rician estimates; 01-June-2020 23:58 UTC at 18.474 MHz; Rician estimates overlay.

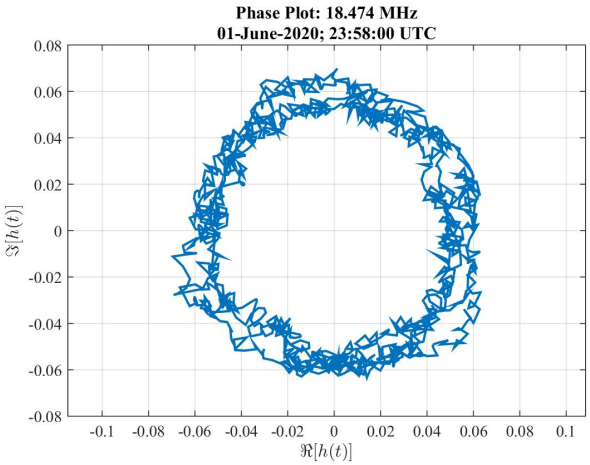


Figure 52: Fading phase on 01-June-2020 23:58 UTC at 18.474 MHz.

4.1.5 23.1 MHz

Figure 53 shows the power-delay profile recorded on the ship at 23:59 UTC when the ship was approximately 40 km from the San Diego transmitter at 23.1 MHz. The profile records a single spike at delay 0.14 ms consistent with the ground range to the transmitter and identifies the surface wave. The noise floor is at least 40 dB below this surface wave so that excellent details of the Rician fading are revealed.

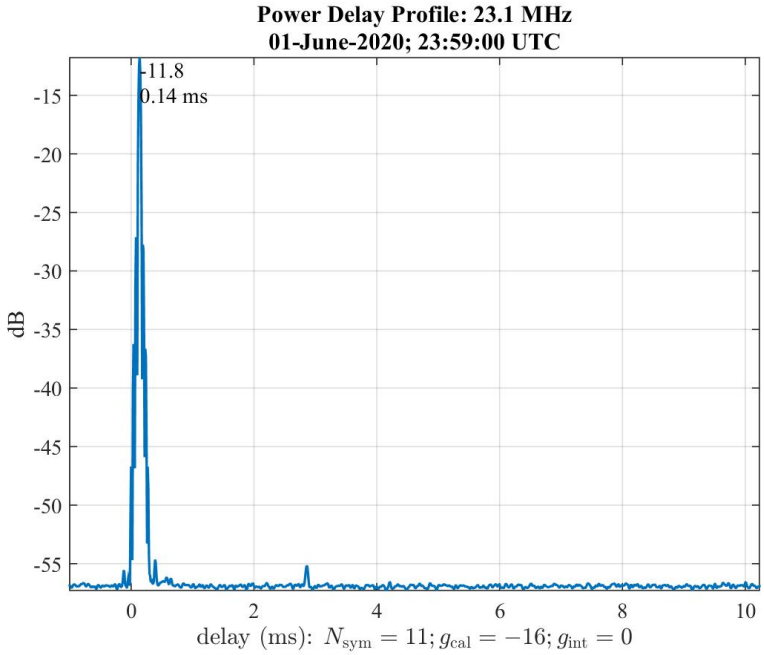


Figure 53: Power-delay profile on 01-June-2020 23:59 UTC at 23.1 MHz.

Figure 54 shows the surface-wave's fading and reports the Rician parameters estimated by the moment-based methods. The fading amplitude is relatively flat having 5-second modulations. The stronger diffuse component reduces the K factor to $\widehat{K} = 17.6$ dB compared to the more noisy fading at 18.474 MHz (See Section 4.1.4). The fading phase is almost linear so the Doppler shift $\widehat{f}_D = 0.09363$ Hz is credible parameter for a linear phase model.

Figure 55 shows the surface-wave's power spectrum. The most prominent feature is the specular component's needle-like spike. The spike widens at 20 dB down and is visible 60 dB down to the noise floor. The lower noise floor reduces the RMS bandwidth to $\widehat{f}_{\mathsf{RMS}} = 0.452$ Hz that is four times smaller than the bandwidth estimated for fading at 18.474 MHz. These low-noise measurements demonstrate higher noise biases the RMS bandwidth estimates. A physics-based model of the RMS bandwidth is one approach to handling this bias.

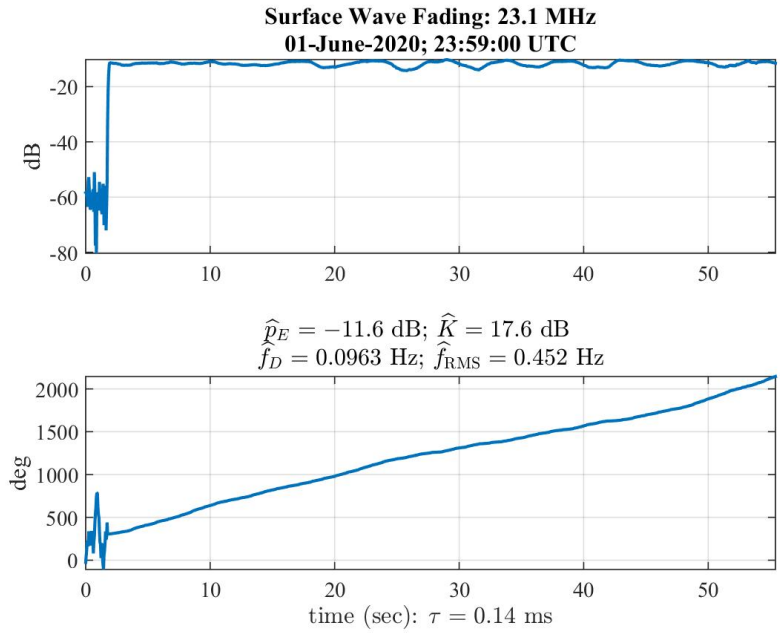


Figure 54: Fading on 01-June-2020 23:59 UTC at 23.1 MHz.

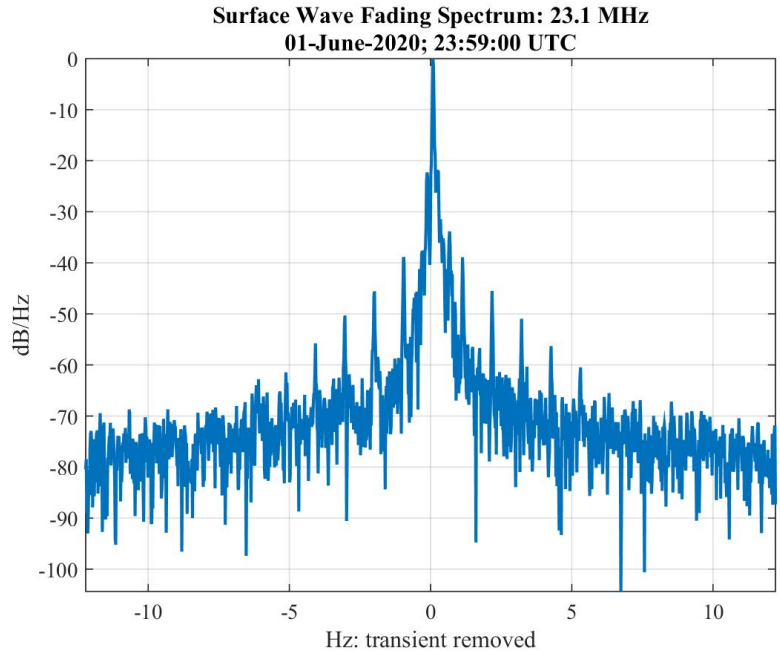


Figure 55: Fading spectrum on 01-June-2020 23:59 UTC at 23.1 MHz.

Figure 56 reports the fading amplitude's histogram and the two Rician densities estimated from the moments ($\widehat{K}$ and $\widehat{p}_E$) and from fitting the histogram with the Rician density. Both Rician estimators produce nearly identical estimates. However, the histogram is a poor representation of a Rician density with its "lumpy" shape. The following phase plot explains the "lumps".

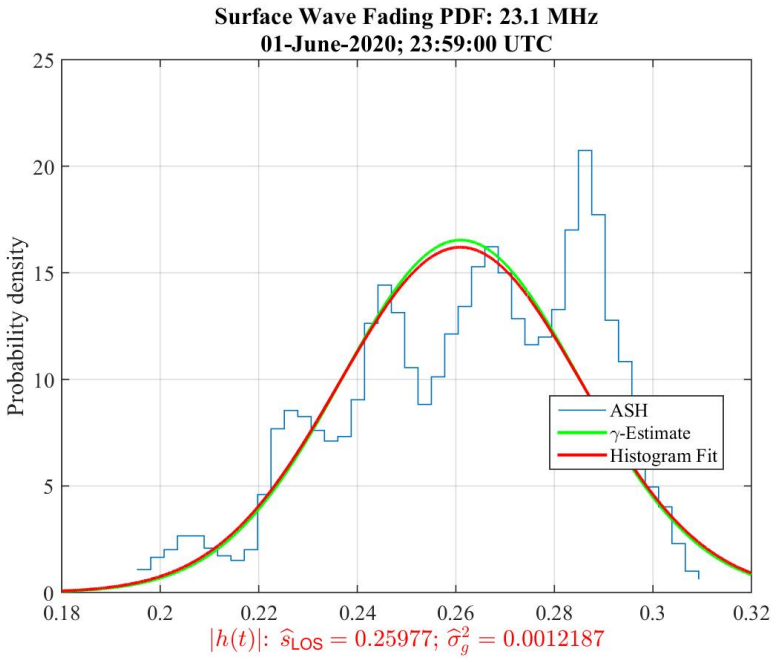


Figure 56: Fading densities on 01-June-2020 23:59 UTC at 23.1 MHz; Rician estimates almost overlay.

Figure 57 plots the surface-wave's fading in the complex plane to explain the non-Rician histogram. The fading spectrum shows diffuse component has most of its spectral energy in the low frequencies. The phase plot shows the diffuse component rotating around the origin with little high frequency noise. Although the phase makes almost 6 rotations ($\widehat{f}_D$=0.0963 Hz), there are too few rotations for a good histogram estimate—each rotation produces an individual "lump" in the histogram.

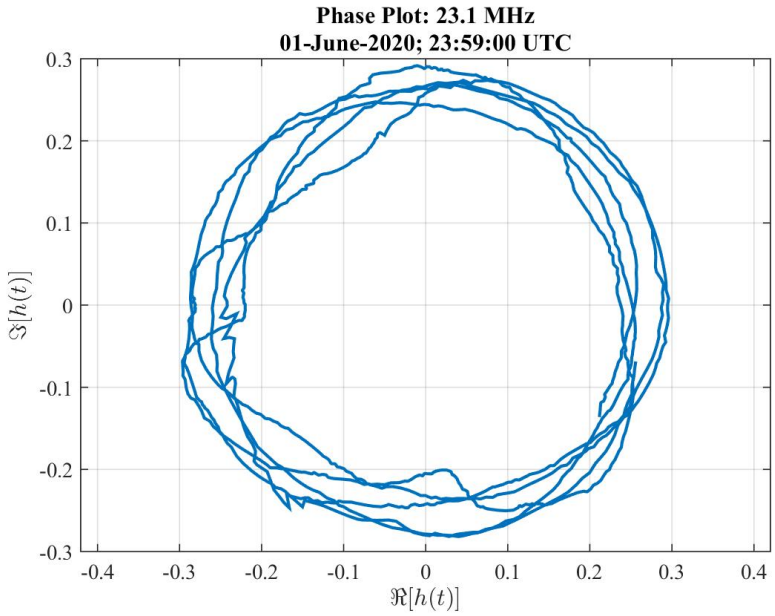


Figure 57: Histogram and Rician estimates; 01-June-2020 23:59 UTC at 23.1 MHz.

In summary, the large K factor and the spectrum argue that Rican fading with the diffuse component having a Gaussian power spectrum is a credible model for this experiment. However, small Doppler shifts requires longer observation times to stabilize the histogram estimate.

4.1.6 Discussion

This section tabulates the Rician fading parameters $\{K, f_D, f_{\mathsf{RMS}}\}$ extracted at 4.23, 8.456, 12.45, 18.474, and 23.1 MHz on 01-June-2020 starting at 23:55 UTC. Each table compares the Rician estimates using the following methods detailed in Section A:

Moment Method: Estimates the Doppler shift f_D, the Rician K factor, and the RMS bandwidth f_{RMS} using Equations 10, 11, and 12.

Filtering Method: Employs a narrowband filter to "separate" the specular component from the diffuse component. The K factor is estimated from the separated components is an upper bound on the actual K factor for a Rician process (Equation 24). The Doppler shift f_D is estimated from the specular component using Equation 10. The RMS bandwidth f_{RMS} is estimated from the diffuse component using the Rayleigh level-crossing method (Equation 27).

Histogram Method: Estimates the K factor by fitting a Rician density to the histogram of the fading amplitude $\{|h(t)|\}$ (Equations 13, 14). The Doppler shift is computed using Equation 10. The RMS bandwidth f_{RMS} using the Rician level-crossing method of Dana [21] in Equation 28.

K **Factor:** Each of the tables shows the K factor estimates are in good agreement and do not exceed the upper bound (See Section 3). The large K factors and well-defined Rician rings in the phase plots point to Rician fading:

Frequency (MHz)	4.23	8.456	12.45	18.474	23.1
$\widehat{K}$ (Hz)	23	20	26	17	18

Doppler Shifts: Previous HF analysis verified by the Doppler shift estimates $\widehat{f_D}$ by comparing the predicted vehicle velocity $\widehat{v} = -\lambda \widehat{f_D}$, where λ is the wavelength of the carrier, against the vehicle velocity recorded in the GPS file [16], [17]. For the ground vehicles traveling at freeway speeds, both velocity estimates agreed within two digits. These surface wave experiments do not exhibit the same accuracy. Figure 31 determines the relative velocity between the transmitter and ship as almost zero:

$$v_{\mathsf{GPS}} = 0.0453 \quad [\mathrm{m/s}].$$

The slightly positive speed means the distance is increasing between the ship and transmitter. This increasing distance implies *negative* Doppler shifts—not the slightly *positive* $\widehat{f_D}$ recorded in Tables 3, 4, 5, and 6

Frequency (MHz)	8.456	12.45	18.474	23.1
$\widehat{f}_D$ (Hz)	0.0118	0.0342	0.0773	0.0963
$\widehat{v}$ (m/s)	−0.42	−0.82	−0.13	−0.13

The Doppler shift at 4.23 MHz is not linear so is removed from the estimates. With $\widehat{f}_D > 0$, the resulting velocity estimates $\widehat{v}$ are negative and contradict the GPS velocity estimates. These Doppler issues are unique to this day's experiment.

RMS bandwidth: The spectral plots show that when more of the diffuse component is exposed, such as the lower spectral noise at 8.456, 12.45, and 23.1 MHz, $\widehat{f}_{\mathsf{RMS}}$ tends to the lower frequencies. Otherwise, larger spectral noise biases $\widehat{f}_{\mathsf{RMS}}$ to the high side for 4.23 and 18.474 MHz:

Frequency (MHz)	4.23	8.456	12.45	18.474	23.1
$\widehat{f}_{\mathsf{RMS}}$ (Hz)	1.1	0.4	0.7	1.9	0.5

This bias and spectral shape of the diffuse component is mitigated by the dominance of the specular component. These issues are reviewed in Section 5.

Table 2: Rician fading estimates on 01-June-2020 23:55:00 UTC; 4.23 MHz.

01-June-2020 23:55:00 UTC 4.23 MHz 40 km 0.14 ms			
K (dB)	f_D (Hz)	f_{RMS} (Hz)	Method
22.7804	−0.0040	1.0879	Moments
25.3283	−0.0037	2.9397	Filtering+Rayleigh Level Crossing
24.9970	−0.0040	1.0645	Histogram+Rician Level Crossing

Table 3: Rician fading estimates on 01-June-2020 23:56:00 UTC; 8.456 MHz.

01-June-2020 23:56:00 UTC 8.456 MHz 40 km 0.14 ms			
K (dB)	f_D (Hz)	f_{RMS} (Hz)	Method
19.695	0.011752	0.3548	Moments
22.576	0.011618	1.3538	Filtering+Rayleigh Level Crossing
19.761	0.011752	0.2094	Histogram+Rician Level Crossing

Table 4: Rician fading estimates on 01-June-2020 23:57:00 UTC; 12.45 MHz.

01-June-2020 23:57:00 UTC 12.45 MHz 40 km 0.14 ms			
K (dB)	f_D (Hz)	f_{RMS} (Hz)	Method
26.112	0.034235	0.69836	Moments
28.386	0.034085	1.3409	Filtering+Rayleigh Level Crossing
25.215	0.034235	NaN	Histogram+Rician Level Crossing

Table 5: Rician fading estimates on 01-June-2020 23:58:00 UTC; 18.474 MHz.

01-June-2020 23:58:00 UTC 18.474 MHz 40 km 0.14 ms			
K (dB)	f_D (Hz)	f_{RMS} (Hz)	Method
16.8953	0.0773	1.9586	Moments
18.8713	0.0716	3.4554	Filtering+Rayleigh Level Crossing
16.9730	0.0773	1.8036	Histogram+Rician Level Crossing

Table 6: Rician fading estimates on 01-June-2020 23:59:00 UTC; 23.1 MHz.

01-June-2020 23:59:00 UTC 23.1 MHz 40 km 0.14 ms			
K (dB)	f_D (Hz)	f_{RMS} (Hz)	Method
17.6155	0.0963	0.4521	Moments
20.0618	0.0958	1.1217	Filtering+Rayleigh Level Crossing
17.4328	0.0963	0.2677	Histogram+Rician Level Crossing

4.2 02-June-2020

Figure 58 shows the ship's "V"-shaped track starting nearest to San Diego:

Start	00:00 UTC	40 km
End	23:59 UTC	133 km

Figure 59 compares all the spectrograms. These spectrograms show the channel-sounding signal at the start of the experiment and decreasing below the noise floor as the ship increases the distance from the transmitter. This decrease of the channel-sounding signal is seen also in the delay spread functions of Figure 60. These functions show that signal is recoverable until 19:00 UTC. At this time, the ship is in the middle of the "dog leg" and approximately 122 km from the transmitter.

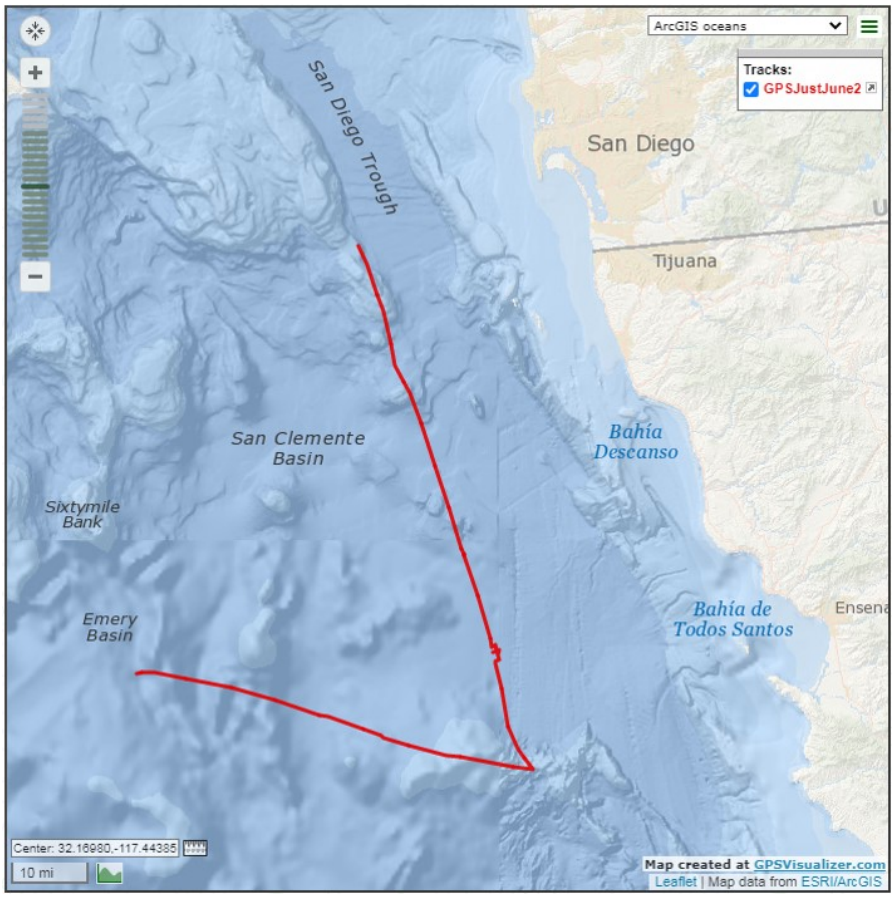


Figure 58: *Acoustic Explorer's* track on 02-June-2020.

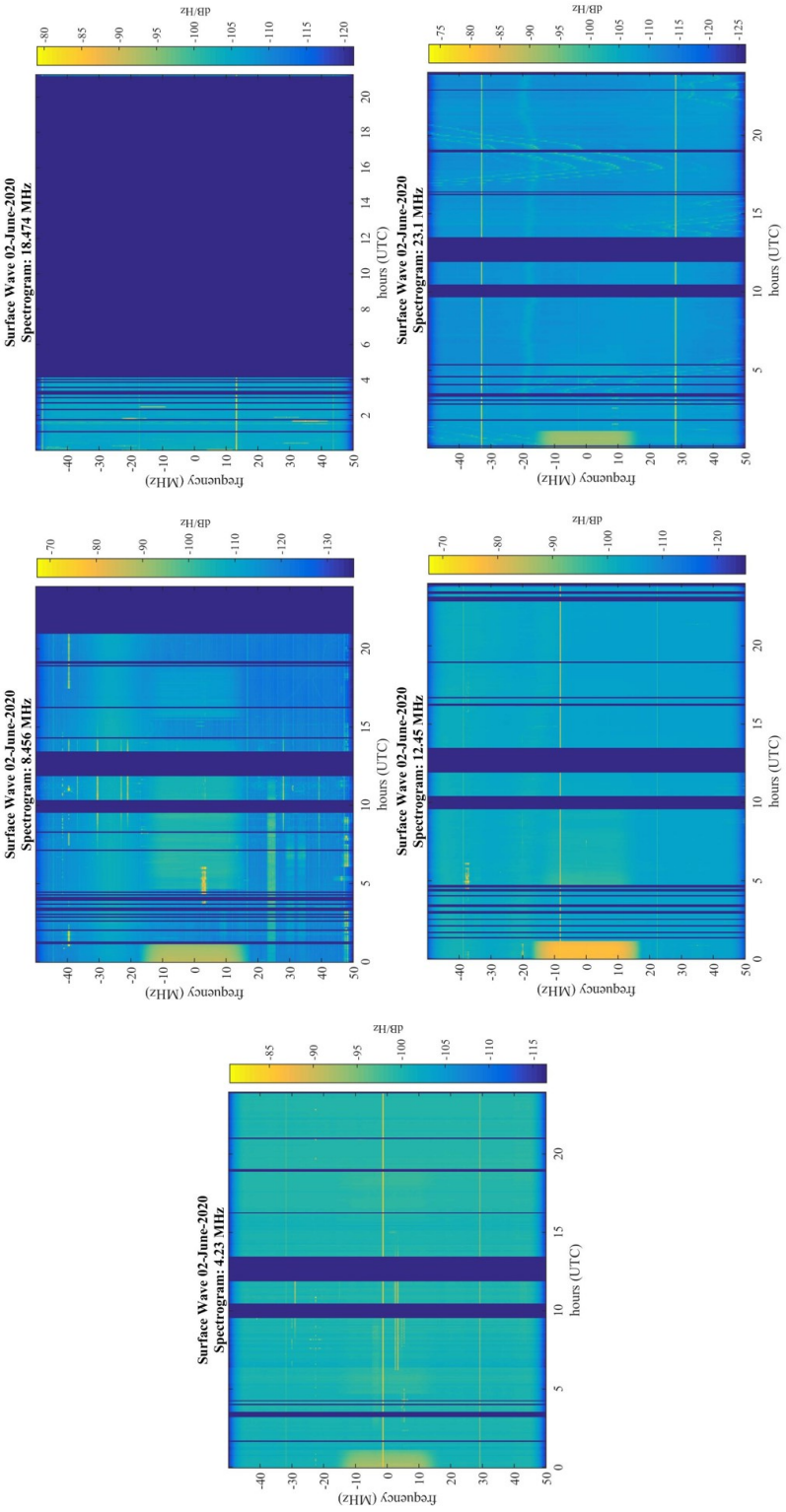


Figure 59: Spectrograms measured on 02-June-2020.

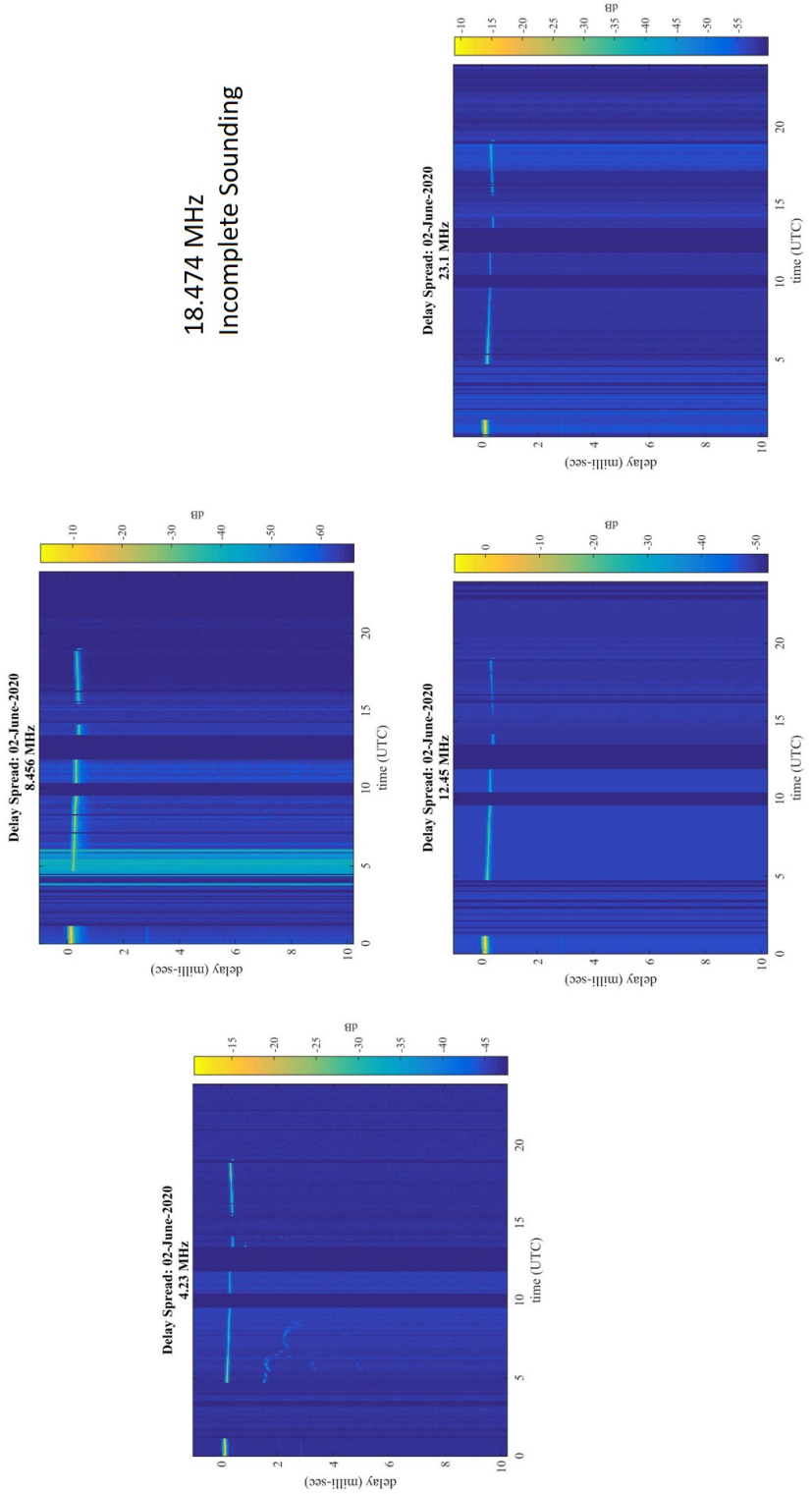


Figure 60: Delay spread functions measured on 02-June-2020.

Figure 61 shows a sounding location that is 68.7803 km from the transmitter in San Diego at 06:02:01 UTC. Figure 62 shows the power-delay profile at the sounding location measured at 4.23 MHz at the same time. The figure reports the "spike" rising +20 dB over the noise at delay 0.24 ms that is a good approximation to the theoretical delay:

$$0.24 \approx \left.\frac{d_G}{c_0}\right|_{d=68.7803} = 0.2293 \quad [\text{ms}].$$

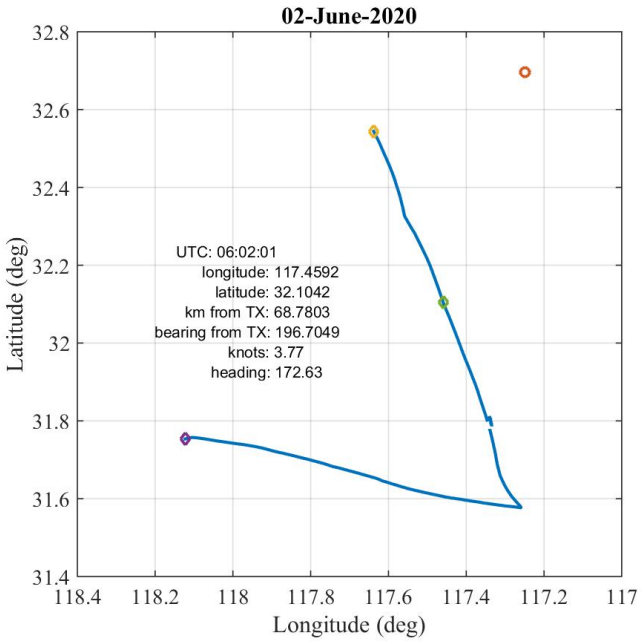


Figure 61: *Acoustic Explorer's* annotated track on 02-June-2020. Transmitter is the circle in the upper right.

The following sections report on the surface-wave fading measured at this 69 km range over the HF sounding frequencies. Each frequency reports a strong Rician K, good fits the Rician density, and little spectral contamination in the fading power spectrum. This day's soundings are tabulated for HF channel emulation in the final section.

4.2.1 4.23 MHz

Figure 62 shows the power-delay profile measured at 4.23 MHz when the ship is located 69 km from the transmitter in San Diego at 06:00 UTC. The plot shows a spike at delay 0.24 ms consistent with the ground range between the ship and transmitter:

$$\tau_G = \frac{d_G}{c_0} = 0.23 \quad [\text{ms}].$$

The other spikes in the power-delay profile are identified as HF skywaves. The value of this power-delay profile is to show the transition from surface wave to the HF-NVIS signal. Well-designed HF radios gather all signal power—from surface wave and skywaves—to maximize the SNR. Adding antennas that respond to the HF-NVIS skywaves opens the possibility for MIMO performance boost [14], [27], [61].

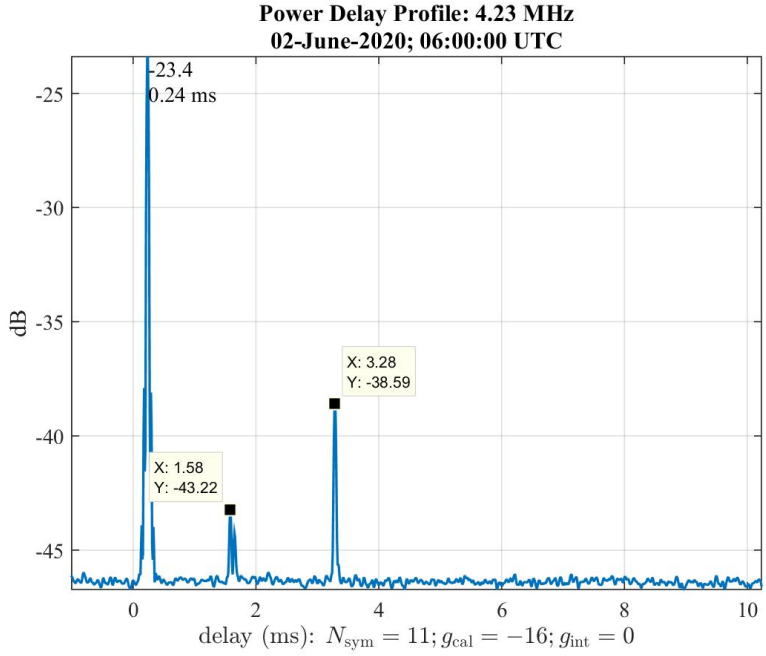


Figure 62: Power-delay profile on 02-June-2020 06:00 UTC at 4.23 MHz.

This section undertakes a fading analysis of this surface wave. The first task is to identify the other spikes in this power-delay profile. This identification is on the next page. The rest of the section verifies that the fading, spectrum, phase plots, and fading densities support the argument that the surface-wave fading is Rician consisting of a strong specular component and a weaker diffuse component. The noise limits the analysis of the diffuse component at this frequency.

Figure 63 shows the ionogram measured at Point Arguello, CA on 02-June-2020 at 06:00 UTC. This ionogram explains the spikes arriving after the surface wave as reflections from the layers at virtual height (km) over 4.23 MHz. The double spikes at $\tau_2 = 1.58$ ms are likely the X- and O-Modes refracting from the layer at 225 km:

$$\tau_2 = 1.58 \approx \left.\frac{2d}{c_0}\right|_{d=225} = 1.5 \quad [\text{ms}].$$

The third spike at $\tau_3 = 3.28$ ms is likely refraction from the layer at 500 km marked by the blue haze:

$$\tau_3 = 3.28 \approx \left.\frac{2d}{c_0}\right|_{d=500} = 3.33 \quad [\text{ms}]$$

or, equivalently, the oblique refraction from the Northeast (See [72]).

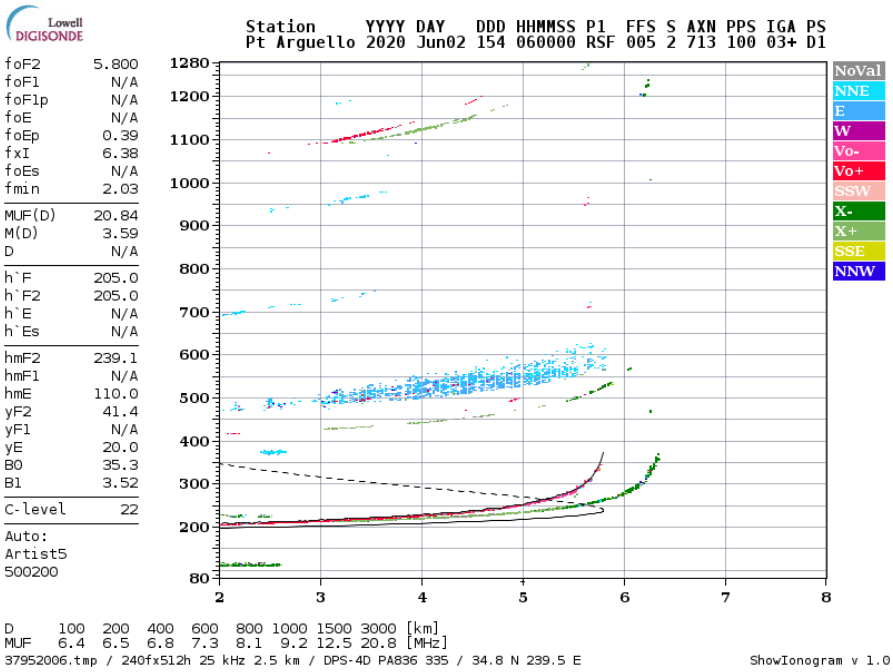


Figure 63: Ionogram at Point Arguello, CA; 02-June-2020 at 06:00 UTC.

All the spikes in the power-delay profile are arise from either the surface wave or HF skywaves. The discussion turns to surface-wave fading.

Figure 64 shows the surface-wave fading extracted at the 0.24 ms delay. The amplitude has a well-defined mean with relatively small and slow oscillations in high-frequency noise. The relatively small diffuse component increases the K factor ($\widehat{K} = 19.5$ dB) in comparison to the fading measured at 8.456 and 12.4 MHz. The phase is linear with Doppler shift $\widehat{f}_D = +0.00213$ Hz. However, the ship is moving *away* from the transmitter so that the Doppler shift should be *negative*. This problem is observed in the 4.23 MHz measurement on 01-June-2020. In fact, all the channel soundings at 4.23 MHz show a positive bias in the Doppler shift. Section 5 quantifies this phenomenon.

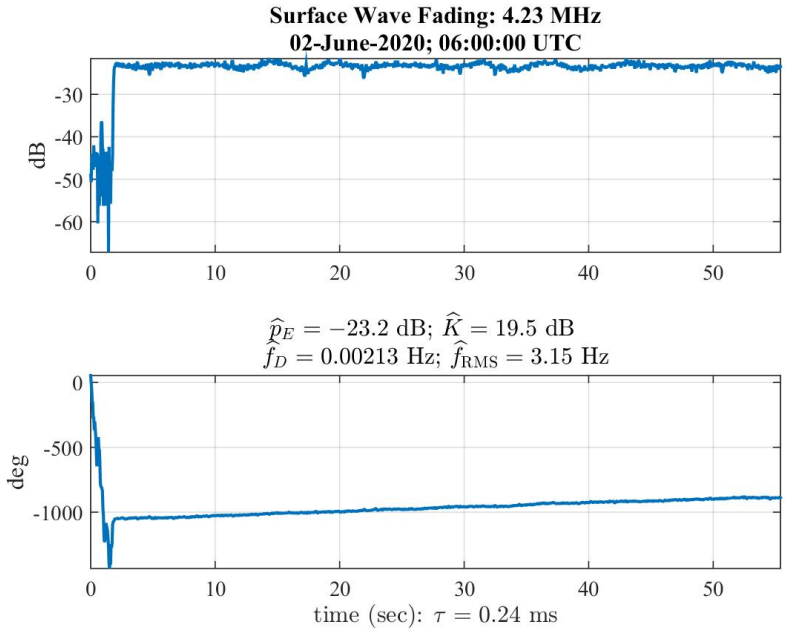


Figure 64: Fading on 02-June-2020 06:00 UTC at 4.23 MHz.

Figure 65 shows the fading spectrum. There is a narrowband "spike" that corresponds to the specular component. The spike widens 30 dB down from the peak to show part of the diffuse component. The noise floor starts at 40 dB down and obscures the low-frequency spectral energy in the diffuse component. The spectral energy of the diffuse component is more visible at 8.456 and 23.1 MHz.

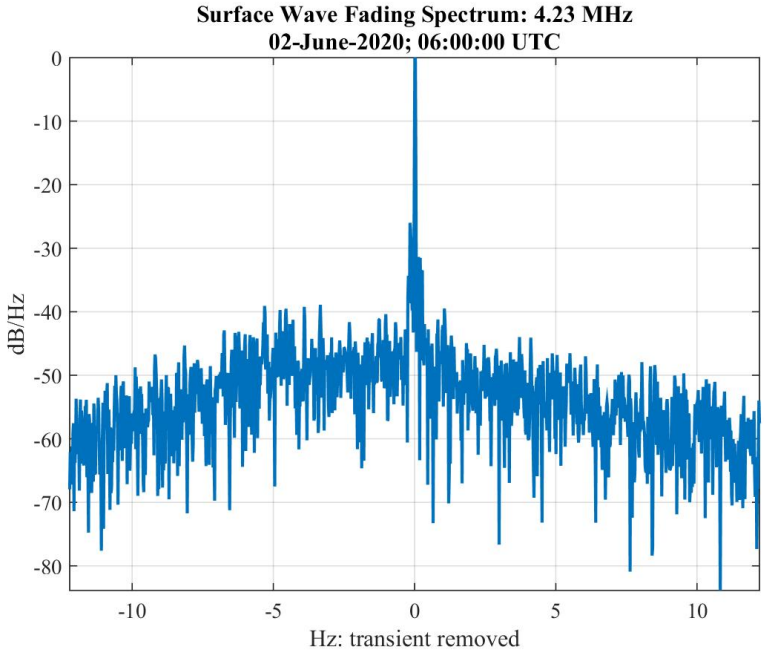


Figure 65: Fading spectrum on 02-June-2020 06:00 UTC at 4.23 MHz.

Figure 66 compares the histogram of the fading amplitude $\{|h(t)|\}$ against the Rican densities estimated from the moments and histogram fitting. Both Rician densities align and fit the histogram.

Figure 67 reports that the small Doppler shift only produces half a rotation in the phase plot. Consequently, the histogram is really showing that the diffuse component appears to have Gaussian distribution because of the high-frequency noise in the phase plot. The fading spectrum shows that this noise arises from the high noise floor. Other experiments on this day show less noise to reveal the diffuse component's spectrum in more detail. In this context, the fading at 4.23 MHz is likely Rican with a strong K factor but with the RMS bandwidth biased high by the noise floor.

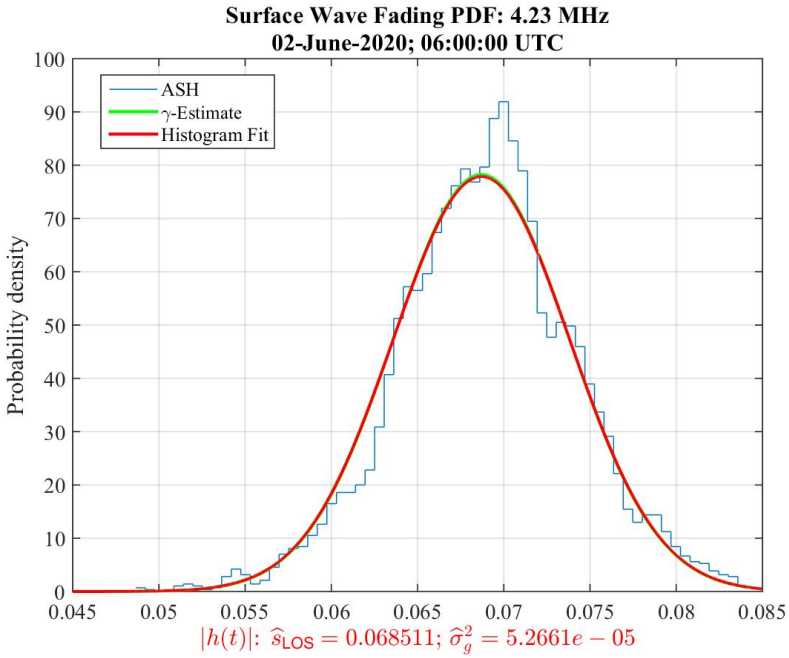


Figure 66: Histogram and Rician estimates; 02-June-2020 06:00 UTC at 4.23 MHz; Rician estimates overlay.

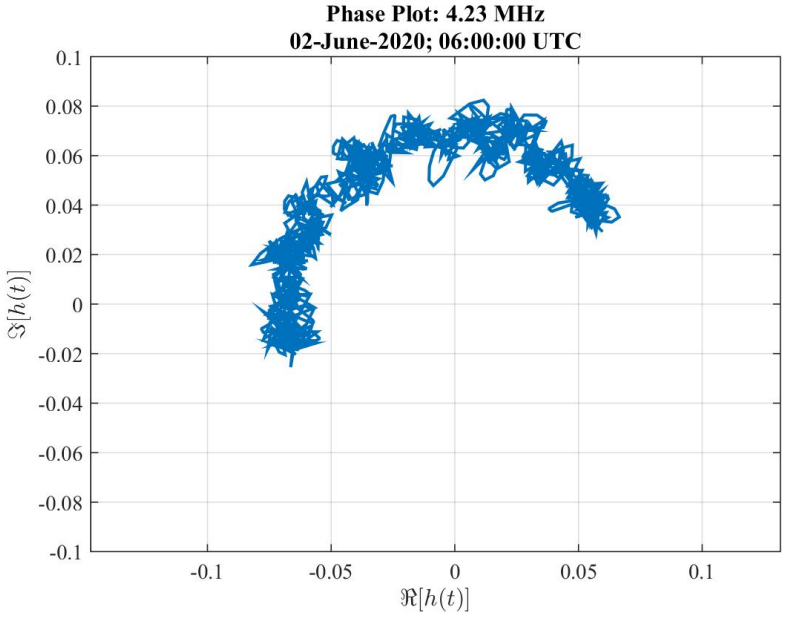


Figure 67: Fading phase on 02-June-2020 06:01 UTC at 4.23 MHz.

4.2.2 8.456 MHz

Figure 68 plots the power-delay profile measured at 8.456 MHz recorded on the ship at 06:01:01 UTC. The 0.23 ms delay is still consistent with the ground range to the transmitter and identifies the surface wave. Althought the noise floor is only 19 dB below the surface-wave's peak, this increased noise does not change the Rician fading model but does bias RMS bandwidth estimates.

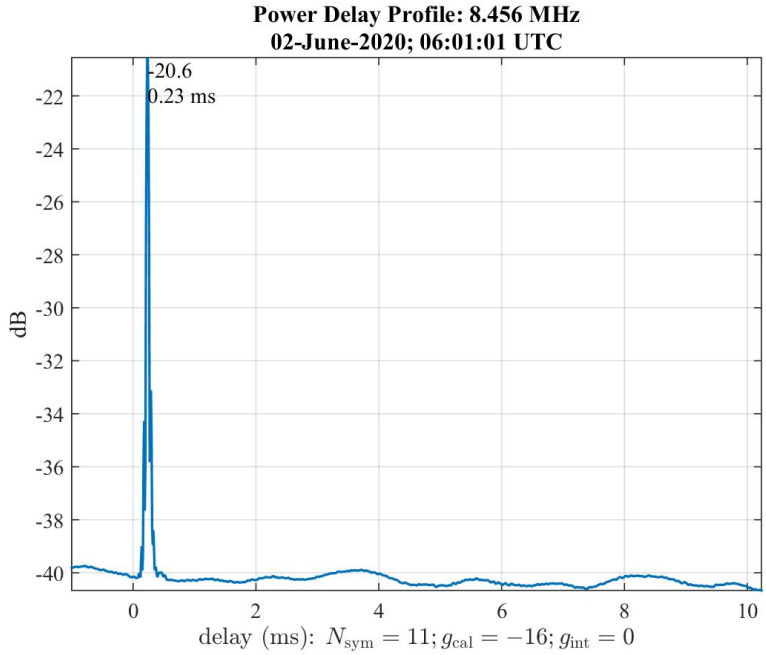


Figure 68: Power-delay profile on 02-June-2020 06:01:01 UTC at 8.446 MHz.

Figure 69 plots the surface-wave fading extracted from the delay at 0.23 ms. The amplitude shows a well-defined mean with 2-second oscillations and high-frequency noise. The extra energy in the diffuse component reduces the K factor ($\widehat{K} = 16.7$ dB) in comparison to 4.23 MHz. The phase is almost linear so that the *negative* Doppler shift $\widehat{f}_D = -0.0105$ Hz is a credible model for the linear phase and is consistent with the ship steaming *away* from the transmitter.

Figure 70 shows the surface-wave's ower spectrum. The spectrum displays a well-defined "spike" that corresponds to the specular component that widens out 30 dB down. This low-frequency spectral energy corresponds to the slow variation seen in the amplitude. The spectrum also shows a noise floor that starts around 40 dB. This high-frequency noise corresponds to the high-frequency noise in amplitude.

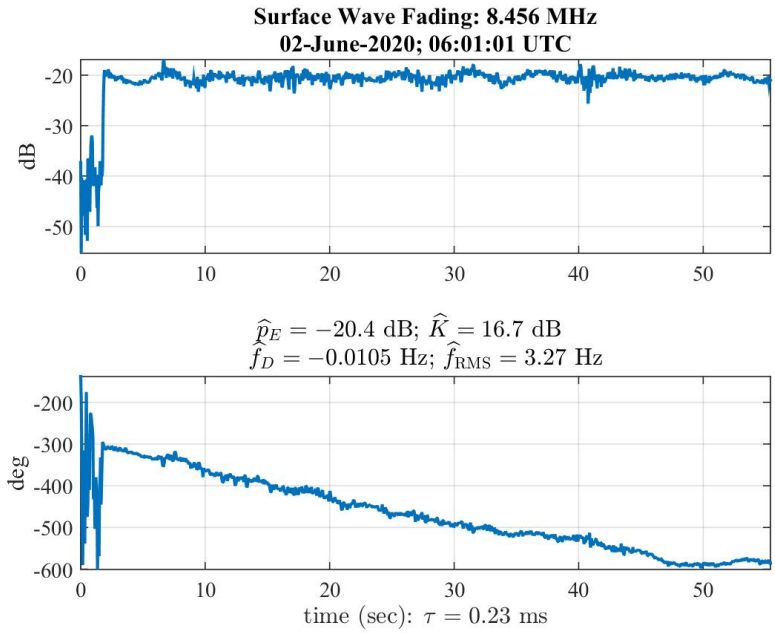


Figure 69: Fading on 02-June-2020 06:01:01 UTC at 8.446 MHz.

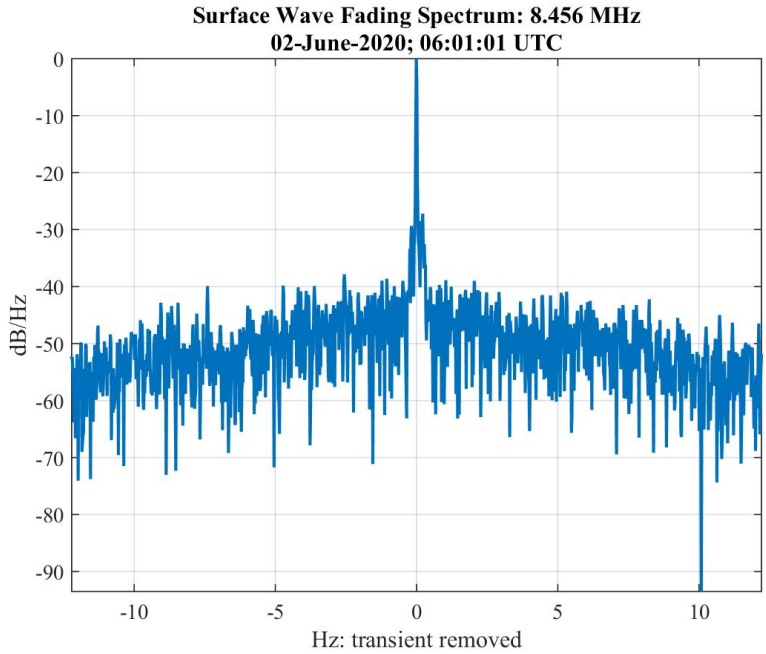


Figure 70: Fading spectrum on 02-June-2020 06:01:01 UTC at 8.456 MHz.

Figure 71 compares the surface-wave's amplitude histogram against the Rician densities estimated from the moments and the direct fit to the histogram. Both Rician densities are almost identical and the histogram itself is close to Rician. Comparing K-factor estimates quantifies the "almost" between these two estimators:

$$16.7 = \widehat{K} \approx \frac{|\widehat{s}_{\mathsf{LOS}}|^2}{\widehat{\sigma}_g^2} = 16.8 \quad [\text{dB}].$$

The leftmost term is the moment estimate from Figure 69. The rightmost term is from the Histogram Fit. The 0.1-dB error shows the K-factor estimates are credible. The phase plot offers additional insight into this surface-wave fading.

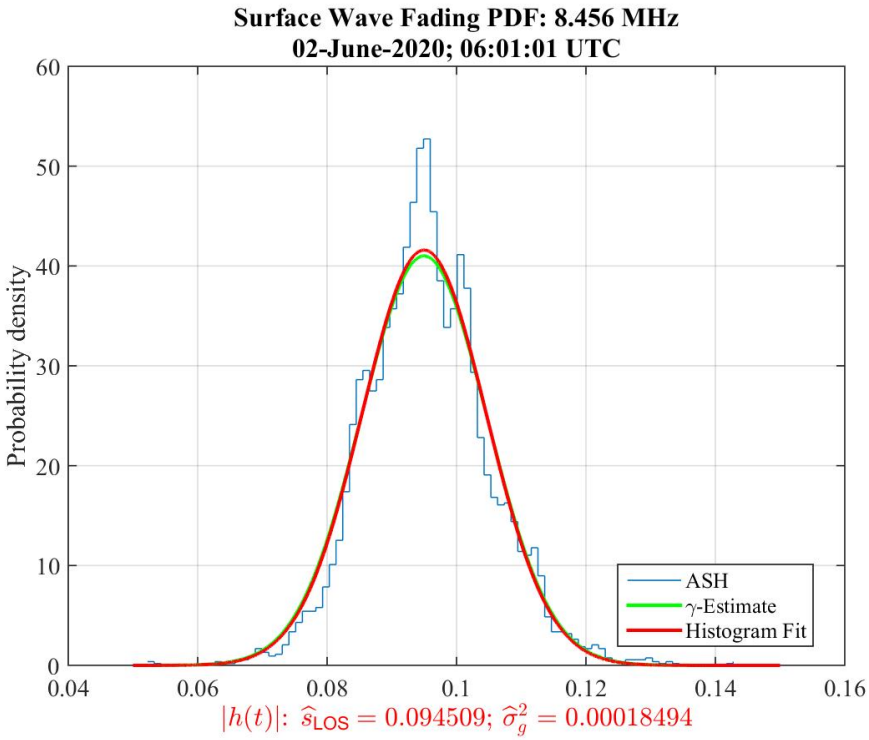


Figure 71: Histogram and Rician estimates; 02-June-2020 06:01:01 at 8.456 MHz; Rician estimates almost overlay.

Figure 72 plots the surface wave in the complex plane without the initial transient. A Rician model explains this plot. The specular component only rotates 300° because the Doppler shift is small (See Figure 69). The diffuse component shows high-frequency variations around the specular component caused by the almost flat noise floor (See Figure 70).

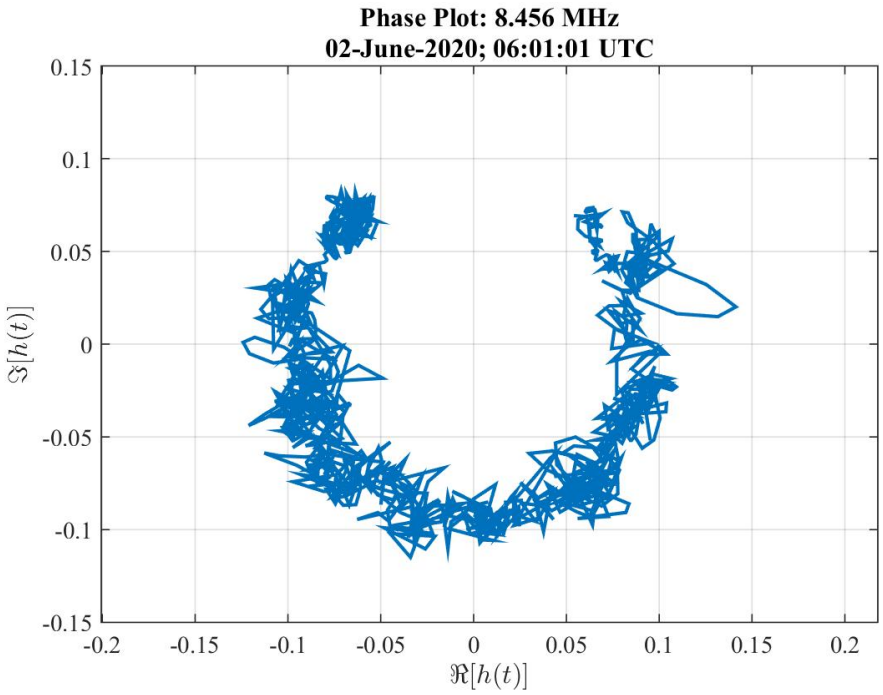


Figure 72: Fading phase on 02-June-2020 06:01 UTC at 8.456 MHz.

In summary, the amplitude and the phase plots show that this day's fading is well-modeled as Rician with a large K factor. The power spectrum of the diffuse component appears to be a low-frequency Gaussian shape in a flat noise floor. The flat noise biases the RMS bandwidth to the high side and the spectral modeling issues in Section 3 apply:

> *Should the flat noise be ignored or included as part of the diffuse component?*

This question is partly mitigated for HF simulations because the relatively large K factor makes the spectral shape of the small diffuse component of secondary importance.

4.2.3 12.45 MHz

This experiment is the basis for the "template" of Section 3.

4.2.4 18.474 MHz

Incomplete sounding as reported on Figure 60.

4.2.5 23.1 MHz

Figure 73 is the power-delay profile recorded at 23.1 MHz when the ship is approximately 60 km from the transmitter at 06:04:01 UTC. The profile shows a single spike at 0.24 ms delay consistent with the ground range to the transmitter and identifies the surface wave. The noise floor is almost 30 dB below this surface wave so that more Rician fading is revealed in comparison to the measurements at 4.23 and 8.456 MHz.

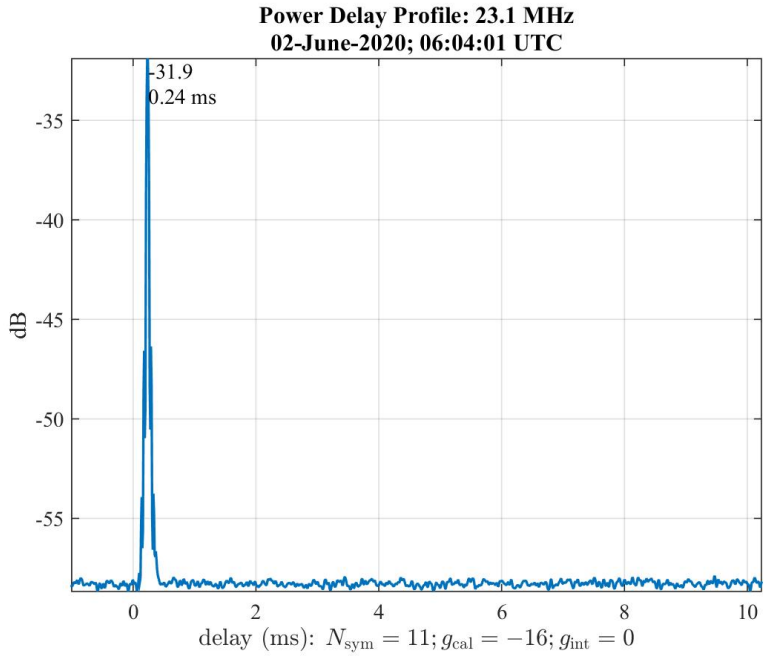


Figure 73: Power-delay profile on 02-June-2020 06:04 UTC at 23.10 MHz.

Figure 74 shows the surface-wave fading extracted at 0.24 ms delay. The amplitude shows a well-defined mean with variations having periods of between 2 and 3 seconds. The larger diffuse component, in comparison to the fading at 4.23 and 8.456 MHz, reduces the K factor ($\widehat{K} = 15.4$ dB). The phase is almost linear so the Doppler shift ($\widehat{f}_D = -0.0973$ Hz) is a credible model for linear phase and consistent with the ship steaming away from the transmitter.

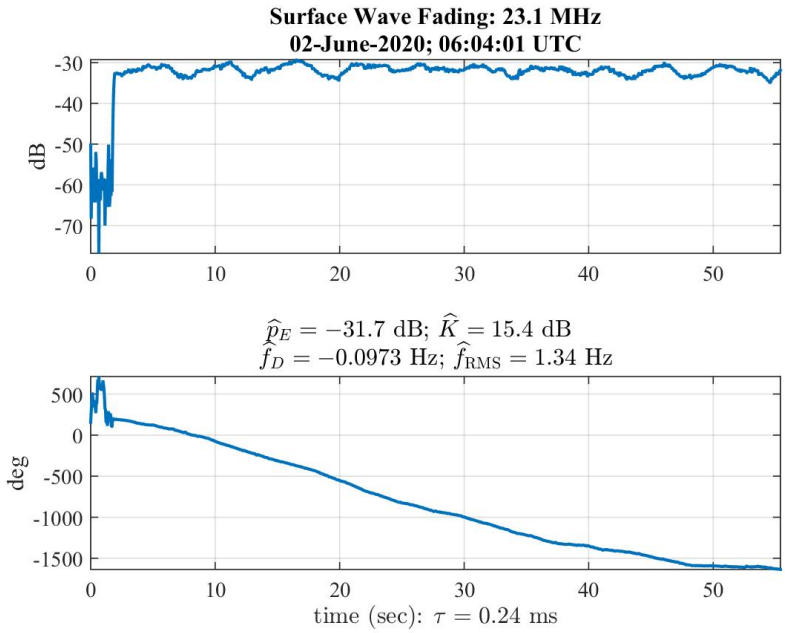


Figure 74: Fading on 02-June-2020 06:04 UTC at 23.1 MHz.

Figure 75 shows the surface-wave's fading spectrum consists of a spike sticking out of an almost flat spectral noise floor. The spike starts to widen 15 dB down and continues widening into the noise floor to almost 50 dB. This noise floor is almost 10 dB lower than the spectral noise floors at 4.23 and 8.456 MHz. The lower spectral noise floor and the increased energy of the diffuse component reveal more of the low frequency energy compared to the spectrum at 4.23 and 8.456 MHz. Consequently, the RMS bandwidth ($\widehat{f}_{\mathsf{RMS}} = 1.34$ Hz) is smaller than the preceding soundings but is still biased high by the noise floor.

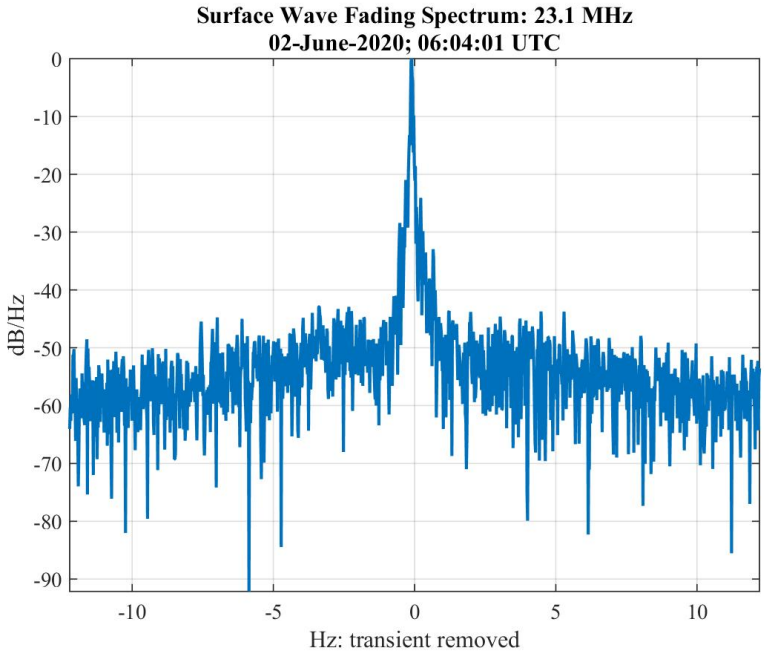


Figure 75: Fading spectrum on 02-June-2020 06:04 UTC at 23.1 MHz

Figure 76 compares the surface-wave's amplitude histogram to two Rician estimators described in Section 3. Although both estimators produced almost identical distrubtions, the histogram itself has multiple "lumps" that deviate from a Rician distribution. These lumps are explained by the phase plot.

Figure 77 plots the surface-wave fading in the complex plane. With $\widehat{K} = 15.4$ dB, the fading still shows a relatively tight "Rician" ring. The slow modulations of the diffuse component correspond to the distinct rotations in the phase. These distinct rotations cause the local "lumps" in the histogram. Future experiments could increase the sounding time or a physics-based modeling could specify parametric models for the surface-wave fading.

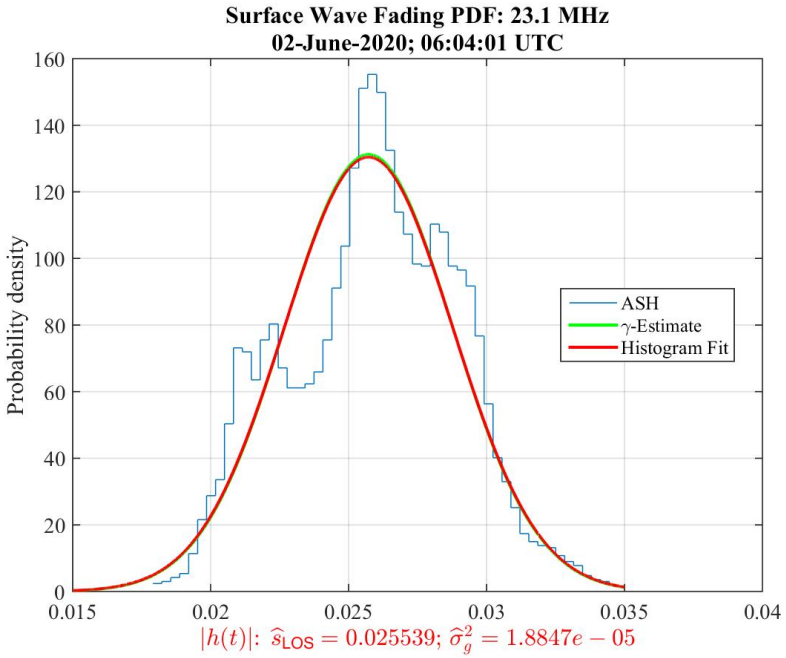


Figure 76: Histogram and Rician estimates; 02-June-2020 06:04 UTC at 23.1 MHz; Rician estimates almost overlay.

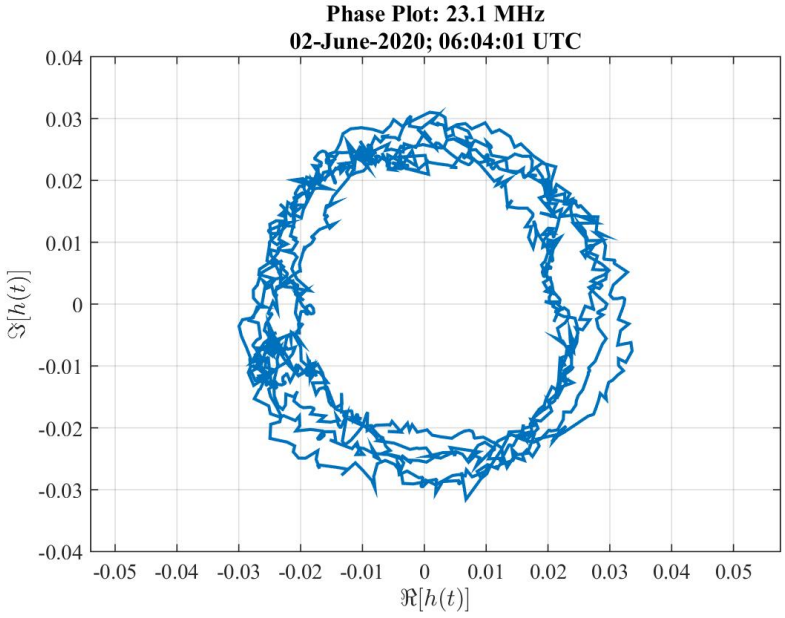


Figure 77: Fading phase at 23.1 MHz on 02-June-2020 06:04 UTC.

4.2.6 Discussion

This section tabulates the Rician fading parameters $\{K, f_D, f_{\mathsf{RMS}}\}$ extracted at 4.23, 8.456, 12.45, and 23.1 MHz on 02-June-2020 starting at 06:00 UTC—the soundings at 18.474 are incomplete.

K **Factor:** Each table show good agreement between the K factor estimates produced by moment, filtering, histogram methods. (See Section 3). The large K factors and well-defined Rician rings in the phase plots point to Rician fading:

Frequency (MHz)	4.23	8.456	12.45	23.1
$\widehat{K}$ (Hz)	20	17	19	15

Doppler Shift: Figure 61 shows the ship steaming away from the transmitter at 06:00 UTC. The increasing distance between transmitter and receiver forces positive velocities for the ship and negative Doppler shifts in the surface-wave channel. The ship's velocity measured with respect to the transmitter on 06:00:00 UTC is

$$v_{\mathsf{GPS}} = +1.8; \quad [\mathrm{m/s}].$$

The ship's velocities estimated from the Doppler shifts is $\widehat{v} = -\lambda \widehat{f}_D$, where λ is the wavelength, are not constant but increase toward the GPS velocity with increasing frequency:

Frequency (MHz)	4.23	8.456	12.45	23.1
$\widehat{v}$ (m/s)	-0.14	0.37	1.1	1.3

This bias in the Doppler shifts is present in all the experiments and will be quantified in Section 5.

RMS bandwidth: The spectral plots show that when more of the diffuse component is exposed, such as the lower spectral noise at 8.456 MHz, $\widehat{f}_{\mathsf{RMS}}$ tends to the lower frequencies. Otherwise, larger spectral noise pushes $\widehat{f}_{\mathsf{RMS}}$ to the high side for 4.23 and 12.45 MHz:

Frequency (MHz)	4.23	8.456	12.45
$\widehat{f}_{\mathsf{RMS}}$ (Hz)	3.2	1.45	3.1

This bias and spectral shape of the diffuse component is mitigated by the dominance of the specular component. These issues are reviewed in Section 5.

Table 7: Rician fading estimates on 02-June-2020 06:00:00 UTC; 4.23 MHz.

02-June-2020 06:00:00 UTC 4.23 MHz 69 km 0.24 ms			
K (dB)	f_D (Hz)	f_{RMS} (Hz)	Method
19.5472	0.0021	3.1505	Moments
20.7619	0.0086	3.7649	Filtering+Rayleigh Level Crossing
19.5003	0.0021	3.3623	Histogram+Rician Level Crossing

Table 8: Rician fading estimates on 02-June-2020 06:01:01 UTC; 8.456 MHz.

02-June-2020 06:01:01 UTC 8.456 MHz 69 km 0.24 ms			
K (dB)	f_D (Hz)	f_{RMS} (Hz)	Method
16.712	−0.0105	3.2660	Moments
17.794	−0.0137	2.9526	Filtering+Rayleigh Level Crossing
16.839	−0.0105	3.3788	Histogram+Rician Level Crossing

Table 9: Rician fading estimates on 02-June-2020 06:02:01 UTC; 12.45 MHz.

02-June-2020 06:02:01 UTC 12.45 MHz 69 km 0.24 ms			
K (dB)	f_D (Hz)	f_{RMS} (Hz)	Method
18.6438	−0.0465	1.1507	Moments
21.3153	−0.0475	3.3910	Filtering+Rayleigh Level Crossing
18.6618	−0.0465	1.1392	Histogram+Rician Level Crossing

Table 10: Rician fading estimates on 02-June-2020 06:04:01 UTC; 23.1 MHz.

02-June-2020 06:04:01 UTC 23.1 MHz 69 km 0.24 ms			
K (dB)	f_D (Hz)	f_{RMS} (Hz)	Method
15.448	−0.097259	1.3395	Moments
17.845	−0.096587	3.03	Filtering+Rayleigh Level Crossing
15.392	−0.097259	1.3466	Histogram+Rician Level Crossing

4.3 04-June-2020

Figure 78 shows the ship's circular track to the southwest of San Diego. The ship starts nearest to San Diego and winds around to the end point:

Start	00:00 UTC	358 km
End	23:59 UTC	424 km

This distance limits the surface-wave propagation. Figure 79 plots all the spectrograms and shows only interference—the channel sounding signal is not visible.

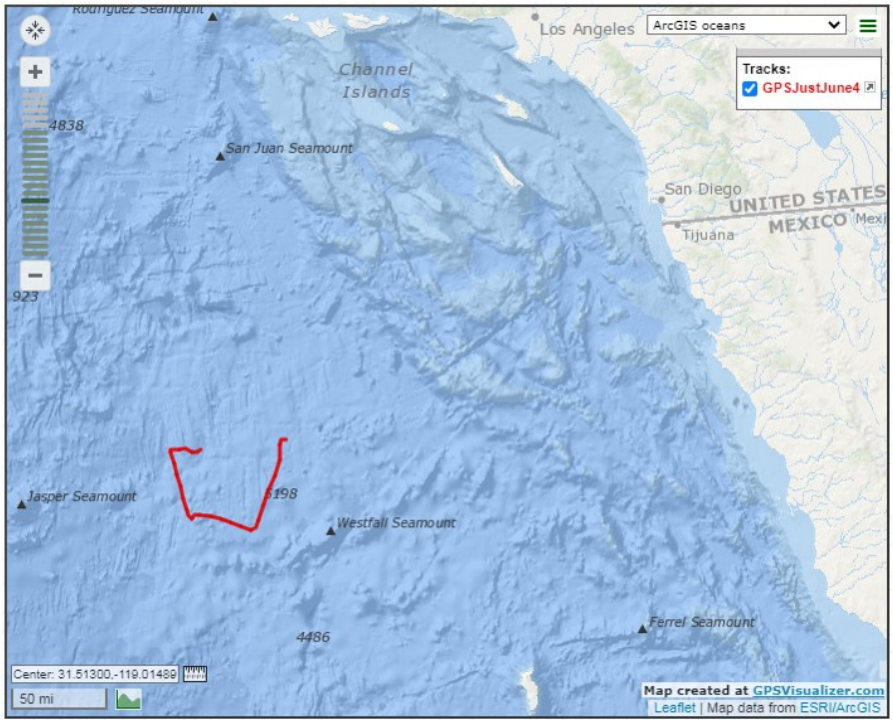


Figure 78: *Acoustic Explorer's* track on 04-June-2020.

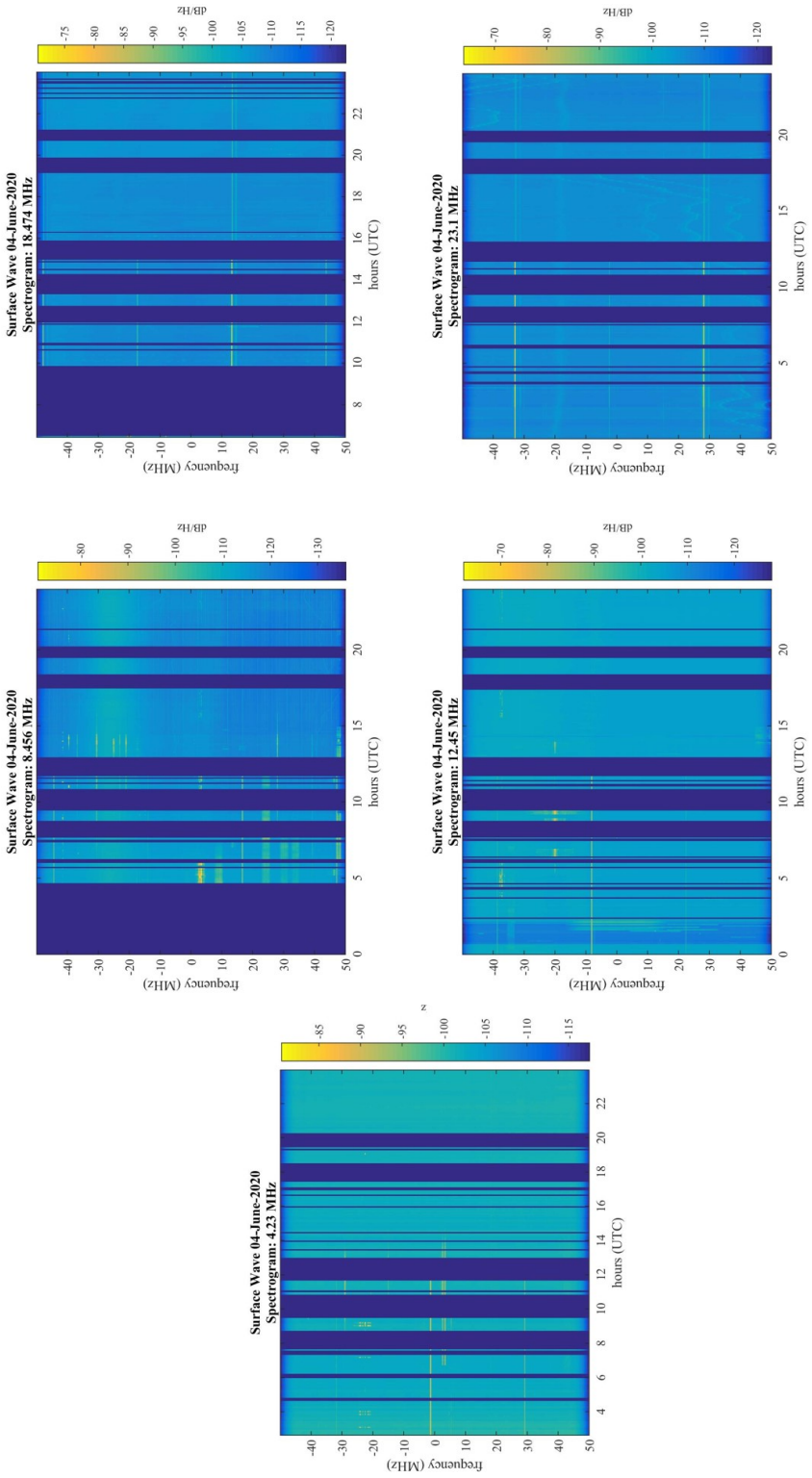


Figure 79: Spectrograms on 04-June-2020.

Figure 80 plots a sounding location that is 380 km from the transmitter in San Diego. Figure 81 shows the power-delay profile at the sounding location. The spike at 1.27 ms delay corresponds to the theoretical delay

$$1.27 \approx \left.\frac{d_G}{c_0}\right|_{d=379.9322} = 1.266 \quad [\text{ms}].$$

The two other taps correspond to skywaves.

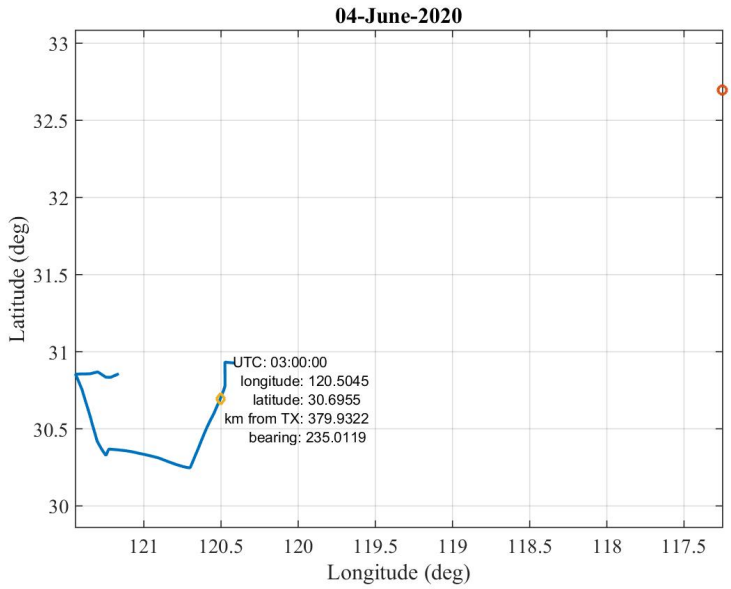


Figure 80: *Acoustic Explorer's* annotated track on 04-June-2020. Transmitter is the circle in the upper right.

Figure 82 shows the ionogram measured at Point Arguello, CA on 04-June-2020 at 03:00 UTC. The second tap at $\tau_2 = 1.47$ ms is likely the low O-Mode refracting from the layer at 210 km:

$$\tau_2 = 1.47 \approx \left.\frac{2d_2}{c_0}\right|_{d_2=210} = 1.4 \quad [\text{ms}].$$

The third tap at $\tau_3 = 3.42$ ms is likely the 2-Hop O-Mode refracting from the layer at 550 km:

$$\tau_3 = 3.42 \approx \left.\frac{2d_3}{c_0}\right|_{d_3=550} = 3.67 \quad [\text{ms}].$$

The value of this power-delay profile underscores an HF communications gap:

- the surface wave is at the limit of its propagation

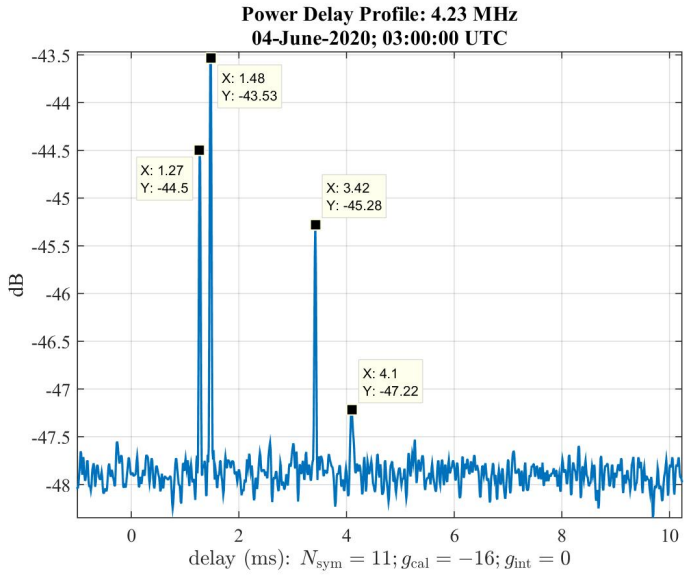


Figure 81: Power-delay profile on 04-June-2020 03:00 UTC at 4.23 MHz

- the HF skywaves are still in the upward null of the HF whip on the ship.

Only an HF-NVIS antenna that responds to the HF-NVIS skywaves covers this gap [14].

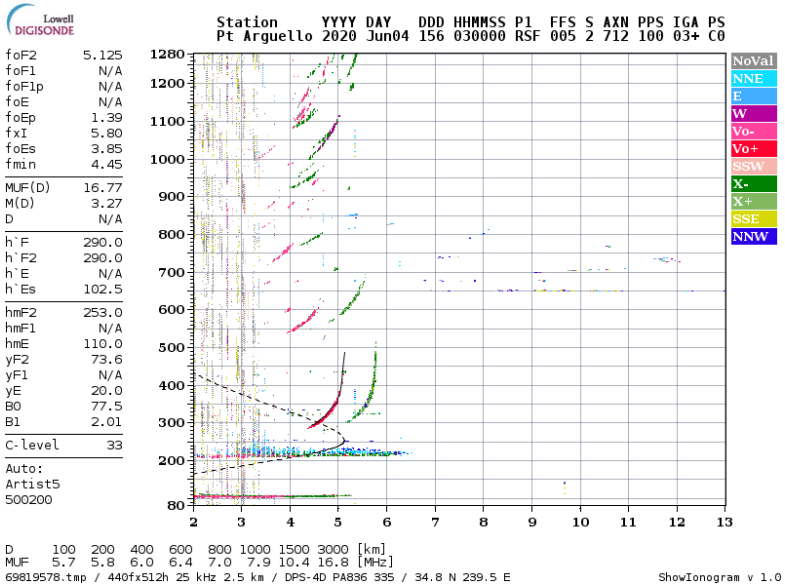


Figure 82: Ionogram at Point Arguello, CA; 04-June-2020 03:00 UTC.

4.4 05-June-2020

Figure 83 shows the ship's track off San Diego on 05-June-2020. The ship starts furthest from San Diego and steams toward San Diego:

Start	00:00 UTC	424 km
End	23:59 UTC	148 km

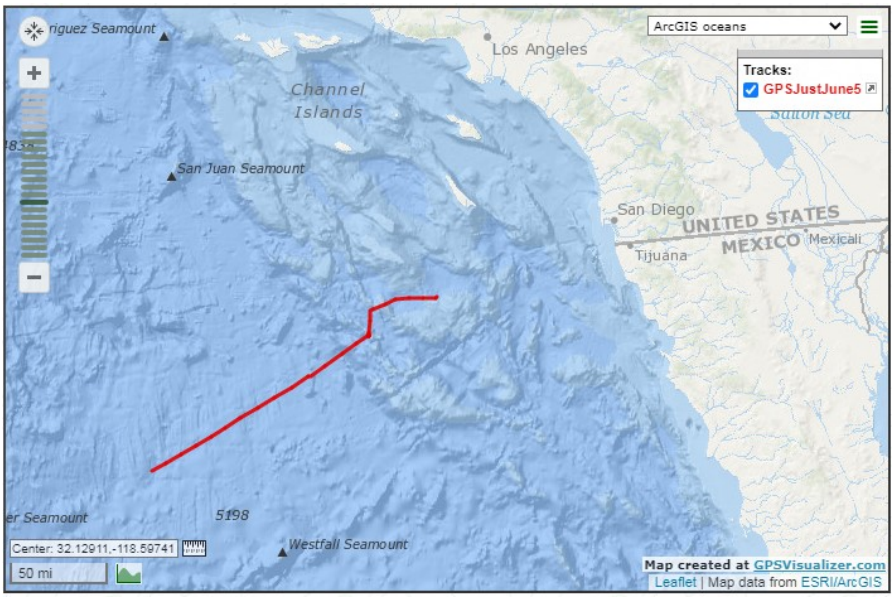


Figure 83: *Acoustic Explorer's* track on 05-June-2020.

None of the spectrograms register the sounding signal so these images are omitted. Only the three lowest frequencies registered a surface wave that was above the noise. Figure 84 shows these delay spreads at 4.23, 8.456, 12.45 MHz. Only when the ship gets close to San Diego does a single tap rise out of the noise starting around 21:00 UTC. The fading analysis will be confined to these frequencies at 21:35 UTC.

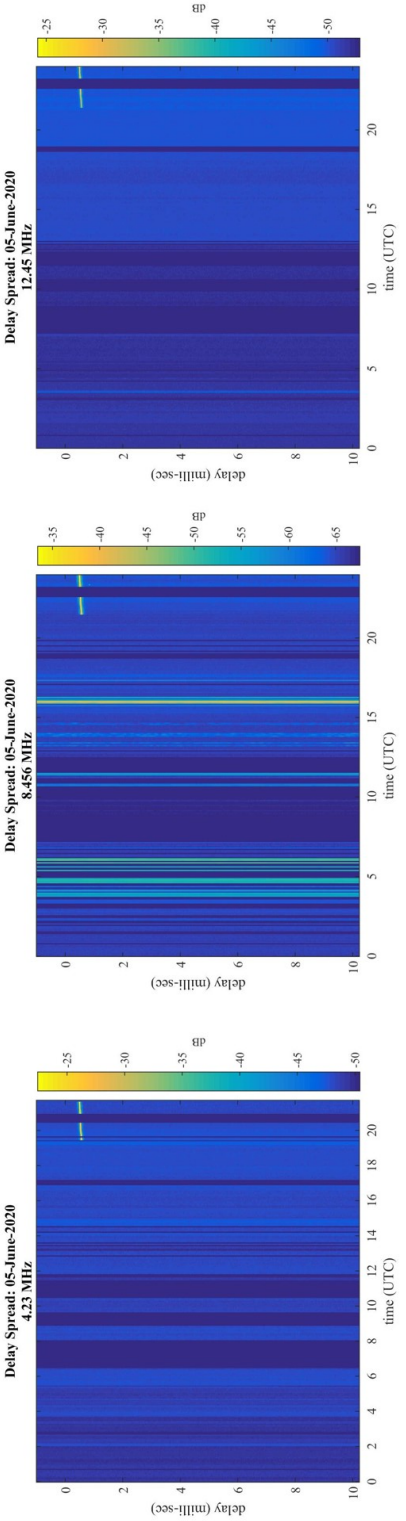


Figure 84: Delay spreads on 05-June-2020.

The fading analysis takes place at the same location. Figure 85 details the location of the fading analysis. At 21:35 UTC, the ship is 169.7 km southwest of San Diego and heading toward the transmitter. Figure 86 shows the power-delay profile of the surface wave at that time. There is a single spike rising out of the noise at 0.56 ms delay corresponding to the surface-wave's theoretical delay

$$0.56 \approx \left.\frac{d_G}{c_0}\right|_{d=169.7354} = 0.5658 \quad [\text{ms}].$$

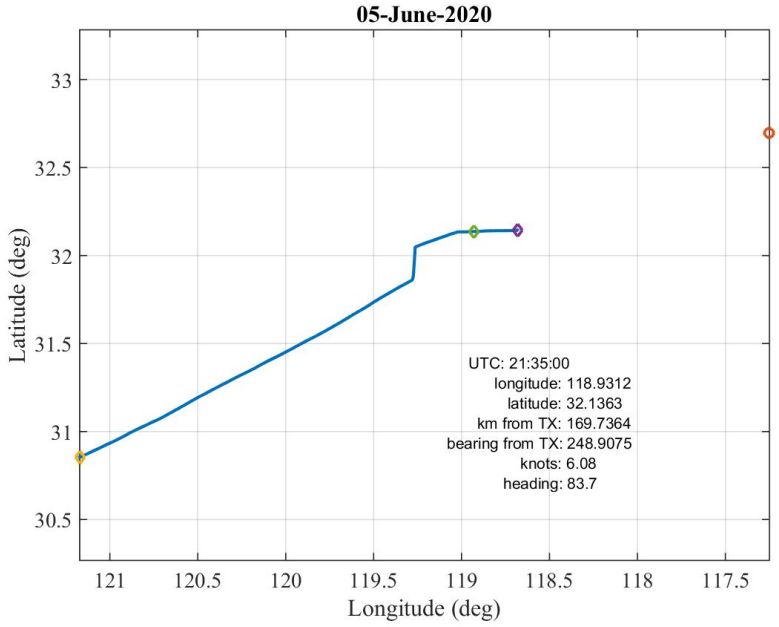


Figure 85: *Acoustic Explorer's* annotated track on 05-June-2020. Transmitter is the circle in the upper right.

The following sections report on the surface-wave fading at the HF sounding frequencies 4.23, 8.456, and 12.45 MHz. Each frequency reports a strong Rician K, good fits the Rician probability density function, and little spectral contamination. The most significant variation between the soundings is the noise floor. The noise at 8.456 MHz is almost 10 dB lower than at the other frequencies. Consequently, more of the Rician features are evident at 8.456 MHz. The soundings are tabulated for HF channel emulation in the final section.

4.4.1 4.23 MHz

Figure 86 shows the 4.23 MHz power-delay profile recorded when the ship is approximately 170 km from the transmitter at 21:35 UTC. The spike at 0.56 ms delay is consistent with the ground range to the transmitter and identifies the surface wave. The noise floor is almost 25 dB below this surface-wave's spike. The discussion will show this surface-wave fading is single-ray Rician with the noise floor obscuring the diffuse component and biasing the RMS bandwidth estimate.

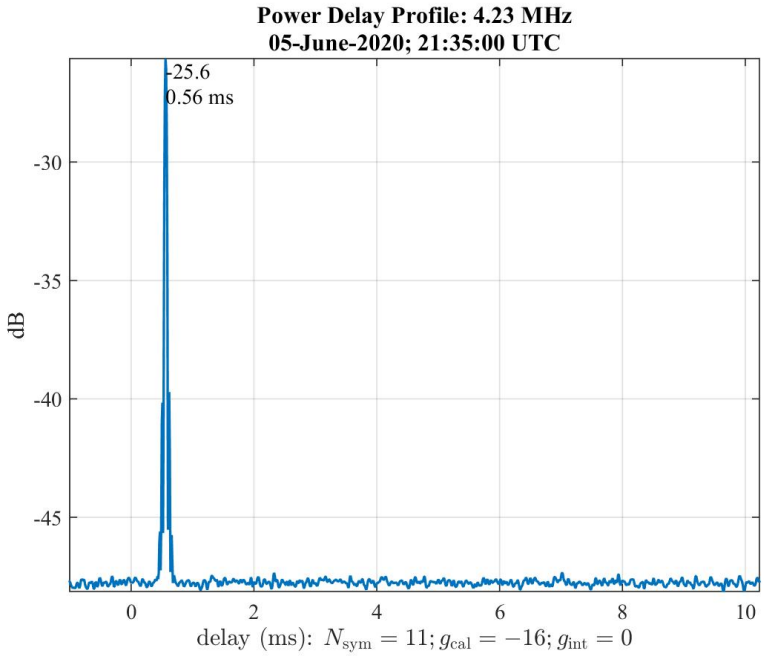


Figure 86: Power-delay profile on 05-June-2020 21:35 UTC at 4.23 MHz.

Figure 87 verifies these claims. The upper left panel shows the surface-wave's amplitude is nearly flat ($\widehat{K} = 21$ dB) with almost linear phase so the Doppler shift $\widehat{f}_D = 0.0634$ Hz makes sense. The lower left panel shows the surface-wave's power spectrum contains a single spike. Some of the spectral width of the spike—the bandwidth of the diffuse component—is visible under the noise. The noise biases $\widehat{f}_{\mathsf{RMS}} = 3.79$ Hz high whereas the diffuse components argue a bandwidth closer to 0.1 Hz. The upper right panel plots surface-wave in the complex plane showing the tight "Rician" ring caused by the large K factor. The high-frequency noise seen in the power spectrum generates the fast variations in the Rician ring. The lower right panel compares the surface-wave's amplitude histogram to the two Rician distributions estimated by moments and histogram fitting. The histogram is well modeled by the Rician distribution. To summarize, this surface-wave fading is well-modeled by Rician fading.

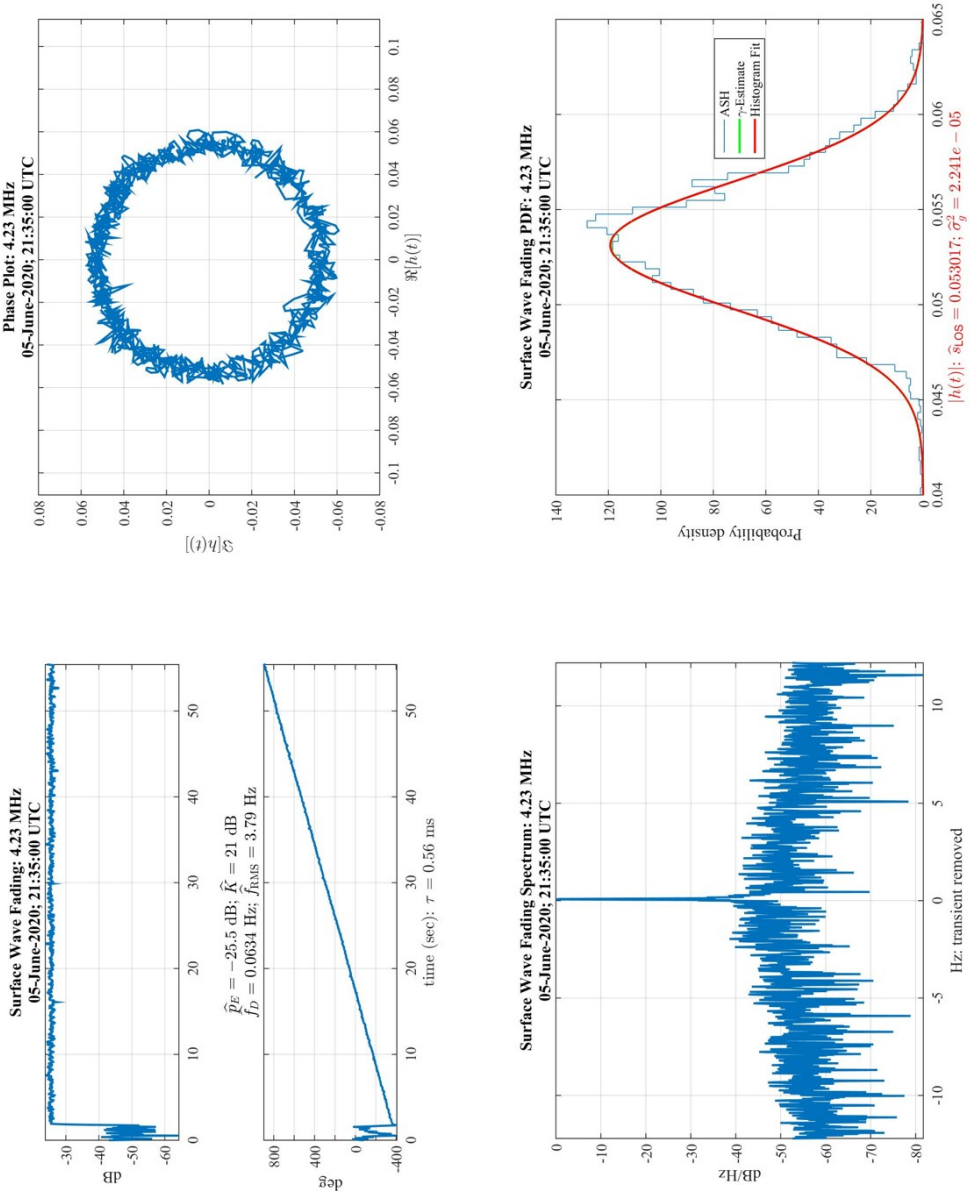


Figure 87: Fading summary on 05-June-2020 21:35 UTC at 4.23 MHz.

4.4.2 8.456 MHz

Figure 88 shows the power-delay profile at 8.456 MHz recorded when the ship is approximately 170 km from the transmitter at 21:36 UTC. The profile shows a single spike at 0.56 ms delay consistent with the ground range to the transmitter and identifies the surface wave. The noise floor is almost 30 dB below this surface wave. Consequently, more fading structure is revealed in comparison to the measurements at 4.23 MHz

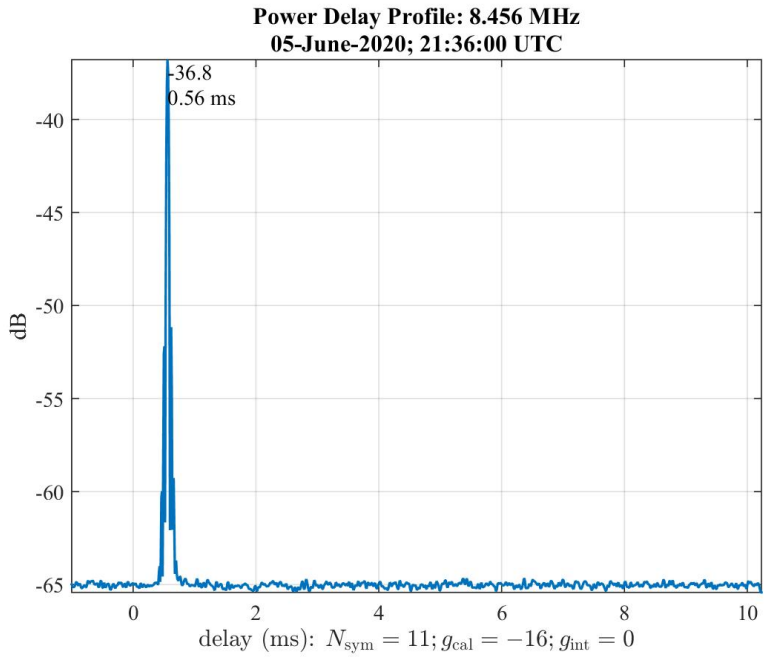


Figure 88: Power-delay profile on 05-June-2020 21:36 UTC at 8.456 MHz.

Figure 89 verifies this low-noise observation. The upper left panel shows the surface-wave's amplitude is nearly flat with less high-frequency noise than at 4.23 MHz. The lower left panel shows the surface-wave's power spectrum has noise floor almost 10 dB less in comparison to 4.23 MHz. Consequently, the diffuse component's spectral width is visible over the noise. The upper right panel plots the surface-wave in the complex plane showing less high-frequency variations to reveal the individual rotations. These individual rotations produce the "lumpiness" in the histograms in the lower right panel. Nevertheless, both the histogram and the Rician estimators produce almost identical Rician distributions.

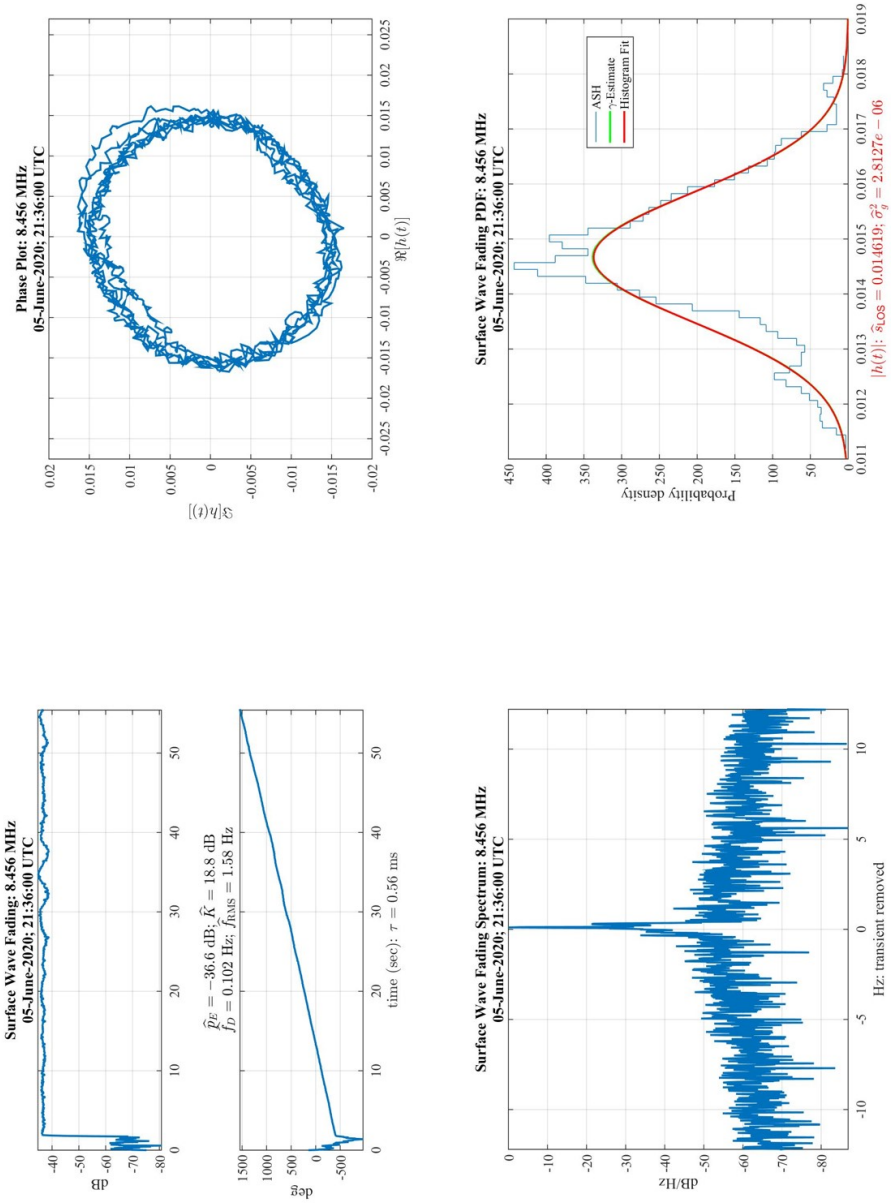


Figure 89: Fading summary on 05-June-2020 21:36 UTC on 8.456 MHz.

4.4.3 12.45 MHz

Figure 90 shows the power-delay profile recorded on the ship at 21:37 UTC when the ship was approximately 170 km from the San Diego transmitter at 12.45 MHz. The profile records a single spike at 0.56 ms delay consistent with the ground range to the transmitter and identifies the surface wave. However, the noise floor is only 18 dB below this surface wave. Consequently, there will be less detail of the Rician fading compared to the measurements at 8.456 MHz

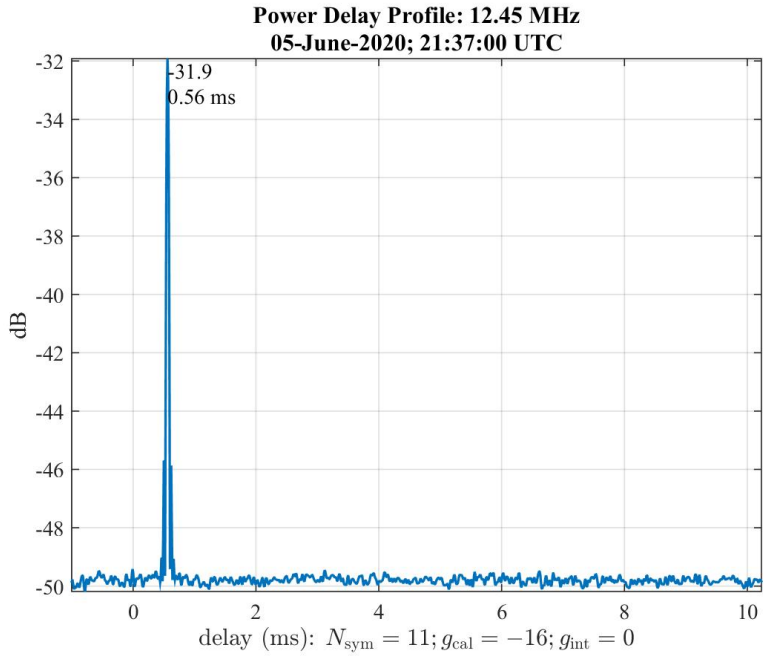


Figure 90: Power-delay profile on 05-June-2020 21:37 UTC at 12.45 MHz.

Figure 91 verifies these increased noise effects. The upper left panel shows the surface-wave's amplitude is nearly flat but has more high-frequency noise compared to the amplitude at 8.456 MHz. The lower left panel is the surface-wave's power spectrum showing a noise floor almost 10 dB greater than at 8.456 MHz. This noise buries the diffuse component and biases the RMS bandwidth estimate. The upper right panel plotting the surface-wave in the complex plane still shows the "Rician" ring with more high-frequency variations than at 8.456 MHz. The lower right panel compares the surface-wave's amplitude histogram to the Rician distributions estimated by moments and the histogram fitting. The increased noise smooths the histogram be almost Rician and causes both Rician estimates to produce almost identical distributions. In summary, Rician fading is a credible model for this surface-wave fading.

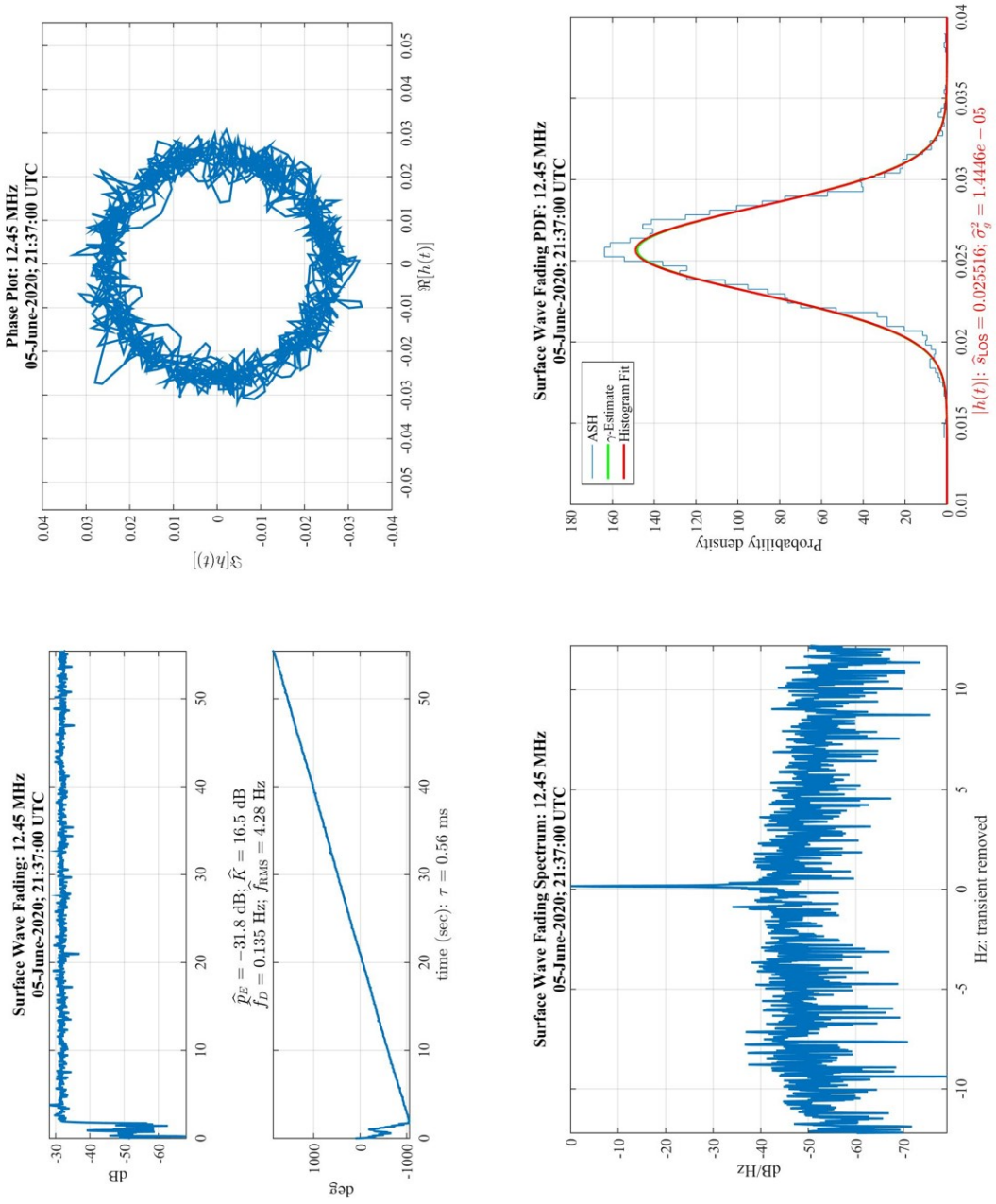


Figure 91: Fading summary on 05-June-2020 21:37 UTC at 12.45 MHz.

4.4.4 18.474 MHz

No surface wave at 21:37 UTC.

4.4.5 23.1 MHz

No surface wave at 21:38 UTC.

4.4.6 Discussion

This section tabulates the fading statistics at 4.23, 8.456, and 12.45 MHz—noise degraded the soundings at 18.474 and 23.1 MHz. Each table reports the Rician parameters $\{K, f_D, f_{\mathsf{RMS}}\}$ estimated using the three Rician estimators described in Section 4.1.6.

K Factor: The tables for 4.23, 8.456, and 12.45 MHz show the K factor estimates are close and below the upper bound. The tight "Rician" rings at 4.23 and 8.456 show less energy in the diffuse component than at 12.45 MHz to produce relatively large K factors:

Frequency (MHz)	4.23	8.456	12.45
$\widehat{K}$ (dB)	21	19	16

These large K factors describe a Rician fading process with a strong specular component and a weak diffuse component:

Doppler Shift: Figure 83 reports the ship is steaming toward the transmitter. The decreasing distance forces negative velocities for the ship and positive Doppler shifts in the surface-wave channels. All the tables report positive Doppler shifts. At 21:35 UTC, the ship's velocity with respect to the transmitter is reported in the GPS files as

$$v_{\mathsf{GPS}} = -3.02 \quad [\mathrm{m/s}].$$

When ship's velocity is estimated using the wavelength and Doppler shift ($\widehat{v} = -\lambda \widehat{f}_D$), the following tabulation shows $\widehat{v}$ is not constant but increases with increasing frequency.

Frequency (MHz)	4.23	8.456	12.45
$\widehat{v}$ (m/s)	-4.5	-3.6	-3.3

This same trend is observed in the subsequent experiments and will be quantified in Section 5.

RMS bandwidth: The RMS bandwidth estimates are biased toward high side whenever the spectral noise buries the diffuse component. Only the fading spectrum at 8.456 MHz shows some of the diffuse component above the noise and RMS moment estimates a smaller bandwidth compared to 4.23 and 12.45 MHz.

Frequency (MHz)	4.23	8.456	12.45
$\widehat{f}_{\mathsf{RMS}}$ (Hz)	3.8	1.6	4.3

The RMS estimator employs the entire sampling bandwidth—no prior information about the physical limits of the diffuse component is employed. Consequently, a flat spectral noise biases the RMS moment estimator as well as the Rayleigh and Rician level crossing estimators. If these "high" RMS estimates are used in simulations, this bias and the shape of the diffuse spectrum is somewhat mitigated by the dominance of the specular component. Both the bandwidth and simulation issues are discussed in Section 5.

Table 11: Rician fading estimates on 05-June-2020 21:35:00 UTC; 4.23 MHz.

05-June-2020 21:35:00 UTC 4.23 MHz 170 km 0.56 ms			
K (dB)	f_D (Hz)	f_{RMS} (Hz)	Method
20.9679	0.0634	3.7943	Moments
21.3645	0.0647	3.7778	Filtering+Rayleigh Level Crossing
20.9838	0.0634	4.4078	Histogram+Rician Level Crossing

Table 12: Rician fading estimates on 05-June-2020 21:36:00 UTC; 8.456 MHz.

05-June-2020 21:36:00 UTC 8.456 MHz 170 km 0.56 ms			
K (dB)	f_D (Hz)	f_{RMS} (Hz)	Method
18.847	0.10209	1.5778	Moments
21.239	0.10231	3.636	Filtering+Rayleigh Level Crossing
18.807	0.10209	1.9557	Histogram+Rician Level Crossing

Table 13: Rician fading estimates on 05-June-2020 21:37:00 UTC; 12.45 MHz.

05-June-2020 21:37:00 UTC 12.45 MHz 170 km 0.56 ms			
K (dB)	f_D (Hz)	f_{RMS} (Hz)	Method
16.483	0.13487	4.2754	Moments
16.922	0.15163	3.8165	Filtering+Rayleigh Level Crossing
16.539	0.13487	5.4619	Histogram+Rician Level Crossing

4.5 06-June-2020

Figure 92 maps the ship's track to the southwest of San Diego. The GPS files report the ship starts furthest from San Diego and ends at the closest point on the track:

Start	00:00 UTC	148 km
End	20:10 UTC	9 km

Although the shipboard receiver records to 18:00 UTC, the transmitter shut down at 06:00 UTC.



Figure 92: *Acoustic Explorer's* track on 06-June-2020.

Figures 93 and 94 compare the spectrograms and the delay spread functions at 4.23, 8.456, and 12.45 MHz. The soundings at 18.474 and 23.1 MHz are degraded by noise and omitted. The spectrograms in the top row show the channel sounding signal at the experiment's beginning that vanishes after 06:00 UTC. The delay spread functions in the bottom row show the surface wave at the experiment's beginning that vanishes after 06:00 UTC. The surface-wave is analyzed at 05:05 UTC when the ship is 135 km from the transmitter.

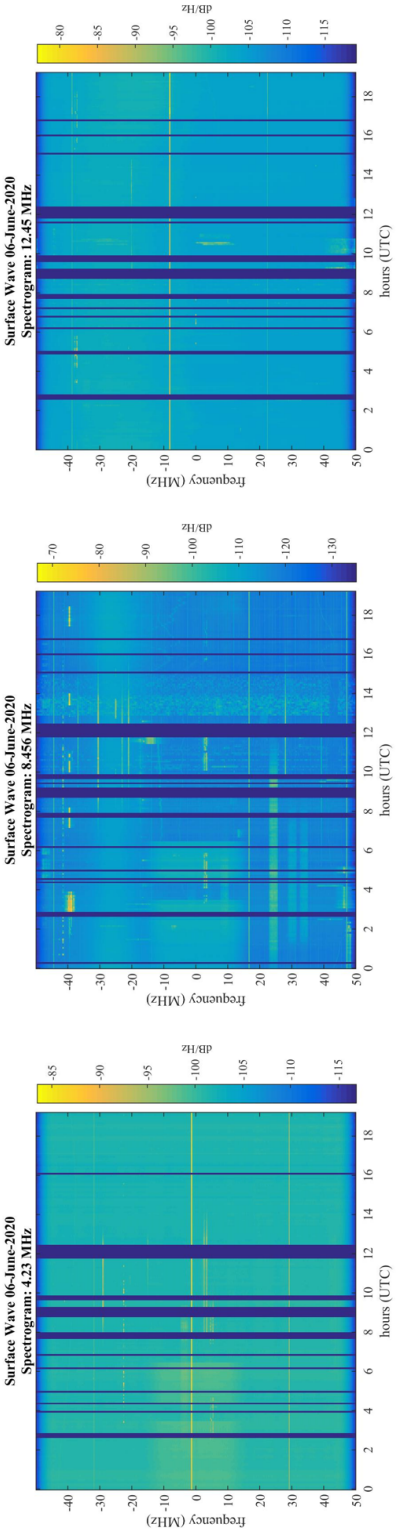


Figure 93: Spectrograms at 4.23, 8.456, and 12.45 MHz on 06-June-2020.

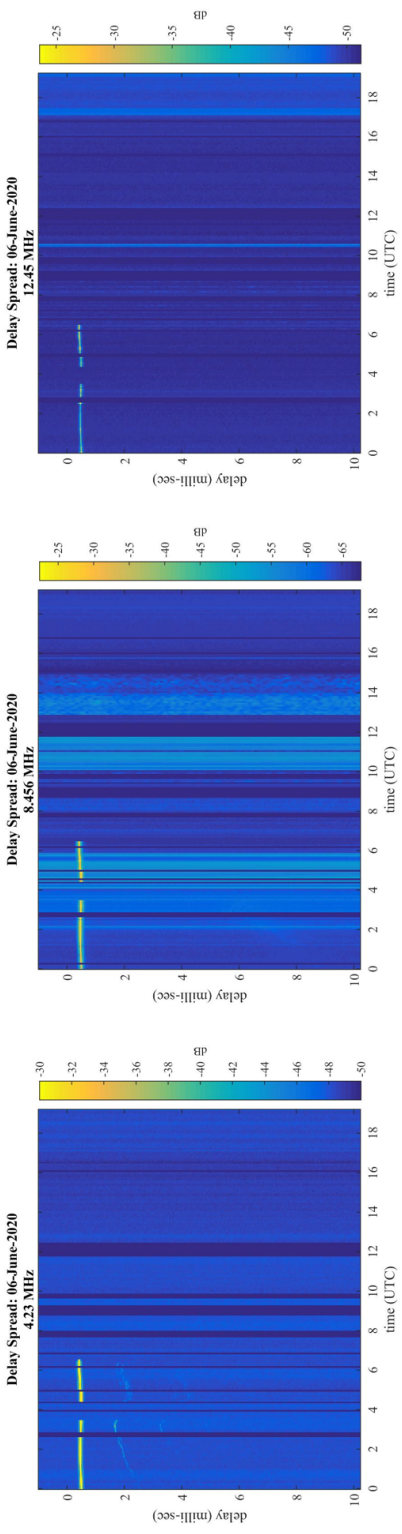


Figure 94: Delay spread functions at 4.23, 8.456, and 12.45 MHz on 06-June-2020.

Figure 95 shows the ship's track and the channel-sounding location at 05:05 UTC when the ship is 135 km southwest of San Diego and heading toward the transmitter. Figure 96 shows the power-delay profile at that time. The largest spike 0.49 ms delay corresponding to the surface-wave's delay measured by the ground range to the transmitter:

$$0.49 \approx \left.\frac{d_G}{c_0}\right|_{d=134.6513} = 0.4488 \quad [\text{ms}].$$

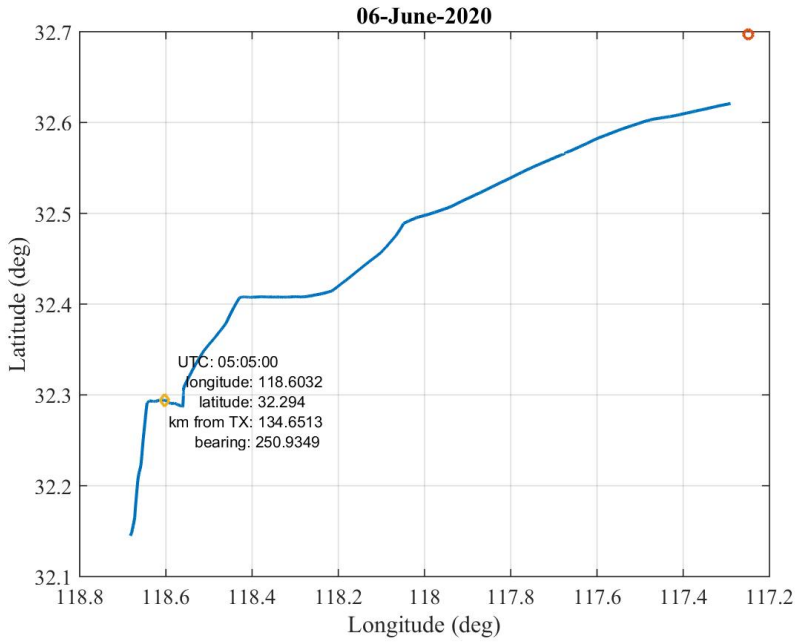


Figure 95: *Acoustic Explorer's* annotated track on 06-June-2020. Transmitter is the circle in the upper right.

The following sections report on the fading measured at this 135-km range over the HF sounding frequencies 4.23, 8.456, and 12.45 MHz. Each frequency reports a strong K factor (11 to 25 dB), Doppler estimates consistent with estimates of the ship's velocity, good fits the Rician probability density function, and little spectral contamination by harmonics. The noise is the most significant difference between soundings. The noise floors at 4.23 and 8.456 MHz are approximately 30 dB down from the surface-wave's spike but only 14 dB down at 12.45 MHz. Consequently, more Rician features are evident at 4.23 and 8.456 MHz than at 12.45 MHz. The soundings are tabulated for HF channel emulation in the final section.

4.5.1 4.23 MHz

Figure 96 plots the power-delay profile at 4.23 MHz measured when the ship is approximately 135 km from the transmitter at 05:05 UTC. The spike at 0.49 ms delay is consistent with the ground range to the transmitter and identifies the surface wave. The plot shows a noise floor almost 30 dB below the surface-wave's spike. The discussion will show Rician fading is a credible approximation for this surface-wave fading, despite the noise floor obscuring the diffuse component and biasing the RMS bandwidth estimate.

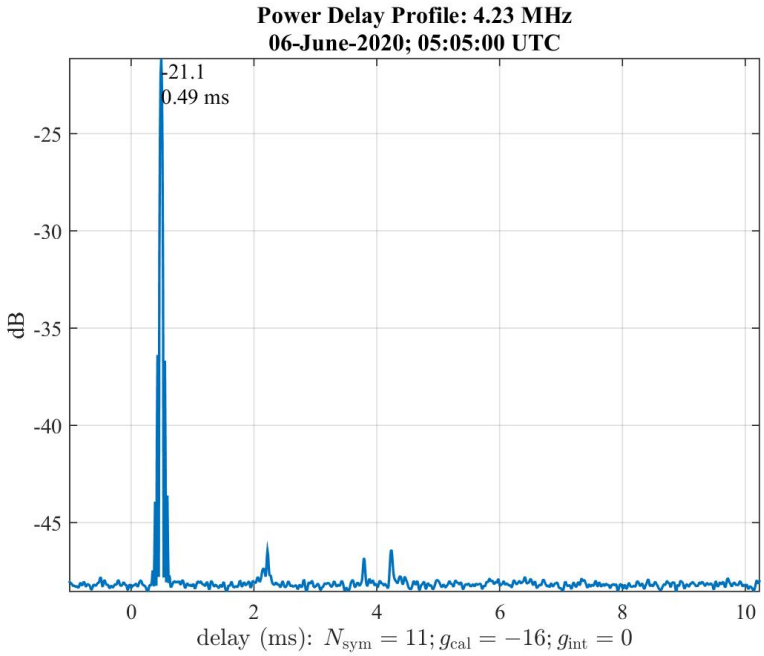


Figure 96: Power-delay profile on 06-June-2020 05:05:00 UTC at 4.23 MHz.

Figure 97 report on the Rician attributes of this this fading. The upper left panel shows the surface-wave's amplitude is nearly flat ($\widehat{K} = 25$ dB). The phase is almost linear with small 10-second modulations so that the Doppler shift $\widehat{f}_D = 0.0227$ Hz makes sense. The lower left panel shows the surface-wave's power spectrum consists of a "spike" in almost flat noise. This noise biases $\widehat{f}_{\mathsf{RMS}} = 3.24$ Hz to the high side whereas the diffuse component argues for a 0.1 Hz bandwidth. The upper right panel plots the surface wave in the complex plane showing the "Rician" ring caused by the large K factor. The lower right panel compares the surface-wave's amplitude histogram to the Rician distributions estimated by moments and the histogram fitting. These two Rician distributions are almost identical and show the histogram is well-modeled by a Rician distribution. In summary, a Rician fading is a credible model for this surface-wave fading.

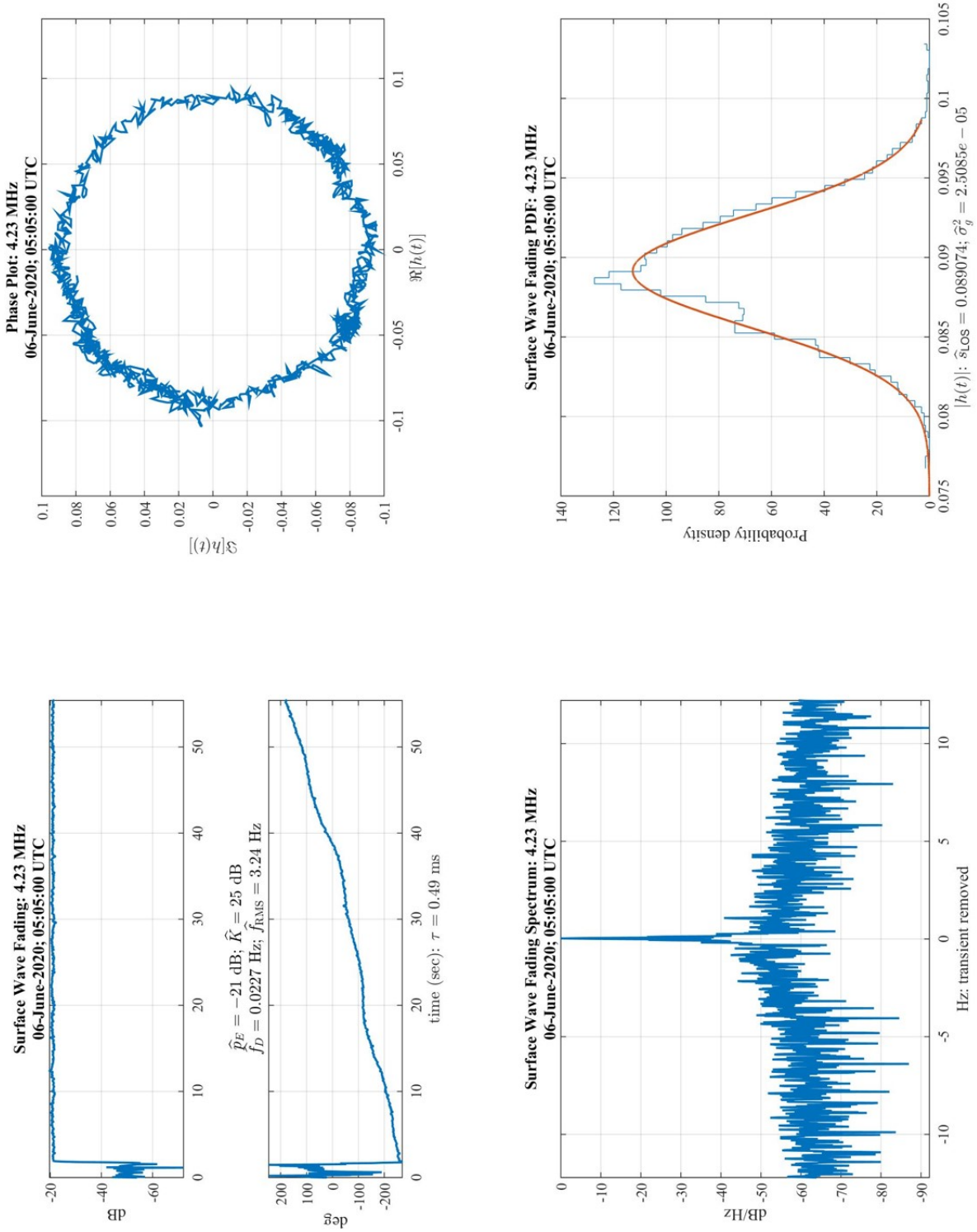


Figure 97: Fading summary on 06-June-2020 05:05 UTC at 4.23 MHz.

4.5.2 8.456 MHz

Figure 98 shows the power-delay profile at 8.456 MHz measured on the ship at 05:06 UTC. The spike at 0.49 ms delay is consistent with the 135 km ground range to the transmitter and identifies the surface wave. There is less noise and a stronger diffuse component than at 4.23 MHz. Consequently, more low-frequency spectral energy in the diffuse component is revealed.

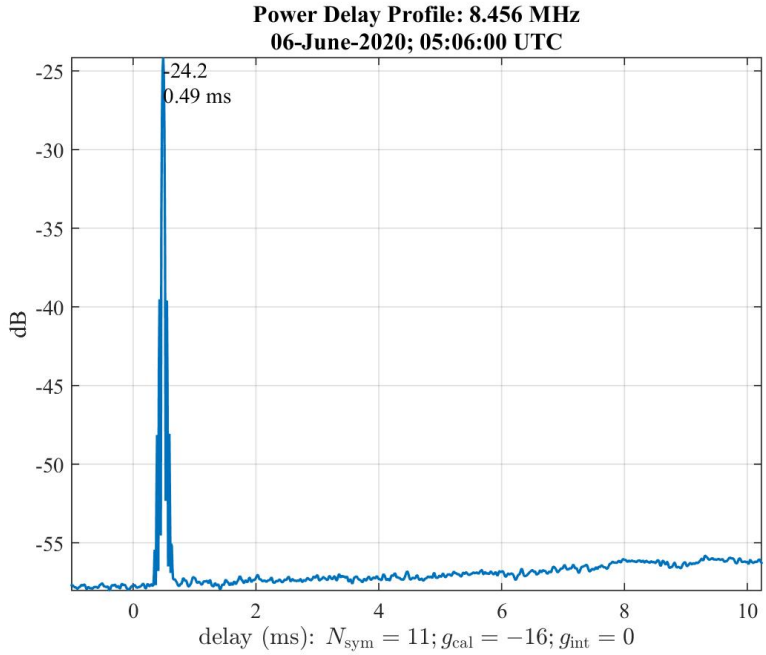


Figure 98: Power-delay profile on 06-June-2020 05:06 UTC at 8.456 MHz.

Figure 99 shows Rician attributes of this fading. The upper left panel shows the surface-wave's amplitude is almost flat ($\widehat{K} = 23.1$ dB) with a small modulations of 3 seconds. The surface-wave's phase is almost linear so the Doppler shift $\widehat{f}_D = 0.0152$ Hz makes sense. The lower left panel shows the surface-wave's power spectrum. There is a narrow spike 50 dB above the noise with spectral width corresponding to the 3-second modulations. The noise biases $\widehat{f}_{\mathsf{RMS}} = 1.46$ Hz to the high side while the modulations suggest that 0.3 Hz is a less biased RMS estimate. The upper right panel plots the surface wave in the complex plane. The large K factor produces a partial "Rician" ring showing noisy bursts. The lower right panel plot the surface-wave's amplitude histogram. This histogram is well-modeled by the two Rician distributions estimated by moments and histogram fitting. In summary, the large K factor makes Rician fading a credible model for this surface-wave fading.

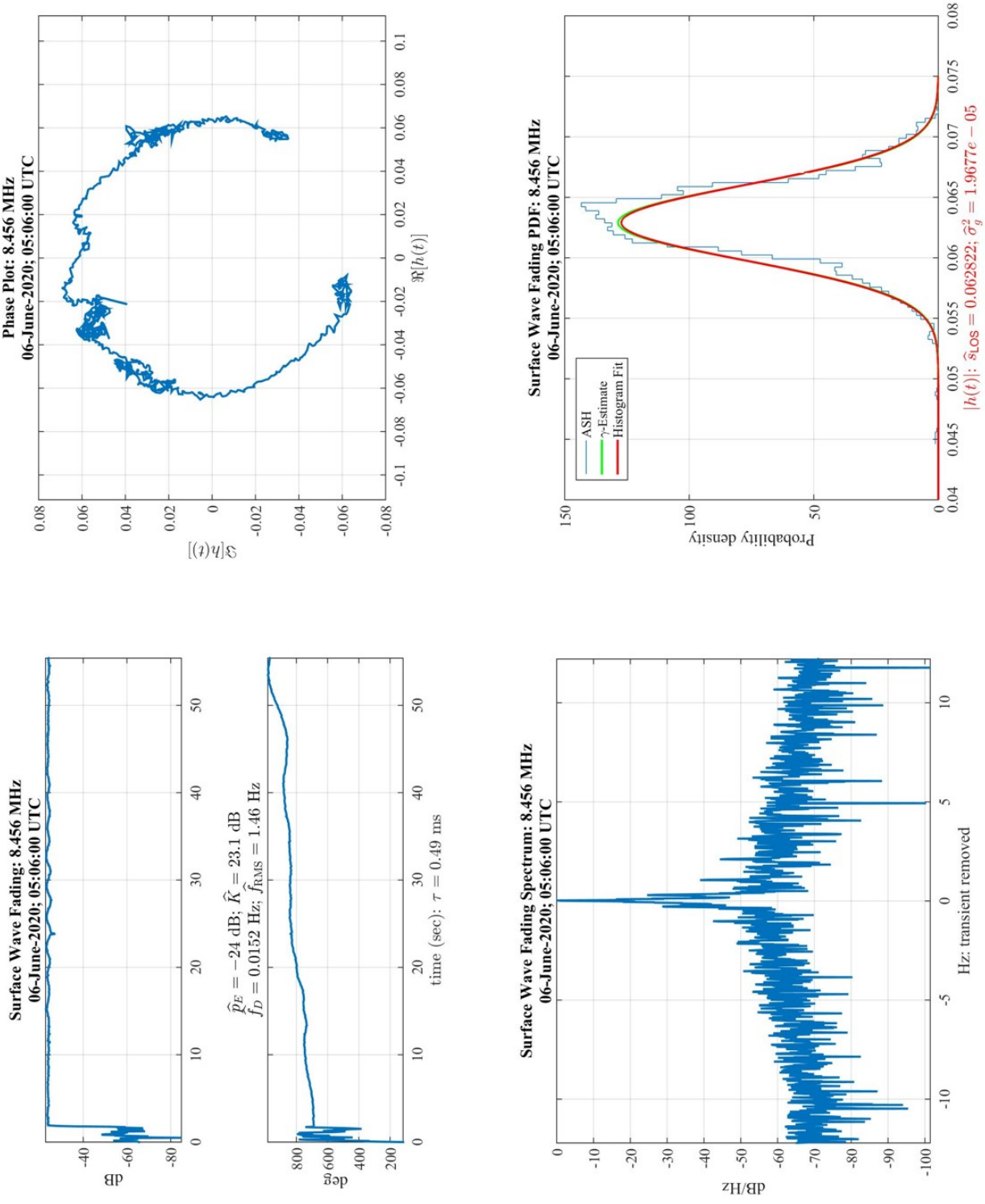


Figure 99: Fading summary on 06-June-2020 05:06 UTC at 8.456 MHz.

4.5.3 12.45 MHz

Figure 100 plots the power-delay profile at 12.45 MHz measured on the ship at 05:07 UTC. The plot shows a spike 0.49 ms at delay. This delay is consistent with the 135 km ground range to transmitter and identifies the surface wave.

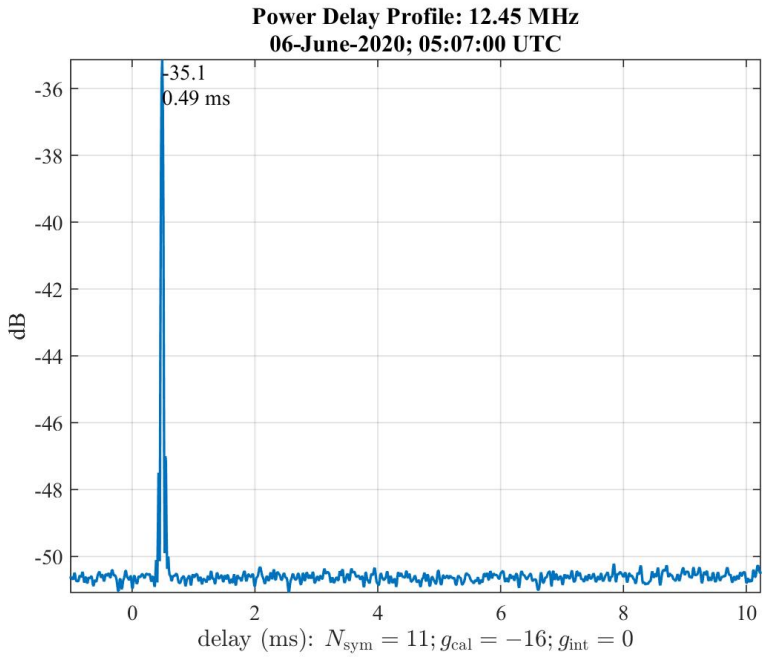


Figure 100: Power-delay profile on 06-June-2020 05:05:07 UTC at 12.45 MHz.

Figure 101 reports the surface-wave fading at 12.45 MHz admits a Rician approximation. The upper left panel shows the surface-wave's amplitude has a well-defined mean ($\widehat{K} = 11.2$ dB), modulations of 2 and 3 seconds, and high-frequency noise. The surface-wave's phase is almost linear so the Doppler shift $\widehat{f}_D = 0.0179$ Hz makes sense. The lower left panel shows the surface-wave's power spectrum contains a low-frequency spike that widens 16 dB down drops into the noise 30 dB down. This spectral noise biases $\widehat{f}_{\mathsf{RMS}} = 3.11$ Hz to the high side whereas the diffuse component argues this bandwidth is closer to 0.2 Hz. The upper right panel plots the surface wave in the complex plane and shows large "bursts" obscuring the "Rician" ring. This measurement is unique among all the soundings. The lower right panel compares the surface-wave's amplitude histogram to the Rician distributions estimated by moment and histogram fitting. The two distributions are almost identical and are good fits the histogram. Although Rician fading describes most of this surface-wave fading, the phase bursts point to more general fading classes listed in Section 5.

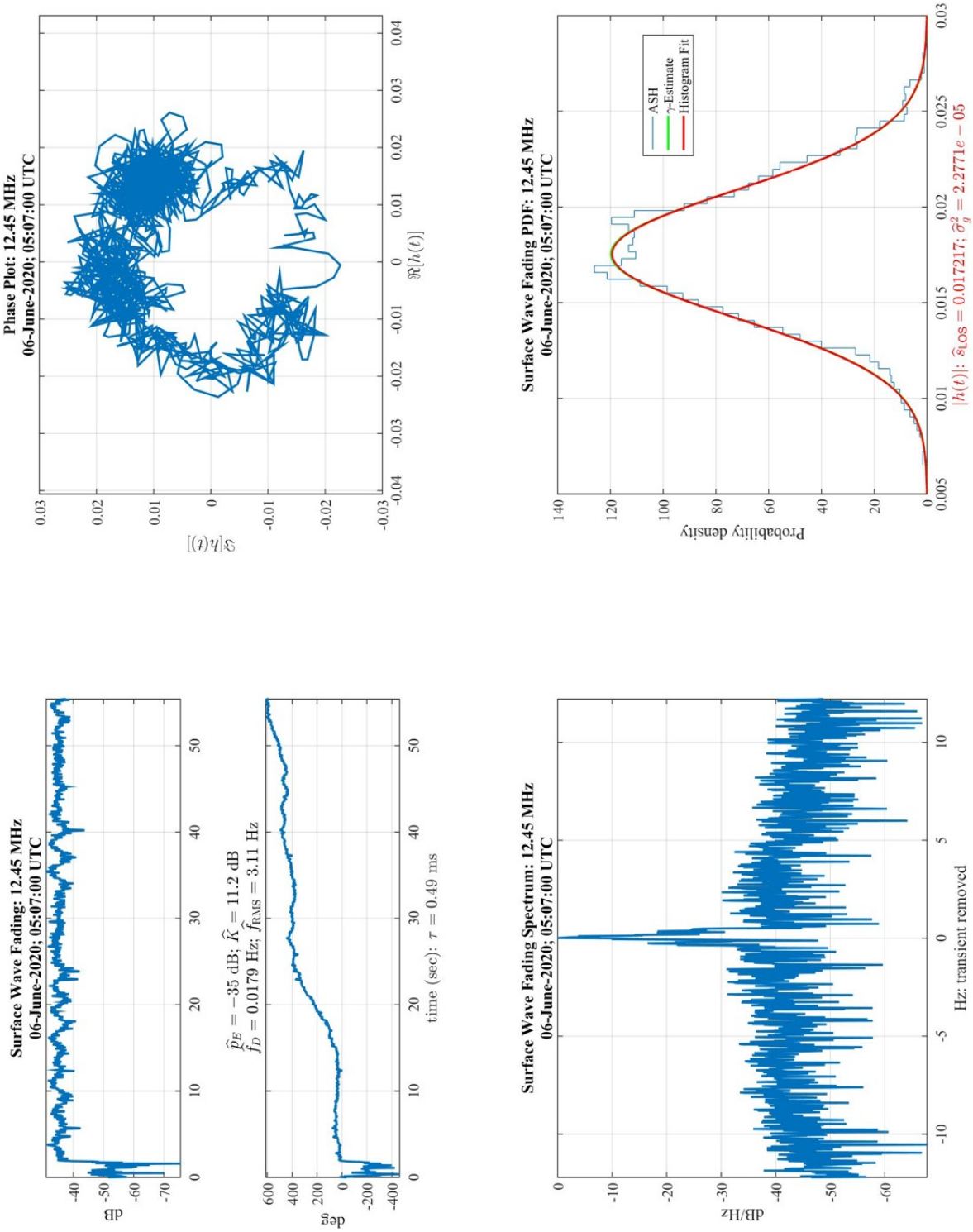


Figure 101: Fading summary on 06-June-2020 05:07 UTC at 12.45 MHz.

4.5.4 18.474 MHz

No surface-wave channel at 05:08 UTC.

4.5.5 23.1 MHz

No surface-wave channel at 05:09 UTC.

4.5.6 Discussion

Only 4.23, 8.456, and 12.45 MHz registered a channel—noise degraded the soundings at 18.474 and 23.1 MHz.

K **Factor:** The tables for 4.23, 8.456, and 12.45 MHz show agreement of the K factor estimates and the upper bound. The phase plots show tight Rician "rings" at 4.23 and 8.456 MHz that are visual confirmations of large K factors. The phase plot at 12.45 MHz exhibits large bursts that reduce the K factor because of the increased energy in the diffuse component:

Frequency (MHz)	4.23	8.456	12.45
$\widehat{K}$ (Hz)	25	23	11

Doppler Shift: Figure 95 shows the ship steaming toward the transmitter at 0.45 knots. The decreasing distance forces a negative velocity for the ship and positive Doppler shifts in the surface-wave channels. The tables report positive Doppler shifts The GPS files report the ship's velocity measured with respect to the transmitter at 05:05:00 UTC to be

$$v_{\mathsf{GPS}} = -0.1 \quad [\text{m/s}].$$

The ship's velocity $\widehat{v} = -\lambda \widehat{f}_D$ estimated from the Doppler shifts is not constant but increases with increasing frequency.

Frequency (MHz)	4.23	8.456	12.45
$\widehat{v}$ (m/s)	-1.6	-0.53	-0.43

This effect is still under consideration.

RMS Bandwidth: The spectral plots show that when more of the diffuse component is exposed, such as the lower spectral noise at 8.456 MHz, $\widehat{f}_{\mathsf{RMS}}$ tends to the lower frequencies. Otherwise, the flat spectrum noise biases $\widehat{f}_{\mathsf{RMS}}$ on the high side for 4.23 and 12.45 MHz:

Frequency (MHz)	4.23	8.456	12.45
$\widehat{f}_{\mathsf{RMS}}$ (Hz)	3.2	1.45	3.1

The lower noise floors better show the low-frequency energy in the diffuse component. If these Rician parameters are used in simulations, this bias and the shape of the diffuse spectrum is mitigated by the dominance of the specular component. These issues are reviewed in Section 5.

Table 14: Rician fading estimates on 06-June-2020 05:05:00 UTC; 4.23 MHz.

06-June-2020 05:05 UTC 4.23 MHz 135 km 0.49 ms			
K (dB)	f_D (Hz)	f_{RMS} (Hz)	Method
25.001	0.022661	3.243	Moments
25.63	0.023052	3.5457	Filtering+Rayleigh Level Crossing
24.809	0.022661	3.365	Histogram+Rician Level Crossing

Table 15: Rician fading estimates on 06-June-2020 05:06:00 UTC; 8.456 MHz.

06-June-2020 05:06:00 UTC 8.456 MHz 135 km 0.49 ms			
K (dB)	f_D (Hz)	f_{RMS} (Hz)	Method
23.114	0.015173	1.4618	Moments
25.253	0.014883	2.9139	Filtering+Rayleigh Level Crossing
23.023	0.015173	1.4453	Histogram+Rician Level Crossing

Table 16: Rician fading estimates on 06-June-2020 05:07:00 UTC; 12.45 MHz.

06-June-2020 05:07:00 UTC 12.45 MHz 135 km 0.49 ms			
K (dB)	f_D (Hz)	f_{RMS} (Hz)	Method
11.183	0.017898	3.1083	Moments
12.575	0.026185	3.7133	Filtering+Rayleigh Level Crossing
11.146	0.017898	3.2215	Histogram+Rician Level Crossing

5 Conclusions

The soundings show these wideband HF surface-wave channels are well modeled with a delay spread function $\{h_{\mathsf{SW}}(t,\tau)\}$ that is a single-tap Rician:

$$h_{\mathsf{SW}}(t,\tau) = h(t)\delta(\tau - \tau_G); \quad \tau_G = \frac{d_G}{c_0}, \tag{15}$$

where d_G is the ground range between the transmitter and receiver, c_0 is the velocity of light, and the fading process $\{h(t)\}$ is *Rician*:

$$h(t) = e^{j2\pi f_D t}\{s_{\mathsf{LOS}} + g(t)\} \tag{16}$$

consisting of a linear *Doppler shift* f_D modulating a strong *specular component* s_{LOS}, a weaker *diffuse component* $\{g(t)\}$ that is zero-mean Gaussian with variance σ_g^2 and RMS bandwidth f_{RMS}. All the measurements are tabulated to use in NIWC's HF Channel Emulator. This analysis fulfills the first two objectives listed in Section 3 and repeated here for convenience:

SW-1 Surface wave channel identification

SW-2 Tabulation of the surface-wave channels

SW-3 Documenting the gaps between theory and measurements

The gaps between theory and measurements starts with the Rician model itself. The surface-wave measurements exhibit tight "Rician rings" in the phase plots, a strong K-factor ($K \approx 18$ dB), and fading spectrum with a narrowband "spike" corresponding to the specular component that widens out to show the diffuse component roughly K dB down. A close-up of the diffuse component shows a Gaussian shape in the low frequencies. What is missing from this "taxidermist" approach is a *physics-based* argument showing the surface-wave fading *should* be Rician. For HF propagation in the ionosphere, a physics-based argument for Rician fading was advanced by Shaft [60], modified by Valley [71], and assessed by De Raad & Grover [25]. A physics-based argument for surface-wave fading would encompass the action of the sea surface on the propagating HF wave. A complete theory would map the direction of the HF wave over the sea-surface into the Rician parameters (e.g., HF propagation parallel to the wave troughs produces less Doppler shift than propagation orthogonal to the wave troughs).

The second gap between theory and measurements is that with ship's velocities $\widehat{v} = -\lambda\widehat{f}_D$ estimated from the Doppler shifts $\widehat{f}_D$ are not constant but increase with increasing frequency as shown in Figure 102. The trend appears to converge to the ship's velocity estimated from the GPS files.

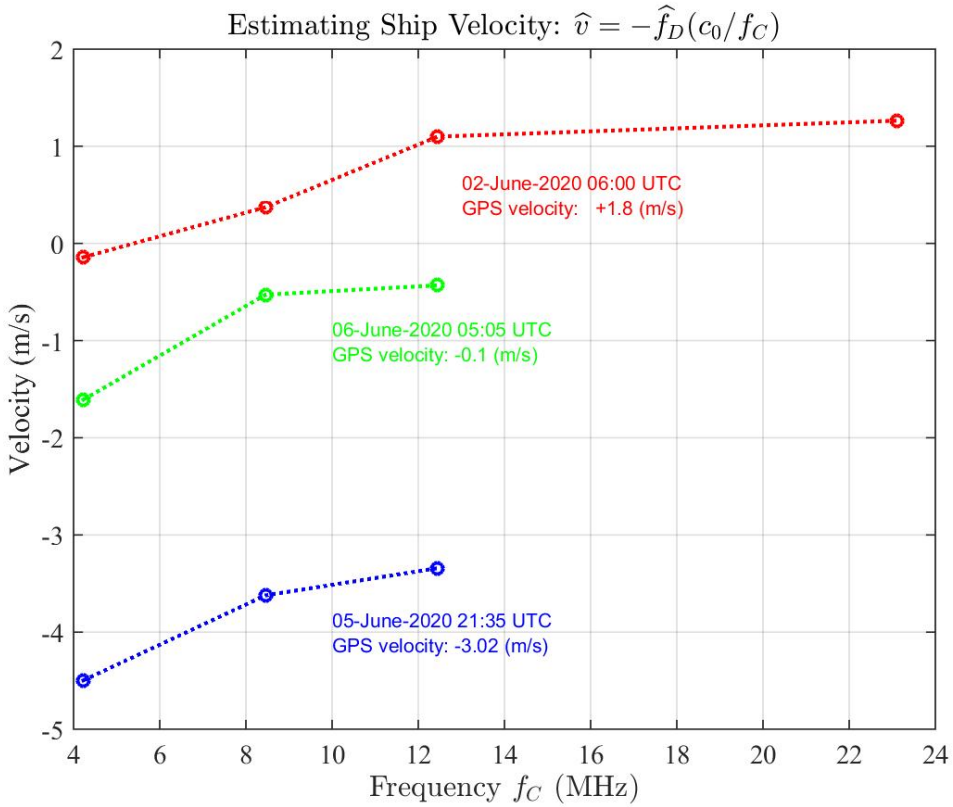


Figure 102: Trends in the ship velocity computed from the Doppler shifts.

The third gap between theory and measurements is the spectrum of the diffuse component. The measurements show the fading spectrum has a narrowband "spike" that has a Gaussian shape (See Equation 19). Watterson models the fading spectrum with a Gaussian shape for mid-latitude HF skywaves [75]. Dana offers the f^{-k} spectrums for HF skywaves shown in Figure 20. A physics-based argument is necessary to nail down the spectral shape. For these shore-to-ship surface-wave channels, a less than ideal model for the spectral shape of the diffuse component is offset by the large K factors.

Payoff: Despite these limitations in fading estimators and physical modeling, the Rician channels extracted from these measurements suffice for ship-to-ship surface-wave channel emulation. The Executive Summary pointed out these surface-wave channels are in the HF Channel Emulator's User's Manual [78]. The Executive Summary *recommended* aggregating these surface-wave channels into a mobile HF surface-wave network. Figure 103 illustrates such a networking test. The figure shows three ships starting in a mesh, moving to a relay, and disconnecting.

The ship's time-varying geometry tests the HF network's fragmentation capability. Running the ship's geometry in reverse tests the HF network's aggregation capability.



Figure 103: Shipboard HF Networks: Mesh → Relay → Disconnect.

The received signal's power varies with range and will be modeled by surface-wave propagation codes (e.g., Figure 104). The received signal's fading will be modeled as Rician (e.g., Tables 2 to 16). Additive noise will be modeled using the standard HF noise models (e.g., [36, Section 7.1.3] or [10]). An HF emulator modeling ship-to-ship surface-wave network assumes the ships are confined within 200 km and employs vertical monopoles. The Executive Summary *recommended* adding a ship-to-ship surface-wave network scenario to the HF Emulator's Technical Report [77]. Figure 81 reports skywaves arriving at 380 km range. Consequenlty, this report's final recommendation is adding a ship-to-ship surface+skywave network scenario to HF Emulator's Technical Report. Both efforts are underway and should be completed in 2024.

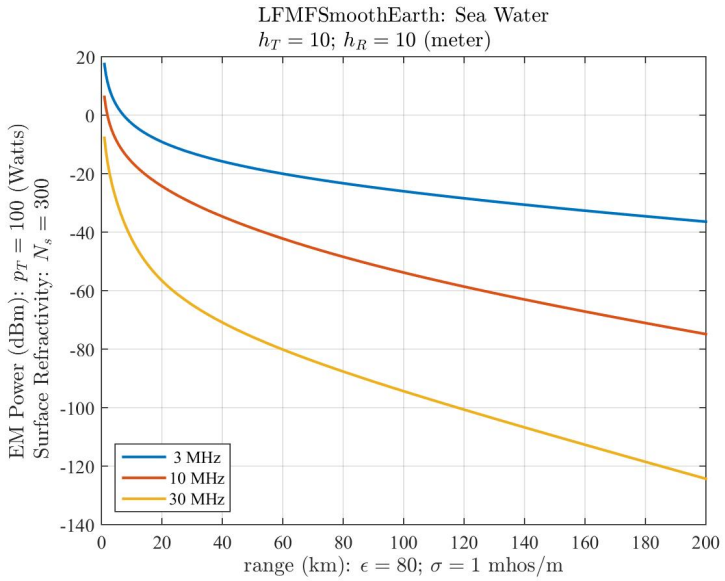


Figure 104: Surface-wave propagation at 3, 10, 30 MHz; Propagation from vertically polarized monopoles [33, Figure 1].

References

[1] Australia, Canada, New Zealand, United Kingdom, United States (AUSCANNZUKUS) [2019] *Experimentation 2018 Report, Appendix A: High Latitude Wideband High Frequency Channel Sounding*. Maritime Information Warfare Organisation, Experimentation Working Group 18-1.

[2] Abdi, Ali; Cihan Tepedelenlioglu; Mostafa Kaveh; Georgios Giannakis [2001] On the Estimation of the K Parameter for the Rice Fading Distribution, *IEEE Communication Letters*, 5(3).

[3] Abramson, Norman [1963] Bandwidth and Spectra of Phase-and-Frequency-Modulated Waves, *IEEE Transactions on Communications Systems*, 11(4).

[4] Aulin, T. [1979] A Modified Model for the Fading Signal at a Mobile Radio Channel, *IEEE Transactions in Vehicular Technology*, 28(3).

[5] Azemi, G.; B. Senadji; B. Boashash [2004] Ricean K-Factor Estimation in Mobile Communications Systems, *IEEE Communications Letters*, 8(10).

[6] Baddour, Kareem E. & Norman C. Beaulieu [2005] Robust Doppler Spread Estimation in Nonisotropic Fading Channels, *IEEE Transactions on Wireless Communions*, 4(6).

[7] Barrick, D. E. [1970] *Theory of Groundwave Propagation Across a Rough Sea at Dekameter Wavlengths*, Battelle Memorial Institute Report, Contract DAAH01-70-C-0312.

[8] Bello, Philip A. [1963] Characterization of Randomly Time-Variant Linear Channels, *IEEE Transactions on Communications Systems*, CS-11.

[9] Bello, Phillip A. [1965] On the RMS Bandwidth of Nonlinearly Envelope Detected Narrow-Band Gaussian Noise, *IEEE Transactions on Information Theory*, 11(2).

[10] Buchanan, K. ; L. Xu; C. Dilay; David Hilton [2019] Pacific Ocean HF Noise Distributions Off Southern California, *2019 URSI International Symposium on Electromagnetic Theory (EMTS)*, San Diego, CA, USA.

[11] Bhatnagar, Manav R. & Arti M.K. [2013] Performance Analysis of AF Based Hybrid Satellite-Terrestrial Cooperative Network over Generalized Fading Channels, *IEEE Communications Letters*, 17(10).

[12] Booker, H.G.; R. Lugannani; L. E. Hoff [1978] *HF Channel Simulator for Wideband Signals*, NOSC Technical Report 208, Naval Oceans Systems Center, San Diego, CA.

[13] Cheng, Dave K. [1989] *Field and Wave Electromagnetics* (second edition), Addison-Wesley Publishing Company, New York, NY.

[14] Daly, M.; J. Meloling; J. Rockway; T. Xie; W. Nielsen; P. McGinnis; A. Monges [2015] A Compact Six-Port HF Vector Sensor, *Proc. Antennas Applications Symposium*, Allerton Park, Monticello, IL.

[15] Daly, M.; J. Allen; T. Wojtaszek; M. Ontiveros [2017] Mitigation of Spectral Nulls in a Wideband HF Signal, *2017 IEEE Antennas and Propagation Symposium.*

[16] Daly, M.; J. Allen; John Meloling; Nazia Mozaffar; Marcos Ontiveros; Fred Verd; Demi Truong [2017] *Mid-Latitude Mobile Wideband HF-NVIS Channel Analysis: Part I*, SPAWAR Technical Report 3075.

[17] Daly, Michael; John Meloling; Jeffery Allen; Fred Verd; Marcos Ontiveros; Nazia Mozaffar; Jordan Melcher [2019] *Mid-Latitude Mobile Wideband HF-NVIS Channel: Part II* , NIWC Technical Report, number pending.

[18] Daly, Michael; Jeffery C. Allen; John Meloling [2020] Wideband HF-NVIS Channel: Models for Software Emulators, NIWC Technical Report, number pending.

[19] Dana, Roger A. [1991] *Propagation of RF Signals Through Structured Ionization: The General Model*, Report Number MRC-R-1262R, Mission Research Corporation, P.O. Drawer 719, Santa Barbara, CA 93102-0719.

[20] Dana, Roger A. [1992] *Temporal Statistics of Non-Rayleigh Fading*, Report Number MRC-R-1427, Mission Research Corporation, P.O. Drawer 719, Santa Barbara, CA 93102-0719.

[21] Dana, Roger A. [1993] *Statistics of Sampled Rician Fading*, Report Number MRC-R-1410, Mission Research Corporation, P.O. Drawer 719, Santa Barbara, CA 93102-0719.

[22] Dana, Roger A. & Robert L. Bogusch [2000] *Digital Communications in Fading Channels: COMLINK Validataion*, Report Number MRC-R-1531, Mission Research Corporation P.O. Drawer 719, Santa Barbara, CA 93102-0719.

[23] Davila, Celso Vargas [1993] *Comparison of HF Groundwave Propagation Models*, Master's Thesis, Naval Postgraduate School, Monterey, CA.

[24] DeMinco, N. [1986] *Ground-wave Analysis Model for MF Broadcast Systems*, National Telecommunications & Information Administration (NTIA) Report 86-203.

[25] DeRaad, Lester L., Jr. & Grover, Morgan K. [1990] *First-Order Intensity Statistics for Non-Rayleigh Fading*, Report Number RDA-TR-02261 28902-002, R & D Associates, P.O. Box 9695, Marina del Rey, CA 90295-2095.

[26] Doukas, Athanasios & Grigorios Kalivas [2006] Rician K Factor Estimation for Wireless Communication Systems, *2006 International Conference on Wireless and Mobile Communications (ICWMC'06)*, Bucharest, Romania.

[27] Daniels, Robert C. & Steven W. Peters [2013] A New MIMO HF Data Link: Designing for High Data Rates and Backwards Compatibility, *MILCOM 2013.*

[28] Eckert, Robert [1986] *Modern Methods for Calculating Ground-Wave Field Strength over a Smooth Spherical Earth*, FCC/OET R88-1.

[29] Kerr, Donald E. [1951] *Propagation of Short Radio Waves*, McGraw-Hill, New York, NY.

[30] Giunta, Gaetano; Chengpeng Hao; Danilo Orlando [2018] Estimation of Rician K-Factor in the Presence of Nakagami-m Shadowing for the LoS Component, *IEEE Wireless Communication Letters*, 7(4).

[31] Greenstein, L. J.; D. G. Michelson; V. Erceg [1999] Moment-Method Estimation of the Rice K-Factor, *IEEE Communications Letters*, 3(6).

[32] ITU [2019] *The Concept of Transmission Loss for Radio Links*, Recommendation ITU-R P.341-7 (08/2019), *International Telecommunication Union*, Geneva, Switzerland.

[33] ITU [2022] *Ground-Wave Propagation Prediction Method for Frequencies Between 10 kHz and 30 MHz*, Recommendation ITU-R P.368-10 (08/2022), *International Telecommunication Union*, Geneva, Switzerland.

[34] Kerr, Donald E. [1951] *Propagation of Short Radio Waves*, McGraw-Hill, New York, NY.

[35] Kouyoumjian. Robert G. [1965] Asymptotic High-Frequency Methods, *Proceedings of the IEEE*, 53.

[36] Kim, John C. & Eugen I. Muehldorf [1995] *Naval Shipboard Communication Systems*, Prentice-Hall, Inc., Englewood Cliffs, NJ.

[37] Logan, J. C. & J. W. Rockway [1997] *Dipole and Monopole Antenna Gain and Effective Area for Communication Formulas*, Technical Report 1756, Naval Command, Control and Ocean Surveillance Center (NCCOSC), RDT&E Division (NRaD), San Diego, CA 92152-5001.

[38] Long, Marice W. [1983] *Radar Reflectivity of Land and Sea*, Artech House, Dedham, MA.

[39] Lustgarten, M.N. & J.A. Madison [1977] An Empirical Propagation Model (EPM-73), *IEEE Tran. Electromagnetic Compatibility*, EMC-19(3).

[40] Meloling, John [2020] Private communication.

[41] Mitić, Aleksandra M. & Mihajlo Č. Stefanović [2007] Second-Order Statistics of the Signal in Ricean-Lognormal Fading Channel with Selection Combining, *Facta Universitatis (NIŠ)*, SER.: ELEC. ENERG., 20(2).

[42] Norton, Kenneth A. [1959] *Transmission Loss in Radio Propagation*, Technical Note 12, National Bureau of Standards.

[43] Norton, Kenneth A. [1941] The Calculation of Ground-Wave Field Intensity Over a Finitely Conducting Spherical Earth, *Proceedings of the IRE*, 29.

[44] Ontiveros, Marcos; Michael P. Daly; Jeffery C. Allen [2020] *Polar Skywave Radar Distributed Communications (PSRDC) FY19 Experimentation: HF Analysis*, Report prepared for NRL.

[45] Papazafeiropoulos, Anastasios K. & Stavros A. Kotsopoulos [2009] The η-λ-μ: A General Fading Distribution, *IEEE GLOBECOM*.

[46] Park, Goohyun; Takki Yu; Daesik Hong; Changeon Kang [2004] A Modified Covariance-Based Doppler Estimation Method for Rician Fading Channel, *2004 IEEE 59th Vehicular Technology Conference (VTC 2004-Spring)*, Milan, Italy.

[47] Patterson, Wayne L. [2001] *Advanced Refractive Effects Prediction System (AREPS)*, NIWC Technical Document 3117.

[48] Pielou, J.M. ; J.D. Milsom; R.N, Herring [1987] HF Ground Wave Propagation From a Cliff-Top Site, *IEE Conf ICAP87*.

[49] Portilla-Yandún, Jesús [2017] The Global Signature of Ocean Wave Spectra, *Geophysical Research Letters*, 45.

[50] Putnam, Mike [2012] *Final Report: Laser Line Scan System for UXO Characterization*, ESTCP Project Number MM-0911, SPAWAR Systems Center Pacific with Science Applications International Corporation.

[51] Proakis, [1983] *Digital Communications*, third edition, McGraw-Hill Inc., New York, NY.

[52] Pielou, J.M. ; J.D. Milsom; R.N, Herring [1987] HF Ground Wave Propagation From a Cliff-Top Site, *IEE Conf ICAP87*.

[53] Ripley, B. D. [1996] *Pattern Recognition and Neural Networks*, Cambridge University Press, New York, NY.

[54] Ryabkova, M.; V. Karaev; J. Guo; Yu. Titchenko [2019] A Review of Wave Spectrum Models as Applied to the Problem of Radar Probing of the Sea Surface, *Journal of Geophysical Research: Oceans*, 124.

[55] Ryan, Frank [1991] *User's Guide for the VTRPE (Variable Terrain Radio Parabolic Equation) Computer Code*, NIWC Pacific, Technical Report 1456.

[56] Ryan, Frank [2022] *User's Guide for the Variable Terrain Radiowave Parabolic Equation (VTRPE) Electromagnetic Wave Propagation Model, Version 4.1Y*, Applied Technology, Inc., San Diego, CA, 92103: `fjryan@ieee.org`

[57] Scott, David W. [1992] *Multivariate Density Estimation*, John Wiley & Sons, Inc., New York, NY.

[58] Sevgi, Levent [2007] Groundwave Modeling and Simulation Strategies and Path Loss Prediction Virtual Tools, *IEEE Transactions on Antennas and Propagation*, 55(6).

[59] Stefanovic, Hana; Vladimir Stefanovic; Aleksandra Cvetkovic; Jelena Anastasov; Dimitrije Stefanovic [2008] Some Statistical Characteristics of a New Shadowed Rician Fading Channel Model, *The Fourth International Conference on Wireless and Mobile Communications*, IEEE Computer Society.

[60] Shaft, P. D. [1974] On the Relationship Between Scintillation Index and Rician Fading, *IEEE Transactions on Communication*, 22(5).

[61] Scheible, Maureen P.; Lucien J. Teig; John D. Fite; Kevin M. Cuomo; Janet L. Werth; Glenn W. Meurer; Nathan C. Ferreira; Cecelia R. Franzini [2014] High Data Rate, Reliable Wideband HF Communications Demonstration, *The MITRE Corporation*.

[62] Schwartz, Mischa; William R. Bennett; Seymour Stein [1966] *Communication Systems and Techniques*, McGraw-Hill Book Company, New York, NY.

[63] Sevgi, L. & Ç. Uluışık [2006] A Matlab-Based Virtual Propagation Tool: Surface Wave Mixed-path Calculator, *Progress In Electromagnetics Research Symposium 2006*, Cambridge, USA.

[64] Sevgi, Levent [2007] Groundwave Modeling and Simulation Strategies and Path Loss Prediction Virtual Tools, *IEEE Transactions on Antennas and Propagation*, 55(6).

[65] Sijbers, Jan; Arnold J. den Dekker; Paul Scheunders; Dirk Van Dyck [1998] Maximum-Likelihood Estimation of Rician Distribution Parameters, *IEEE Transactions on Medical Imaging*,17(3).

[66] Stüber, Gordon L. [2001] *Principles of Mobile Communication*, second edition, Kluwer Academic Publishers, Boston, MA.

[67] Szajnowski, W. J. [1996] A Fast Time-Domain Estimator of the Bandwidth of a Gaussian Process, *IEEE Signal Processing Letters*, 3(60).

[68] `https://www.tcibr.com/communications-antennas`

[69] Tepedelenlioğlu, C.; A. Abdi; G. Giannakis [2003] The Ricean K factor: Estimation and Performance Analysis, *IEEE Transactions on Wireless Communications*, 4(2).

[70] Tsimenidis, C. C.; O. R. Hinton; B. S. Sharif; A. E. Adams 2000] Linear predictor based method for estimating Doppler shifts in mobile radio communication systems, *Electronics Letters*, 36(12).

[71] Valley, George C. [1975] The Relation Between the Specular-to-Interference Ratio and the Scintillation Index, *IEEE Transactions on Communications*, 23(11).

[72] `ulcar.uml.edu/directionograms.html`

[73] Villavicencio, Mirko Alberto Gomez; Rausley Adriano Amaral de Souza; Geordan Caldeira de Souza; Michel Daoud Yacoub [2016] A Bivariate κ- μ Distribution, *IEEE Transactions on Vehicular Technology*, 65(7).

[74] Wait, J. [1956] Radiation From a Vertical Antenna Over a Curved Stratified Ground, *Journal of Research of the National Bureau of Standards*, 56(4) Research Paper 2671.

[75] Watterson, C.C.; J.R. Juroshek; W.D. Bensema [1970] Experimental confirmation of an HF channel model, *Proceedings of the IEEE*, 18(6).

[76] Wyatt, Lucy R. & J. J. Green [2022] Swell and Wind-Sea Partitioning of HF Radar Directional Spectra, *Journal of Operational Oceanography*, https://doi.org/10.1080/1755876X.2022.2127232

[77] *Wideband High Frequency Channel Emulator Technical Manual, Version 3.1*, NIWC Pacific.

[78] *Wideband High Frequency Channel Emulator User's Manual, Version 3.1*, NIWC Pacific.

[79] Yu, Hyunkyu; Goohyun Park; Hangyu Cho; Changeon Kang; Daesik Hong [2005] SNR-Independent Methods for Estimating Maximum Doppler Frequency, *IEEE Signal Processing Letters*, 12(5).

[80] Zhang, Jiayi; Wen Zeng; Xu Li; Qiang Sun; Kostas P. Peppas [2018] New Results on the Fluctuating Two-Ray Model with Arbitrary Fading Parameters and Its Applications, *IEEE Transactions on Vehicular Technology*, 67(3).

[81] Zhang, Hong [2007] *Doppler Spread Estimation in Mobile Fading Channels* PhD Thesis, New Jersey Institute of Technology, Department of Electrical and Computer Engineering.

A Rician Fading and Estimation

The surface-wave channels are well-modeled by a single tap

$$h_{\mathsf{SW}}(t,\tau) = h(t)\delta(\tau - \tau_G)$$

where the fading $\{h(t)\}$ is Rician. characteristics. This section reviews Rician fading and estimators. Standard Rician fading has the form

$$h(t) = s_{\mathsf{LOS}} + g(t)$$

where the constant s_{LOS} is called the *specular component* and the random process $\{g(t)\}$ is called the *diffuse component*. Stüber offers the following insight for modeling Rician fading [66, page 52]:

> A very simple Rician fading model assumes means ... are constant. Such an approach will certainly yield a Rician distributed envelope but will not realistically model higher-order envelope statistics or a particular scattering environment.

Stüber recommends including Doppler shifts. Some models shift the specular component and the diffuse component with different Doppler frequencies. This report applies a single Doppler shift on the standard Rician fading.

Definition 1 (Rician [66], [4]) *The Rician fading model has the form*

$$h(t) = e^{j2\pi f_D t}\left\{s_{\mathsf{LOS}} + g(t)\right\},$$

where f_D denotes the Doppler shift, the specular component s_{LOS} *is a complex-valued constant, and the* diffuse component $\{g(t)\}$ *is a complex-valued, zero-mean, circular Gaussian process with variance σ_g^2 and* power spectrum $P_{gg}(f)$*. The average envelope power p_E is the sum of the* specular power *and the* diffuse power *[66, page 53]*

$$p_E = |s_{\mathsf{LOS}}|^2 + \sigma_g^2. \tag{17}$$

The Rician K factor is the ratio of the specular to the scattered power [66, page 53]:

$$K = 10 \cdot \log_{10}\left(\frac{|s_{\mathsf{LOS}}|^2}{\sigma_g^2}\right) \quad [\text{dB}]. \tag{18}$$

There are multiple spectral models for the diffuse component. For the medium-haul, mid-latitude skywaves, Watterson observed a Gaussian power spectrum [75]:

$$P_{gg}(f) = \frac{\sigma_g^2}{f_N\sqrt{2\pi}}\exp\left(-\frac{f^2}{2f_N^2}\right), \tag{19}$$

where f_N is the RMS bandwidth *[3].*

Definition 2 (RMS Bandwidth) *Let* $\{g(t)\}$ *be a wide-sense stationary random process with integrable power spectrum* $P_{gg}(f)$. *Introduce the normalized spectral density*

$$\mathbb{P}_{gg}(f) = P_{gg}(f) \cdot \left(\int_{-\infty}^{\infty} P_{gg}(f) df \right)^{-1}.$$

The mean frequency is [9, Eq. 5]

$$f_{\mathsf{M}} = \int_{-\infty}^{\infty} f \cdot \mathbb{P}_{gg}(f) df.$$

The RMS bandwidth *is the standard deviation of the power spectrum [62, Eq. 9-2-63], [9]*

$$f_{\mathsf{RMS}} = \left(\int_{-\infty}^{\infty} (f - f_{\mathsf{M}})^2 \cdot \mathbb{P}_{gg}(f) df \right)^{1/2}.$$

Remarks: (*i*) "RMS frequency" is also used [62, Eq. 9-2-63]. (*ii*) The Rician spectrum given by Equation 19 has $f_N = f_{\mathsf{RMS}}$. (*iii*) Bello employs a factor of 2 [9, Eq. 4]. (*iv*) Dana [21] lists other power spectrum for the diffuse component (See Figure 20).

The following sections compare estimators of $\{p_E, K, f_D, f_N\}$. These parameters model the Rician processes as follows:

$$h(t) = e^{j2\pi f_D t} \left\{ s_{\mathsf{LOS}} + g(t) \right\}; \quad \left\{ \begin{array}{r} s_{\mathsf{LOS}} = p_E K (K+1)^{-1} \\ \sigma_g^2 = p_E (K+1)^{-1} \end{array} \right. .$$

Estimates of these parameters are reported on the fading plots with the "hat" notation (e.g., $\widehat{p}_E$). The moment-based estimators employ the following notation. If $\{h(t)\}$ and $\{g(t)\}$ are jointly WSS, their covariance is denoted as

$$R_{hg}(\tau) = E\left[h(t) \overline{g(t+\tau)} \right]$$

and naturally leads to the estimate

$$\widehat{R}_{hg}(N;\tau) = \frac{1}{N} \sum_{n=1}^{N} h(t_n) \overline{g(t_n + \tau)}.$$

A.1 Envelope Power

The fading process admits the following maximum-likelihood estimate for its envelope power [2]:

$$p_E = |s_{\mathsf{LOS}}|^2 + \sigma_g^2 = E[|h(t)|^2] = R_{hh}(0) \approx \widehat{R}_{hh}(N;0) = \widehat{p}_E.$$

A.2 Doppler Shift

There are multiple estimators for the Doppler shift f_D [46], [70], [79]. A moment-based estimate derived in Theorem 1 is as follows:

$$f_D = -\frac{1}{j2\pi}\frac{R_{h\dot{h}}(0)}{R_{hh}(0)} \approx -\frac{1}{j2\pi}\frac{\widehat{R}_{h\dot{h}}(N;0)}{\widehat{R}_{hh}(N;0)} = \widehat{f}_D. \tag{20}$$

Figure 105 plots the Doppler-shift estimate $\widehat{f}_D$ as a function the Rician K factor. Each curve on the plot is a Doppler shift estimate $\widehat{f}_D$ as a function of K computed from Rician simulations

$$h(t) = e^{j2\pi f_D t}\left\{s_{\mathsf{LOS}} + g(t)\right\}; \quad \left\{\begin{array}{ll} p_E = 0 & [\text{dB}] \\ f_N = 10 & [\text{Hz}] \end{array}\right. .$$

The plot makes sense because increasing K moves the fading to the deterministic function:

$$h(t) \approx \exp(j2\pi f_D t) \quad (K \gg 1).$$

What is surprising is that the estimator did not fall apart for small K factors.

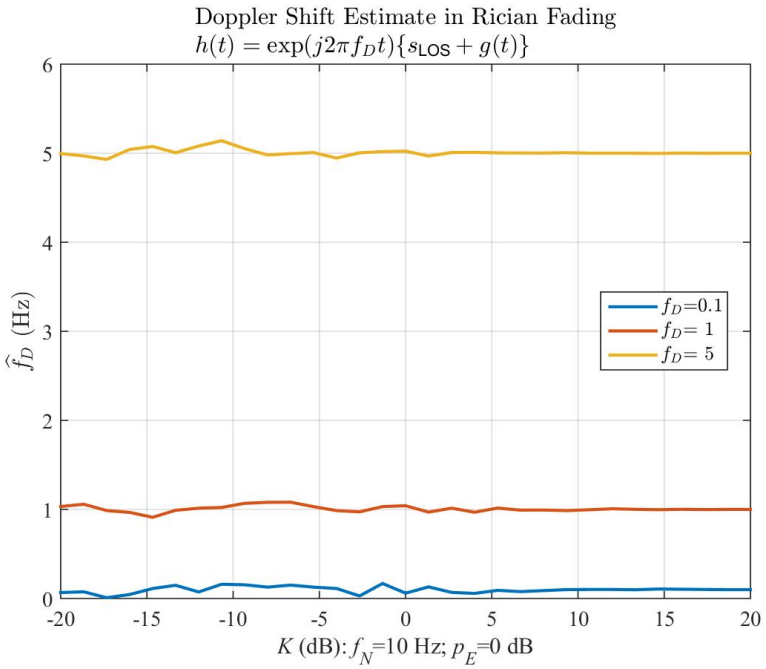


Figure 105: Doppler shift estimates $\widehat{f}_D$ as a function of K for envelope power $p_E = 0$ dB and RMS bandwidth $f_N = 10$ Hz.

A.3 Rician K Factor

Estimators for the Rician K factor fall into the following classes:

- Moments
- Histogram
- Maximum Likelihood
- Filtering

This section compares estimators from all classes. The estimators are all comparable on Rician simulations, provided $K > 0$ dB.

A.3.1 Moments

A concise review of moment-based estimators is found in [2]. Moment-based estimators have varying levels of success. For example, the μ estimate is based on the first-order moments [26], [2, Eq. 1]

$$\mu = \frac{E[|h(t)|]}{\sqrt{E[|h(t)|^2]}} = \frac{\sqrt{\pi}}{2}\frac{e^{-K/2}}{\sqrt{K+1}}\left\{(K+1)I_0\left(\frac{K}{2}\right) + KI_1\left(\frac{K}{2}\right)\right\}. \tag{21}$$

The μ estimate is problematic because the μ estimate converges to unity as K get large. The γ estimate is based on fourth-order moments [2, Eq. 2]:

$$\gamma = \frac{\mathsf{Var}[|h(t)|^2]}{E[|h(t)|^2]^2} = \frac{2K+1}{(K+1)^2}. \tag{22}$$

Figure 106 plots the estimate $\widehat{K}$ as a function the Rician K factor. Each curve on the plot is computed from the Rician simulations

$$h(t) = e^{j2\pi f_D t}\left\{s_{\mathsf{LOS}} + g(t)\right\}; \quad \left\{\begin{array}{ll} p_E = 0 & [\text{dB}] \\ f_D = 5 & [\text{Hz}] \end{array}\right.$$

for selected f_N bandwidths. The plot shows the γ estimate is a robust estimator for $K > 0$ dB.

A.3.2 Histogram

The histogram estimator fits a Rician distribution to the averaged-shifted histogram (ASH) as described in Equation 13:

$$\left\{\widehat{s}_{\mathsf{LOS}}, \widehat{\sigma}_g^2\right\} = \mathsf{argmin}\left\{d(p_{\mathsf{ASH}}||p_{\mathsf{RICE}}(s_{\mathsf{LOS}}, \sigma_g^2)) : \widehat{p}_E = |s_{\mathsf{LOS}}|^2 + \sigma_g^2\right\}.$$

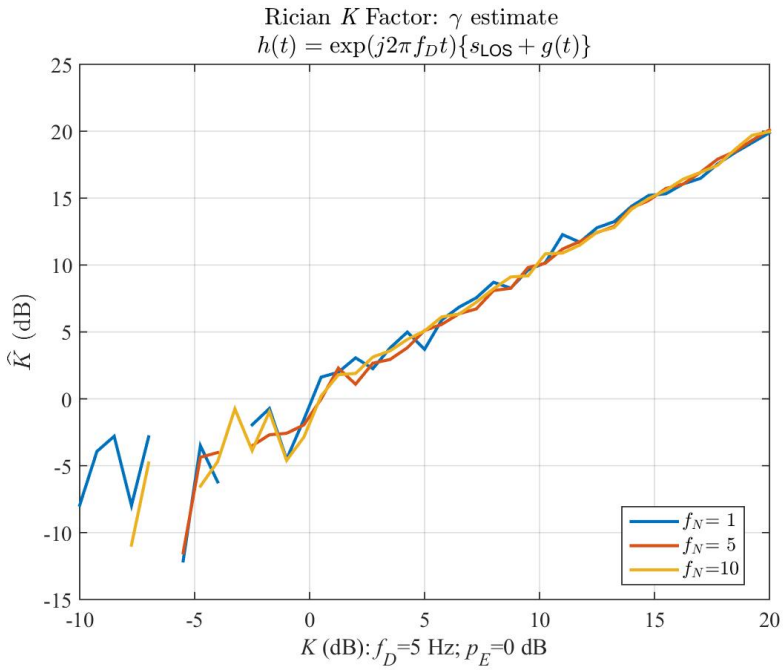


Figure 106: Performance of the moment estimator of $\widehat{K}$ as a function of K and RMS bandwidths f_N for the envelope power $p_E = 0$ dB and $f_D = 5$ Hz.

The Histogram estimate of the K factor is

$$\widehat{K} = \frac{|\widehat{s}_{\mathsf{LOS}}|^2}{\widehat{\sigma}_g^2}.$$

Figure 107 plots the estimate $\widehat{K}$ as a function the Rician K factor. Each curve on the plot is computed from the Rician simulations

$$h(t) = e^{j2\pi f_D t}\left\{s_{\mathsf{LOS}} + g(t)\right\}; \quad \left\{ \begin{array}{ll} p_E = 0 & [\text{dB}] \\ f_D = 5 & [\text{Hz}] \end{array} \right.$$

for selected f_N bandwidths. The plot shows the histogram is a robust estimator for $K > 0$ dB.

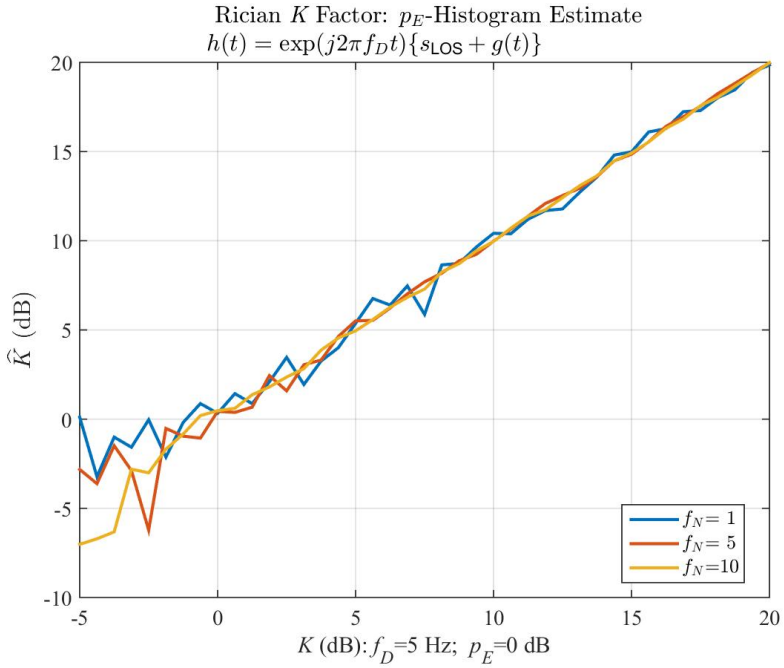


Figure 107: Performance of the Histogram estimator of $\widehat{K}$ as a function of K and RMS bandwidths f_N for the envelope power $p_E = 0$ dB and $f_D = 5$ Hz.

A.3.3 Maximum-Likelihood

This maximum-likelihood estimator performed well on simulated Rican fading but failed on the measured Rician fading. This estimator is reviewed in this section but not included in ensemble of Rician estimators in the main report. The maximum-likelihood estimator for the K factor assumes the fading amplitude

$$R(t) = |h(t)| \tag{23}$$

has a Rician probability density function [66, Eq. 2.45]:

$$p_{\mathsf{RICE}}\left(|s_{\mathsf{LOS}}|, \sigma_g^2; r\right) = \frac{2r}{\sigma_g^2} \exp\left(-\frac{r^2 + |s_{\mathsf{LOS}}|^2}{\sigma_g^2}\right) I_0\left(2\frac{r|s_{\mathsf{LOS}}|}{\sigma_g^2}\right).$$

This density is modified to account for the average power written as

$$p_E = |s_{\mathsf{LOS}}|^2 + \sigma_g^2.$$

Standard maximum likelihood maximizes the sample probability [65]:

$$\{\widehat{s}_{\mathsf{LOS}}, \widehat{\sigma}_g^2\} = \mathsf{argmax}\left\{\prod_{n=1}^{N} p_R\left(|s_{\mathsf{LOS}}|, \sigma_g^2; R(t_n)\right)\right\},$$

where $\{R(t_n)\}$ are assumed to be independent samples of $\{R(t)\}$. The maximum likelihood estimate in this report maximizes the sample probability under the sample power constraint:

$$\{\widehat{s}_{\mathsf{LOS}}, \widehat{\sigma}_g^2\} = \mathsf{argmax}\left\{\prod_{n=1}^{N} p_R\left(|s_{\mathsf{LOS}}|, \sigma_g^2; R(t_n)\right) : \widehat{p}_E = |s_{\mathsf{LOS}}|^2 + \sigma_g^2\right\}$$

and estimates the K factor as

$$\widehat{K} = \frac{|\widehat{s}_{\mathsf{LOS}}|^2}{\widehat{\sigma}_g^2}.$$

Figure 108 illustrates the performance of this estimator on simulated Rician fading. The Rician simulations hold the envelope power and Doppler shift constant but vary the K factor -5 to $+20$ dB for three RMS bandwidths. The estimated $\widehat{K}$ are credible down to $K = 0$ dB. As remarked at the beginning of this section, this estimator failed on the measured fading and is not part of the Rician estimators.

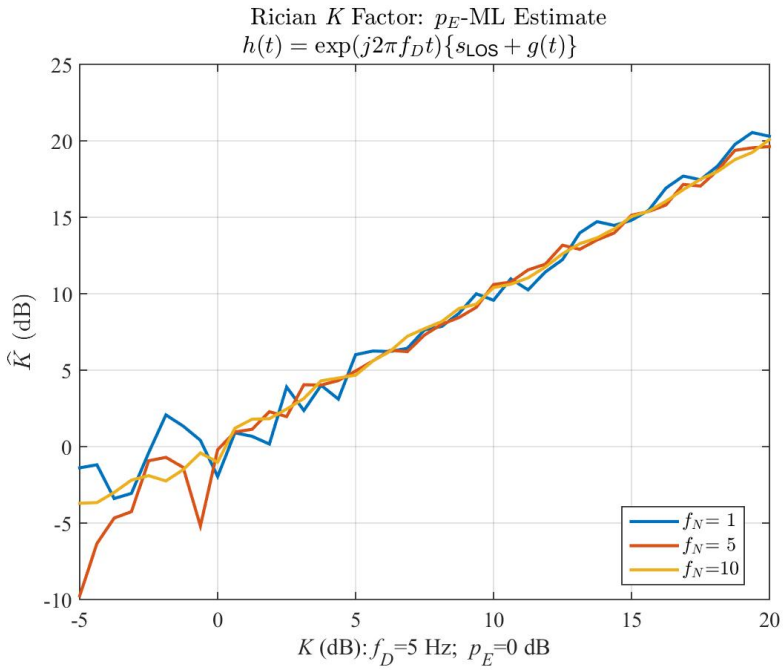


Figure 108: Performance of the p_E-constrained maximum-likelihood estimator of $\widehat{K}$ as a function of K and RMS bandwidths f_N for the envelope power $p_E = 0$ dB and $f_D = 5$ Hz.

A.3.4 Filtering

The method estimates the K factor by filtering the specular component from the diffuse component. Assuming a Doppler estimate $\widehat{f}_D$ and an estimate of the bandwidth $\widehat{f}_B$ of the specular component locate the Doppler shift f_D as

$$|f_D - \widehat{f}_D| < \widehat{f}_B.$$

Let filter denote an ideal bandpass filter with passband $\widehat{f}_D \pm \widehat{f}_B$. The action of this filter on the Rician fading is

$$\mathsf{filter}(h(t)) = s_{\mathsf{LOS}} e^{j2\pi f_D t} + \mathsf{filter}(g(t)).$$

The in-band filtered power is bounded below:

$$E[|\mathsf{filter}(h(t))|^2] = |s_{\mathsf{LOS}}|^2 + \int_{\widehat{f}_D - \widehat{f}_B}^{\widehat{f}_D + \widehat{f}_B} P_{gg}(f) df > |s_{\mathsf{LOS}}|^2.$$

The out-of-band filtered power is bounded above

$$E[|h(t) - \mathsf{filter}(h(t))|^2] = \int_{-\infty}^{\widehat{f}_D - \widehat{f}_B} P_{gg}(f) df + \int_{\widehat{f}_D + \widehat{f}_B}^{\infty} P_{gg}(f) df < \sigma_g^2.$$

Consequently, the filter estimate is an upper bound for the K factor:

$$\frac{E[|\mathsf{filter}(h(t))|^2]}{E[|h(t) - \mathsf{filter}(h(t))|^2]} > K. \tag{24}$$

The "tightness" of this upper bound depends on the bandwidth of the filter. Figure 109 plots the estimate $\widehat{K}$ as a function the Rician K factor. Each curve on the plot is computed from the Rician simulations

$$h(t) = e^{j2\pi f_D t} \left\{ s_{\mathsf{LOS}} + g(t) \right\}; \quad \left\{ \begin{array}{ll} p_E = 0 & [\text{dB}] \\ f_D = 5 & [\text{Hz}] \end{array} \right. ,$$

over selected RMS values. The Doppler shift $\widehat{f_D}$ is estimated using Equation 20. The bandwidth, for these simulations, is set as 10% of the estimated Doppler shift:

$$\widehat{f_B} = 0.1 \times \widehat{f_D}. \tag{25}$$

The plots verify this filtered estimate of $\widehat{K}$ is a tight upper bound for the actual K value. This upper bound holds when applied to the measured surface-wave channels. Both the moment-based and the histogram estimates of the K factor are bounded by this filter-based K-factor estimate.

Improvements in the filter method lie in adapting the bandwidth of Equation 25 to the time series under consideration. This report uses the 10% bandwidth without regard for the RMS bandwidth in the fading or the noise floor. The measurements show that a high noise floor obscures the spectral width of the diffuse component. In this case, a good *adaptive* filter would employ a bandwidth $\widehat{f_B}$ to only filter that part of the diffuse component that rises above the noise—not a straight 10% of the Doppler shift.

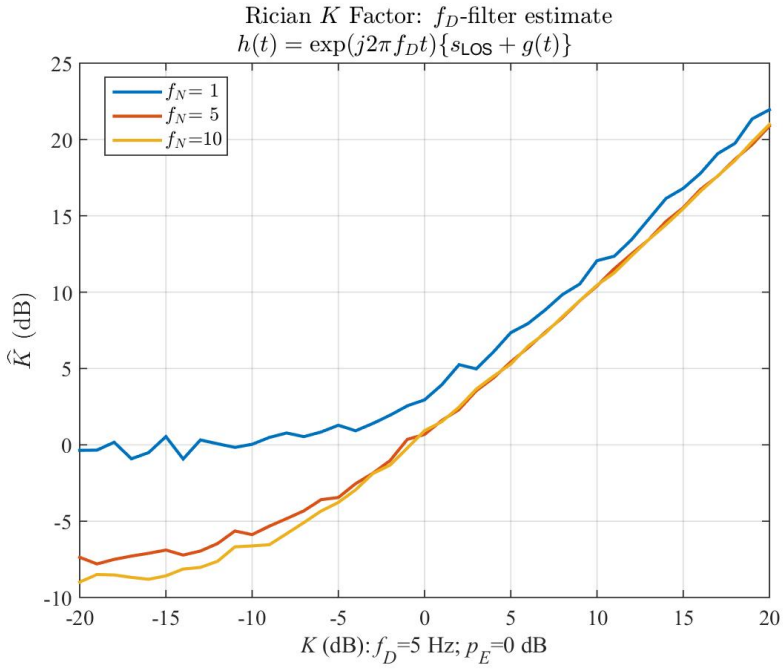


Figure 109: Performance of the f_D-filter estimate $\widehat{K}$ as a function of K and RMS bandwidths f_N for envelope power $p_E = 0$ dB and $f_D = 5$ Hz.

A.4 RMS Bandwidth

Estimates of the RMS bandwidth f_{RMS} are based on moments or level crossings.

A.4.1 Moments

One moment-based estimator is derived in Theorem 4:

$$\frac{R_{\dot{h}\dot{h}}(0)}{R_{hh}(0)} = 4\pi^2 f_D^2 + \frac{4\pi^2}{K+1} f_{\mathsf{RMS}}^2. \tag{26}$$

When the Rician fading has the Gaussian spectrum of Equation 19, $f_{\mathsf{RMS}} = f_N$. Figure 110 plots estimates of $\widehat{f_N}$ as a function the Rician K factor. Each curve on the plot is computed from the Rician simulations

$$h(t) = e^{j2\pi f_D t}\left\{s_{\mathsf{LOS}} + g(t)\right\}; \quad \begin{cases} p_E = 0 & [\text{dB}] \\ f_D = 5 & [\text{Hz}] \end{cases}$$

over selected RMS values. The Doppler shift f_D is replaced with the moment-based estimate $\widehat{f_D}$ from Equation 20. The Rician K factor is replaced with the moment-based estimate $\widehat{K}$ from Equation 22. The figure shows that estimating f_N from these moments delivers credible performance for $K > 0$ and continues to function for $K < 0$.

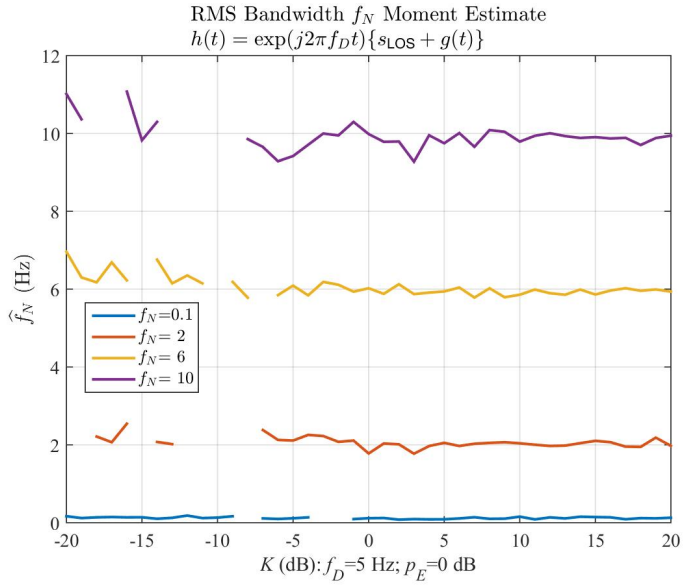


Figure 110: Moment estimator's performance for $\widehat{f_N}$ as a function of K and RMS bandwidths f_N for envelope power $p_E = 0$ dB and $f_D = 5$ Hz.

A.4.2 Level Crossings

This report employs a Rayleigh level-crossing and a Rician level-crossing to estimate RMS bandwidth. When there is no specular component, Rayleigh level-crossing is based on [62, Eq. 9-2-62]:

$$f_e = 1.1475 f_N \quad [\text{Hz}], \tag{27}$$

where the fade rate f_e is the average rate of downward excursions of the envelope across its median level. The filtering method of Section A.3.4 approximately separates the fading into its specular and diffuse components. Applying this Rayleigh level-crossing to approximate diffuse component produces RMS bandwidth estimates listed in the tables as "Filtering+Rayleigh Level Crossing".

Dana authored remarkable series of reports on HF propagation [19], Rician fading [20], and radio performance in Rician noise [22]. In particular, Dana generalized Rice's level-crossing analysis [21]. The expected number of downward excursions $N(r,T)$ of the envelope $\{|h(t)|\}$ across level r in a time increment from t to $t+T$ is adapted from [21, page 16]:

$$E[N(r,T)] = 2\sqrt{\pi} f_N T \, \frac{r}{\sigma_g} \exp\left(-\frac{r^2 + |s_{\mathsf{LOS}}|^2}{\sigma_g^2}\right) I_0\left(\frac{2r|s_{\mathsf{LOS}}|}{\sigma_g^2}\right). \tag{28}$$

The specular and diffuse components are replaced with their estimates obtained by inverting the equations:

$$\begin{aligned} \widehat{p}_E &= |\widehat{s}_{\mathsf{LOS}}|^2 + \widehat{\sigma}_g^2 \\ \widehat{K} &= \frac{|\widehat{s}_{\mathsf{LOS}}|^2}{\widehat{\sigma}_g^2}, \end{aligned}$$

where $\widehat{p}_E$ and $\widehat{K}$ are the estimates from Equations 7 and 22, respectively. Figure 111 shows the level-crossing estimates of f_N as a function the Rician K factor. Each curve on the plot is computed from the Rician simulations

$$h(t) = e^{j2\pi f_D t}\left\{s_{\mathsf{LOS}} + g(t)\right\}; \quad \begin{cases} p_E = 0 & [\text{dB}] \\ f_D = 5 & [\text{Hz}] \end{cases}$$

over selected RMS values. The level-crossing estimate employs the median of the envelope $\{|h(t)|\}$ although Equation 28 allows other level-crossing values. The plot shows the level-crossing estimate of f_N is credible for $K > 0$. Applying this Rician level-crossing to the measured fading produces RMS bandwidth estimates listed in the tables as "Histogram+Rician Level Crossing".

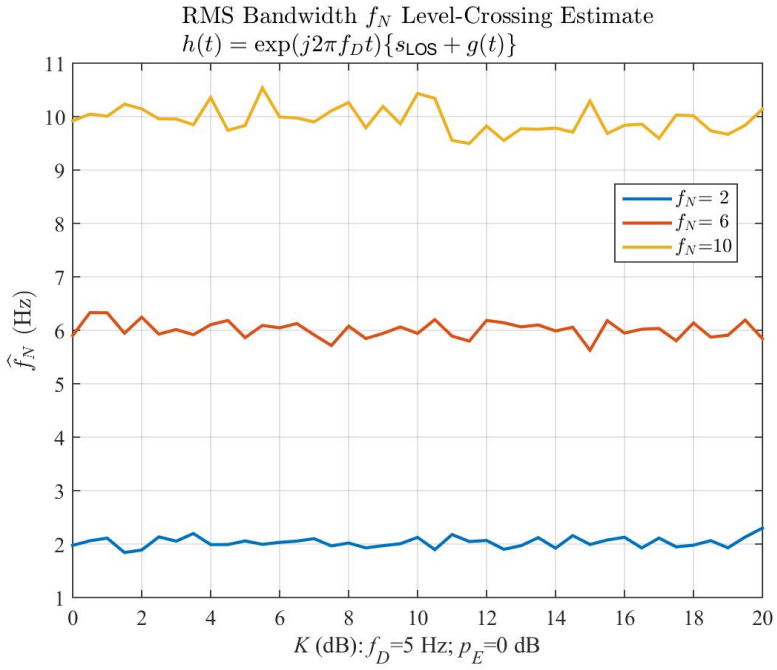


Figure 111: Rician level-crossing performance for $\widehat{f_N}$ as a function of K and RMS bandwidths f_N for envelope power $p_E = 0$ dB and $f_D = 5$ Hz.

B Gaussian Notebook

This section archives technical results supporting the Rician estimators in Appendix A.

Lemma 1 *let X and Y be real-valued, zero-mean, independent Gaussian random variables with equal variances $\sigma_X^2 = \sigma_Y^2$. If $G = X + jY$,*

$$\begin{aligned} E[G^2] &= 0 \\ E[\overline{G}|G|^2] &= 0 \end{aligned}$$

Proof:

$$E[G^2] = E[X^2] + 2jE[XY] - E[Y^2] = \sigma_X^2/2 + 0 - \sigma_Y^2/2 = 0.$$

$$E[\overline{G}|G|^2] = E[(X - jY)(X^2 + Y^2)] = E[X^3] + E[XY^2] - jE[YX^2] - jE[Y^3] = 0.$$

□

Lemma 2 *Let $\{g(t)\}$ be a WSS harmonizable random process with spectral representation*

$$g(t) = \int_{-\infty}^{\infty} e^{+j2\pi ft} G(f) df,$$

where $\{G(f)\}$ is the zero-mean generalized random process

$$E[G(f_1)\overline{G}(f_2)] = S_{gg}(f_1, f_2) = \delta(f_1 - f_2) P_{gg}(f_1).$$

Then

$$\dot{g}(t) = j2\pi \int_{-\infty}^{\infty} e^{+j2\pi ft} f dG(f)$$

and random process $\{g(t)\}$ and $\{g\dot{(}t)\}$ are jointly WSS with

$$R_{g\dot{g}}(\tau) = j2\pi \int_{-\infty}^{\infty} e^{j2\pi f\tau} f P_{gg}(f) df$$

and

$$R_{\dot{g}\dot{g}}(\tau) = 4\pi^2 \int_{-\infty}^{\infty} e^{j2\pi f\tau} f^2 P_{gg}(f) df.$$

Proof:

$$\begin{aligned} E[g(t_1)\overline{\dot{g}(t_2)}] &= j2\pi \int_{-\infty}^{\infty}\int_{-\infty}^{\infty} e^{+j2\pi f_1 t_1} e^{-j2\pi f_2 t_2} f_2 S_{gg}(f_1, f_2) df_1 df_2 \\ &= j2\pi \int_{-\infty}^{\infty}\int_{-\infty}^{\infty} e^{j2\pi\{f_1 t_1 - f_2 t_2\}} f_2 \delta(f_1 - f_2) P_{gg}(f_1) df_1 df_2 \\ &= j2\pi \int_{-\infty}^{\infty} e^{j2\pi f_1\{t_1 - t_2\}} f_1 P_{gg}(f_1) df_1. \end{aligned}$$

$$\begin{aligned} E[\dot{g}(t_1)\overline{\dot{g}(t_2)}] &= 4\pi^2 \int_{-\infty}^{\infty}\int_{-\infty}^{\infty} e^{+j2\pi f_1 t_1} e^{-j2\pi f_2 t_2} f_1 f_2 S_{gg}(f_1, f_2) df_1 df_2 \\ &= 4\pi^2 \int_{-\infty}^{\infty}\int_{-\infty}^{\infty} e^{j2\pi\{f_1 t_1 - f_2 t_2\}} f-1 f_2 \delta(f_1 - f_2) P_{gg}(f_1) df_1 df_2 \\ &= 4\pi^2 \int_{-\infty}^{\infty} e^{j2\pi f_1\{t_1 - t_2\}} f_1^2 P_{gg}(f_1) df_1. \end{aligned}$$

□

Lemma 3

$$R_{hh}(\tau) = e^{j2\pi f_D \tau}\left\{|s_{\mathsf{LOS}}|^2 + R_{gg}(\tau)\right\}$$
$$R_{h\dot{h}}(\tau) = e^{j2\pi f_D \tau}\ R_{g\dot{g}}(\tau) - j2\pi f_D R_{hh}(\tau)$$

$$\begin{aligned} R_{h\dot{h}}(\tau) &= e^{j2\pi f_D \tau}\left\{4\pi^2 f_D^2 |s_{\mathsf{LOS}}|^2 + R_{\dot{g}\dot{g}}(\tau) + j2\pi f_D R_{g\dot{g}}(\tau)\right. \\ &\quad \left. -j2\pi f_D R_{\dot{g}g}(\tau) + 4\pi^2 f_D^2 R_{gg}(\tau)\right\}. \end{aligned}$$

Proof: This covariance computation of $\{h(t)\}$ relies on the fact that $\{g(t)\}$ has zero mean so that the expectation zeros the cross terms:

$$\begin{aligned} E[h(t_1)\overline{h(t_2)}] &= E[e^{j2\pi f_D t_1}\{s_{\mathsf{LOS}} + g(t_1)\} e^{-j2\pi f_D t_2}\{\overline{s}_{\mathsf{LOS}} + \overline{g(t_2)}\}] \\ &= e^{j2\pi f_D\{t_1 - t_2\}}\left\{|s_{\mathsf{LOS}}|^2 + R_{gg}(t_1 - t_2)\right\} \end{aligned}$$

For the covariance with the derivative $\{\dot{h}(t)\}$, the full computation is worked out:

$$\begin{aligned} &E[h(t_1)\overline{\dot{h}(t_2)}] = E[e^{j2\pi f_D t_1}\{s_{\mathsf{LOS}} + g(t_1)\}\ \overline{e^{j2\pi f_D t_2}\dot{g}(t_2) + j2\pi f_D e^{j2\pi f_D t_2}\{s_{\mathsf{LOS}} + g(t_2)\}}] \\ &= e^{j2\pi f_D\{t_1 - t_2\}} E[\{s_{\mathsf{LOS}} + g(t_1)\}\{\ \overline{\dot{g}(t_2)} - j2\pi f_D \overline{s_{\mathsf{LOS}}} - j2\pi f_D \overline{g(t_2)}\ \}] \\ &= e^{j2\pi f_D\{t_1 - t_2\}}\Big\{E[s_{\mathsf{LOS}}\overline{\dot{g}(t_2)}] - j2\pi f_D |s_{\mathsf{LOS}}|^2 - j2\pi f_D E[s_{\mathsf{LOS}}\overline{g(t_2)}] \\ &\quad + E[g(t_1)\overline{\dot{g}(t_2)}] - j2\pi f_D E[g(t_1)\overline{s_{\mathsf{LOS}}}] - j2\pi f_D E[g(t_1)\overline{g(t_2)}]\Big\} \\ &= e^{j2\pi f_D\{t_1 - t_2\}}\left\{0 - j2\pi f_D |s_{\mathsf{LOS}}|^2 - 0 + R_{g\dot{g}}(t_1 - t_2) - 0 - j2\pi f_D R_{gg}(t_1 - t_2)\right\}. \end{aligned}$$

Observe the presence of the covariance of $\{h(t)\}$:

$$\begin{aligned} R_{h\dot{h}}(\tau) &= e^{j2\pi f_D \tau}\left\{-j2\pi f_D |s_{\mathsf{LOS}}|^2 + R_{g\dot{g}}(\tau) - j2\pi f_D R_{gg}(\tau)\right\} \\ &= e^{j2\pi f_D \tau}\left\{R_{g\dot{g}}(\tau) - j2\pi f_D\{|s_{\mathsf{LOS}}|^2 + R_{gg}(\tau)\}\right\} \\ &= e^{j2\pi f_D \tau} R_{g\dot{g}}(\tau) - j2\pi f_D R_{hh}(\tau). \end{aligned}$$

For the covariance with both derivatives

$$\begin{aligned} E[\dot{h}(t_1)\overline{\dot{h}(t_2)}] &= \left[\left(e^{j2\pi f_D t_1}\left(\dot{g}(t_1)+j2\pi f_D\{s_{\mathsf{LOS}}+g(t_1)\}\right)\right)\right. \\ &\times \left.\overline{\left(e^{j2\pi f_D t_2}\left(\dot{g}(t_2)+j2\pi f_D s_{\mathsf{LOS}}+j2\pi f_D g(t_2)\}\right)\right)}\right] \\ &= e^{j2\pi f_D\{t_1-t_2\}}E\left[\left(\dot{g}(t_1)+j2\pi f_D s_{\mathsf{LOS}}+j2\pi f_D g(t_1)\right)\right. \\ &\times \left.\left(\overline{\dot{g}(t_2)}-j2\pi f_D\overline{s_{\mathsf{LOS}}}-j2\pi f_D\overline{g(t_2)}\right)\right] \\ &= e^{j2\pi f_D\{t_1-t_2\}}\left\{R_{\dot{g}\dot{g}}(t_1,t_2)+0-j2\pi f_D R_{\dot{g}g}(t_1,t_2)\right. \\ &+ 0+4\pi^2 f_D^2|s_{\mathsf{LOS}}|^2+0 \\ &+ \left.j2\pi f_D R_{g\dot{g}}(t_1,t_2)+0+4\pi^2 f_D^2 R_{gg}(t_1,t_2)\right\}. \end{aligned}$$

$$\begin{aligned} R_{\dot{h}h}(t_1,t_2) &= e^{j2\pi f_D\{t_1-t_2\}}\left\{4\pi^2 f_D^2|s_{\mathsf{LOS}}|^2+R_{\dot{g}\dot{g}}(t_1,t_2)+j2\pi f_D R_{g\dot{g}}(t_1,t_2)\right. \\ &\quad \left.-j2\pi f_D R_{\dot{g}g}(t_1,t_2)+4\pi^2 f_D^2 R_{gg}(t_1,t_2)\right\}. \end{aligned}$$

□

B.1 Doppler Moment

Theorem 1 *Let $\{g(t)\}$ be a zero-mean WSS harmonizable random process with covariance*

$$R_{gg}(\tau)=\int_{-\infty}^{\infty}e^{j2\pi f\tau}P_{gg}(f)df.$$

Assume the power spectrum of $\{g(t)\}$ is even: $P_{gg}(f)=P_{gg}(-f)$. Let $\{h(t)\}$ be the Rician process:

$$h(t)=e^{j2\pi f_D t}\{s_{\mathsf{LOS}}+g(t)\}.$$

An estimator for the Doppler shift is

$$\frac{R_{h\dot{h}}(0)}{R_{hh}(0)}=-j2\pi f_D.$$

Proof: Lemma 3 computes:

$$R_{hh}(0)=|s_{\mathsf{LOS}}|^2+\sigma_g^2.$$

Lemma 2 shows that a symmetric power spectrum $P_{gg}(f)$ forces $R_{g\dot{g}}(0)=0$. Lemma 3 computes:

$$R_{h\dot{h}}(0)=R_{g\dot{g}}(0)-j2\pi f_D|s_{\mathsf{LOS}}|^2-j2\pi f_D R_{gg}(0)=-j2\pi f_D R_{hh}(0).$$

□

B.2 K Factor Moments

Theorem 2 *Let $\{h(t)\}$ be the Rician process:*

$$h(t) = e^{j2\pi f_D t}\{s_{\mathsf{LOS}} + g(t)\}.$$

An estimator for the K factor is

$$E[|h(t)|] = \sigma_g \frac{\sqrt{\pi}}{2} e^{-K/2} \left\{(1+K)I_0(K/2) + KI_1(K/2)\right\}.$$

Proof: The Rician distribution is [66, Equation 2.45]

$$p_R(r) = \frac{r}{\sigma^2} \exp\left(-\frac{r^2+s^2}{2\sigma^2}\right) I_0\left(\frac{rs}{\sigma^2}\right)$$

replacing the standard "$2\sigma^2$ with σ_g^2. The first moment is [69]

$$\begin{aligned} E[|h(t)|] &= \sigma_g \sqrt{\frac{\pi}{2}} L_{1/2}\left(-\frac{s^2}{2\sigma^2}\right) \\ &= \sigma_g \sqrt{\frac{\pi}{2}} L_{1/2}\left(-K\right) \\ &= \sigma_g \sqrt{\frac{\pi}{2}} e^{x/2} \left\{(1-x)I_0(-x/2) - xI_1(-x/2)\right\}|_{x=-K} \\ &= \sigma_g \sqrt{\frac{\pi}{2}} e^{-K/2} \left\{(1+K)I_0(K/2) + KI_1(K/2)\right\}. \end{aligned}$$

□

Theorem 3 *Let $\{h(t)\}$ be the Rician process*

$$h(t) = e^{j2\pi f_D t}\{s_{\mathsf{LOS}} + g(t)\},$$

where $\{g(t)\}$ is a zero-mean, circular, Gaussian process with variance σ_g^2.

$$\frac{\mathsf{Var}[|h(t)|^2]}{E[|h(t)|^2]} = \frac{2K+1}{(K+1)^2}$$

Proof: The power in the fading envelope is denoted as

$$p_E = E[|h(t)|^2] = |s_{\mathsf{LOS}}|^2 + \sigma_g^2.$$

The variance of $\{|h(t)|^2\}$ is computed using the difference of the second moment and the square of the mean:

$$\begin{aligned}\mathsf{Var}[|h(t)|^2] &= E[(|h(t)|^2 - p_E)^2] \\ &= E[|h(t)|^4] - 2p_E E[|h(t)|^2] + p_E^2 \\ &= E[|h(t)|^4] - 2p_E^2 + p_E^2 \\ &= E[|h(t)|^4] - p_E^2.\end{aligned}$$

The fourth power expands as follows:

$$\begin{aligned}|h(t)|^4 &= |s_{\mathsf{LOS}}|^2\{|s_{\mathsf{LOS}}|^2 + |g(t)|^2 + 2\Re[s_{\mathsf{LOS}}\overline{g(t)}]\} \\ &\quad +|g(t)|^2\{|s_{\mathsf{LOS}}|^2 + |g(t)|^2 + 2\Re[s_{\mathsf{LOS}}\overline{g(t)}]\} \\ &\quad +2\Re[s_{\mathsf{LOS}}\overline{g(t)}]\{|s_{\mathsf{LOS}}|^2 + |g(t)|^2 + 2\Re[s_{\mathsf{LOS}}\overline{g(t)}]\}.\end{aligned}$$

The expectation zeros out the single terms of $\{g(t)\}$:

$$\begin{aligned}E[|h(t)|^4] &= |s_{\mathsf{LOS}}|^4 + |s_{\mathsf{LOS}}|^2\sigma_g^2 + 0 \\ &\quad +\sigma_g^2|s_{\mathsf{LOS}}|^2 + E[|g(t)|^4] + 0 \\ &\quad +0 + 0 + 4E[\Re[s_{\mathsf{LOS}}\overline{g(t)}]^2].\end{aligned}$$

The last term is computed by expanding into real and imaginary parts. Let $s_{\mathsf{LOS}} = s_X + js_Y$. Let $g(t) = x(t) + jy(t)$. Then

$$\Re[s_{\mathsf{LOS}}\overline{g(t)}] = \Re[(s_X + js_Y)(x(t) - jy(t))] = s_X x(t) + s_Y y(t).$$

The expected value of the square is

$$\begin{aligned}E\left[\Re[s_{\mathsf{LOS}}\overline{g(t)}]^2\right] &= E\left[(s_X x(t) + s_Y y(t))^2\right] \\ &= E\left[(s_X x(t))^2\right] + E\left[(s_Y y(t))^2\right] + 2E\left[s_X s_Y x(t)y(t)\right] \\ &= s_X^2\sigma_x^2 + s_Y^2\sigma_y^2 \\ &= |s_{\mathsf{LOS}}|^2\sigma_g^2/2.\end{aligned}$$

This result completes the computation of the fourth moment as

$$E[|h(t)|^4] = |s_{\mathsf{LOS}}|^4 + 4|s_{\mathsf{LOS}}|^2\sigma_g^2 + 2\sigma_g^4,$$

using the fourth moment of a Gaussian

$$E[|g(t)|^4] = 2\sigma_g^4.$$

The variance simplifies as the product of the specular and diffuse components:

$$\begin{aligned}\mathsf{Var}[|h(t)|^2] &= E[|h(t)|^4] - p_E^2 \\ &= |s_{\mathsf{LOS}}|^4 + 4|s_{\mathsf{LOS}}|^2\sigma_g^2 + 2\sigma_g^4 - (|s_{\mathsf{LOS}}|^4 + 2|s_{\mathsf{LOS}}|^2\sigma_g^2 + \sigma_g^4) \\ &= \sigma_g^4 + 2|s_{\mathsf{LOS}}|^2\sigma_g^2.\end{aligned}$$

Divide both sides of the equation by p_E^2 to get

$$\begin{aligned}\frac{\mathsf{Var}[|h(t)|^2]}{p_E^2} &= \frac{\sigma_g^4 + 2|s_{\mathsf{LOS}}|^2\sigma_g^2}{(|s_{\mathsf{LOS}}|^2 + \sigma_g^2)^2} \\ &= \frac{1+2K}{(K+1)^2}.\end{aligned}$$

□

B.3 RMS Bandwidth Moment

Theorem 4 *Let $\{g(t)\}$ be a zero-mean WSS harmonizable random process with covariance*

$$R_{gg}(\tau) = \int_{-\infty}^{\infty} e^{j2\pi f\tau} P_{gg}(f) df.$$

Assume the power spectrum of $\{g(t)\}$ is even: $P_{gg}(f) = P_{gg}(-f)$. Let $\{h(t)\}$ be the Rician process:

$$h(t) = e^{j2\pi f_D t}\{s_{\mathsf{LOS}} + g(t)\}.$$

An estimator for the RMS bandwidth f_{RMS} of Definition 2 is

$$\frac{R_{\dot{h}\dot{h}}(0)}{R_{hh}(0)} = 4\pi^2 f_D^2 + \frac{4\pi^2}{K+1} f_{\mathrm{RMS}}^2.$$

Proof: Lemma at $\tau = 0$

$$R_{\dot{h}\dot{h}}(0) = 4\pi^2 f_D^2 |s_{\mathsf{LOS}}|^2 + R_{\dot{g}\dot{g}}(0) + j2\pi f_D R_{g\dot{g}}(0) - j2\pi f_D R_{\dot{g}g}(0) + 4\pi^2 f_D^2 R_{gg}(0).$$

Lemma 2 computes

$$0 = R_{g\dot{g}}(0) = R_{\dot{g}g}(0)$$

because the power spectrum is even. Lemma 2 computes

$$R_{\dot{g}\dot{g}}(0) = 4\pi^2 f_N^2 \sigma_g^2$$

because the power spectrum is Gaussian. Consequently,

$$R_{\dot{h}\dot{h}}(0) = 4\pi^2 f_D^2 |s_{\mathsf{LOS}}|^2 + f_N^2 \sigma_g^2 + 4\pi^2 f_D^2 \sigma_g^2.$$

Divide by the envelope power $p_E = R_{hh}(0)$ to get

$$\begin{aligned}\frac{R_{\dot{h}\dot{h}}(0)}{R_{hh}(0)} &= 4\pi^2 f_D^2 + 4\pi^2 f_N^2 \frac{\sigma_g^2}{|s_{\mathsf{LOS}}|^2 + \sigma_g^2} \\ &= 4\pi^2 f_D^2 + 4\pi^2 f_N^2 \frac{1}{K+1}.\end{aligned}$$

□

C Propagation: theory and measurements

This section compares transmission loss estimated from the over-the-air measurements against selected propagation codes:

- Booker-Lagannina [12],
- FCCGW [28],
- EMP73 [39],
- LFMFSmoothEarth [33],
- AREPS [47].

Comparisons are limited for two reasons. First, estimating transmission loss from the over-the-air measurements requires calibrated antennas. Second, the surface-wave propagation codes require sea-surface information and terrain information for propagation from the elevated shore-based transmitter.

The first difficulty with comparisons is the received power model. The simplest transmission loss model assumes the received power p_R is the product of the transmitted power p_T, the transmitter's antenna gain g_T, the receiver's antenna gain, g_R and the channel $|h|^2$ as

$$p_R = p_T \, g_T \, g_R \, |h|^2,$$

where frequencies and headings are omitted for brevity, vertical polarization is assumed, antenna gain subsumes the matching loss, and the cable loss is omitted. The channel gain is estimated as

$$|h|^2 = \frac{p_R}{p_T g_T g_R}. \tag{29}$$

Figure 4 shows the reciprocal of this channel gain is the *Basic Transmission Loss*. At least three problems arise when applying Equation 29 to the channel measurements:

CM-1 The effect of the ship's heading is unknown,

CM-2 On-site antenna patterns are not are available,

CM-3 The antenna systems are not calibrated.

The over-the-air measurements have limited duration so that CM-1 effects are mitigated. Estimated antenna patterns provide an approximate solution to CM-2. However, calibration requires extending Equation 29 to encompass the full TX→RX chain as shown in Figure 4. That figure shows the transmitter and receiver connect to boxes labeled "circuit losses". These boxes include the antenna matching circuits, the TX and RX circuitry, and amplifiers. If g_{CAL} denotes these circuit gains, the received power is

$$p_R = p_T \, g_T \, g_R \, g_{\mathsf{CAL}} \, |h|^2. \tag{30}$$

Consequently, the uncalibrated system estimates

$$g_{\mathsf{CAL}}|h|^2 = \frac{p_R}{p_T g_T g_R}. \tag{31}$$

Although absolute power comparisons are not possible, Equation 31 does shows relative power comparisons between different frequencies at the same range are possible:

$$|h(r, f_1)|^2 - |h(r, f_2)|^2 = g_{\mathsf{CAL}}|h(r, f_1)|^2 - g_{\mathsf{CAL}}|h(r, f_2)|^2 \quad [\text{dB}], \tag{32}$$

provided g_{CAL} does not vary with frequency. Other HF calibrations show g_{CAL} varies a few dB with frequency. Therefore, Equation 32 approximates relative power comparisons within a few dB.

The second difficulty with comparisons is knowing credible physical parameters used by the surface-wave codes, either explicitly or implicitly:

- seawater dielectric,
- sea-surface roughness,
- mixed paths,
- antenna models.

The surface-wave codes assume short, identical, vertical monopoles placed on the sea surface. In contrast, the experiment transmitted from a 41-foot vertical monopole operating in low-angle mode mounted on the roof a four-story building set 371 feet above the ocean. The receive antenna was a 10-foot vertical monopole approximately 20 feet above the ocean. These mismatches between the physical experiment and the propagation codes guarantee differences between measurements and theory.

Organization: Section C.1 models the transmit antenna gain g_T from the manufacturer's data sheet. Section C.2 estimates the receive antenna gain g_R from a theoretical model. Both antenna models show gain rapidly decreases as frequency decreases making channel estimates are sensitive to modeling errors (See Equation 31). Sections C.3 and C.4 report the some surface-wave codes deliver relatively good comparisons between theory and measurements—assuming low salinity. Section C.5 sets out the problematic history of the surface-wave theory, lists minimal requirements to compare surface-wave theory to surface-wave codes, and concludes by discussing propagation codes relevant for computing the entire ensemble of HF paths—ground waves, surface waves, and skywaves—such as the *Variable Terrain Radio Parabolic Equation (VTRPE)* [55].

C.1 Transmit Antenna Modeling

The transmitter employed the TCI Model 619 antenna mounted on the northwest corner atop Building 40, NIWC, Pacific. Table 17 lists the directive gain g_D and the efficiency η of this antenna operated in low-angle mode from the data sheet. The roof-top effects are not included. The transmitter antenna's gain g_T is modeled from Table 17 as

$$g_T = g_D + \eta \quad [\text{dBi}].$$

Table 17: TCI Model 619; low-angle mode [68].

Frequency (MHz)	Directive Gain (dBi)	Efficiency (dB)
2	4.8	−19.7
4	4.9	−6.9
10	5.6	−1.0
16	6.8	−2.8
28	7.1	−2.4

Figure 112 shows one estimate of g_T obtained by spline interpolation of Table 17. The gain rapidly decreases once the frequency drops below 8 MHz.

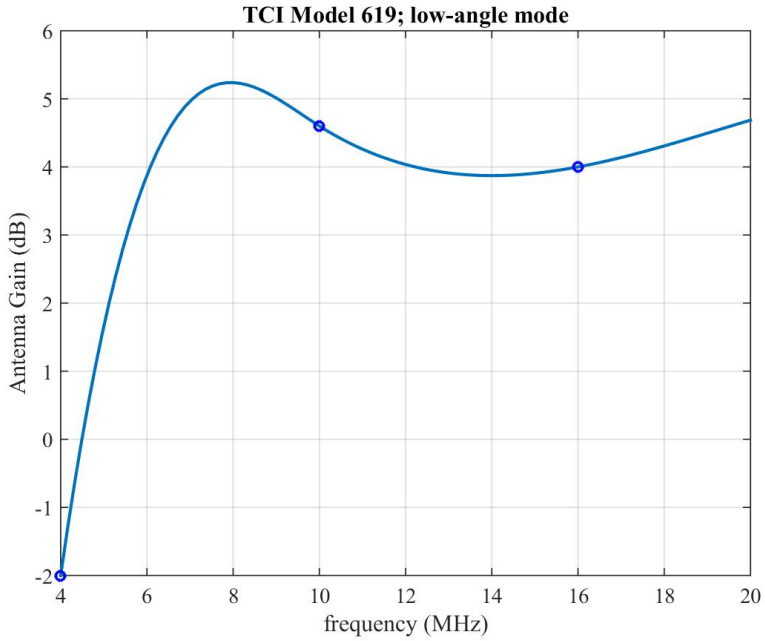


Figure 112: TCI Model 619 antenna gain; interpolated from Table 17.

C.2 Receive Antenna Modeling

The receive antenna is located on the ship behind the wheel-house (See Figure 12). Although this location modifies the antenna pattern, the receive antenna is modeled as a monopole with impedance z_M [40]:

$$g_R = 1 - |s_M|^2; \quad s_M = \frac{z_M - z_0}{z_M + z_0}; \quad z_0 = 50 \text{ [ohms]},$$

ignoring mismatch. The monopole's impedance z_M is half that of a dipole's impedance z_D:

$$z_M = \frac{1}{2} z_D; \quad z_D = 5(\mathsf{k}\ell_D)^2 - j120 \frac{\log(\ell_D/a_W)}{\tan(\mathsf{k}\ell_D)},$$

where $\mathsf{k} = 2\pi\lambda^{-1}$ is the wavenumber, a_W is the wire radius, and ℓ_D the dipole's length that is twice the length of the monopole, The monopole on the ship is estimated to be approximately 10 feet tall with a 1-inch wire diameter so that:

$$\begin{aligned} \ell_D &= 20 \quad \text{[feet]} \\ a_W &= 0.5 \quad \text{[inches]} \end{aligned}$$

Figure 113 plots this theoretical monopole gain from 1 to 20 MHz. The figure shows the first resonance at 12.52 MHz. The sensitivity of estimating propagation loss by dividing by the gain is shown by the gain dropping 50 dB as frequency decreases from 12 MHz to 4 MHz.

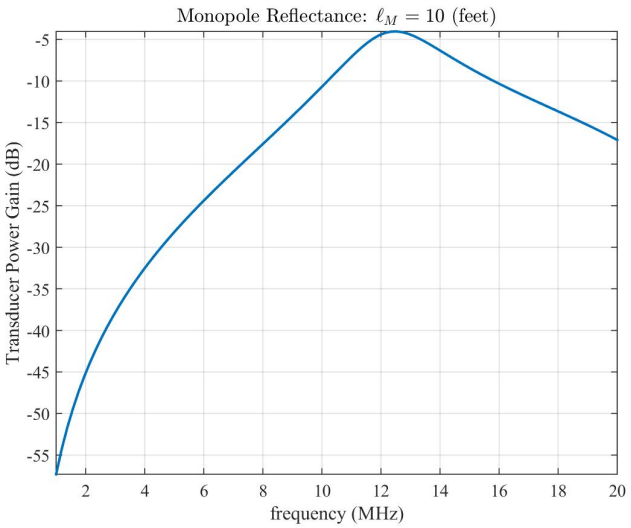


Figure 113: Shipboard receive antenna gain; monopole model.

C.3 05-June-2020

This section compares the *measured* propagation loss on 05-June-2020 against the following *surface-wave codes*:

- LFMFSmoothEarth,
- Booker-Lagannina,
- AREPS.

Section C.3.1 introduces the LFMFSmoothEarth code obtained from the ITU [33]. This model reports the best fit to the measured propagation loss. Section C.3.2 introduces the Booker-Lugannani model extracted from [12]. This model approximates Barrick's analysis for propagation over a smooth earth [7]. Rough-surface loss is included by using an ocean-wave spectrum that is a function of wind speed. Using this model with the 10-knot wind did not align with the measured propagation loss. Section C.3.3 discusses NIWC's *Advanced Refractive Effects Prediction System* (AREPS) [47]. This code approximates the 2-D electric field using split-step parabolic equation methods. The code includes terrain from *Digital Terrain Elevation Data* (DTED) with surface dielectrics. Despite including the terrain and slicing the electric field at the receiver's antenna height, AREPS did not align with the measured propagation loss.

C.3.1 LFMFSmoothEarth

This section compares the *measured* propagation loss to the LFMFSmoothEarth *predictions* assuming the following [33]:

- Smooth homogeneous spherical Earth,
- Troposphere's refractive index decreases linearly with height,
- Transmitting and receiving antennas on or near the Earth's surface,
- Transmitter uses a short vertical monopole on the surface of a perfectly conducting plane Earth.

Figure 114 compares the relative Day 05 measurements (circles) to the predictions (curves). The antennas are not calibrated so the measured ensemble is located *relative* to the 4.23 MHz curve at 160 km using Equation 32. Although the measurements shows a good fit at 12.45 MHz, too little loss is predicted at 8.456 MHz.

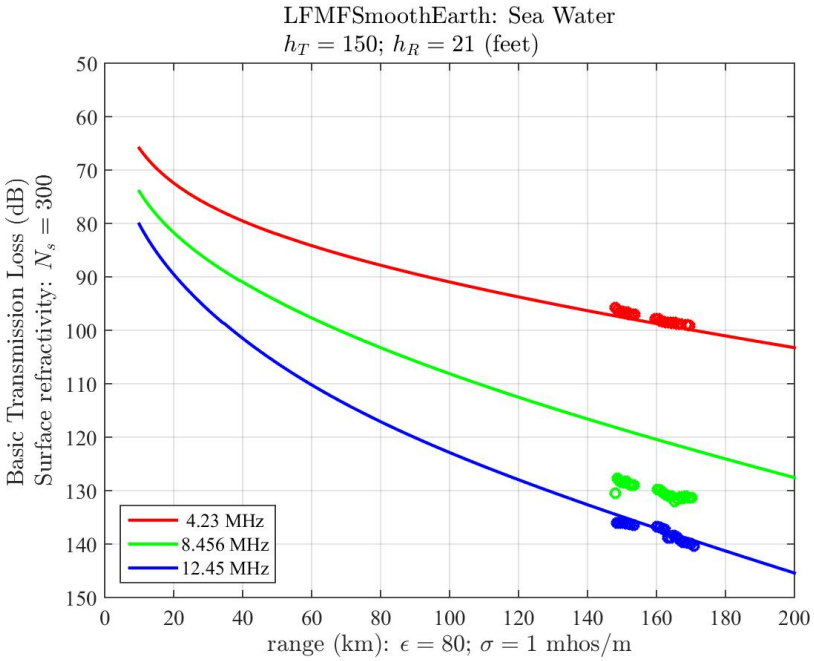


Figure 114: Comparing LFMFSmoothEarth (curves) to relative Day 05 measurements (circles).

Remarks: (*i*) Antenna heights are limited to 150 feet for this model. (*ii*) Surface reactivity ranges from 250 in dry air $< Ns <$ about 400 in extremely humid air. This simulation uses $N_s = 300$. (*iii*) This model used a low-salinity ocean with $\sigma = 1$ mhos/m from [33, Fig. 1].

C.3.2 Booker-Lugannani

This section compares the *measured* propagation loss to the propagation loss *predicted* by the Booker-Lugannani model [12]:

$$L_g(f,r) = L_g^{(1)}(f,r) + L_g^{(2)}(f,r) \quad [\text{dB}]. \tag{33}$$

This model approximates Barrick's model [7] assuming

- Homogeneous spherical Earth,
- Lossy ocean with $\sigma = 4$ mhos/meter conductivity,
- Transmitter and receiver are vertical monopoles located on the ocean surface,
- Phillips Isotropic Ocean-Wave spectrum models the rough surface propagation.

The error incurred by locating the antennas on the ocean surface is bounded as follows [12]:

> The maximum error incurred as a consequence of this assumption is approximately 3% ([7]) and is worth tolerating in view the attendant simplicity (viz, it is not necessary to specify the heights of the transmitter and receiver).

The first term in Equation 33 models the loss along a path of length r_{km} over a smooth, curved, lossy surface at frequency f_{MHz} as [12, Eq. 22]

$$\begin{aligned} L_g^{(1)}(f,r) &= 20\log_{10}\left(\frac{2\pi r_{\mathsf{km}} f_{\mathsf{MHz}}}{0.3}\right) + C_1(f_{\mathsf{MHz}}) r_{\mathsf{km}}^{C_2(f_{\mathsf{MHz}})} \quad [\text{dB}], \\ C_1(f_{\mathsf{MHz}}) &= 1.78\cdot 10^{-4} \times f_{\mathsf{MHz}} \times \exp\left(1.40\cdot 10^{-8} \times f_{\mathsf{MHz}}^5\right), \\ C_2(f_{\mathsf{MHz}}) &= 1.83 \times f_{\mathsf{MHz}}^{-0.243}. \end{aligned} \tag{34}$$

The first term of Equation 34 models the free-space spreading gain g_F for vertical monopoles over a smooth, flat, perfectly conducting surface as [37]:

$$g_F = \left(\frac{\lambda}{2\pi r}\right)^2.$$

Logan and Rockway make explicit free-space spreading gain errors arise when dipoles and monopoles are conflated [37]. Figure 115 compares the relative Day 05 measurements (circles) to $L_g^{(1)}(f,r)$'s predictions (curves). The antennas are not calibrated. Placing the 4.23 MHz measurements on the 4.23 MHz curve at (See

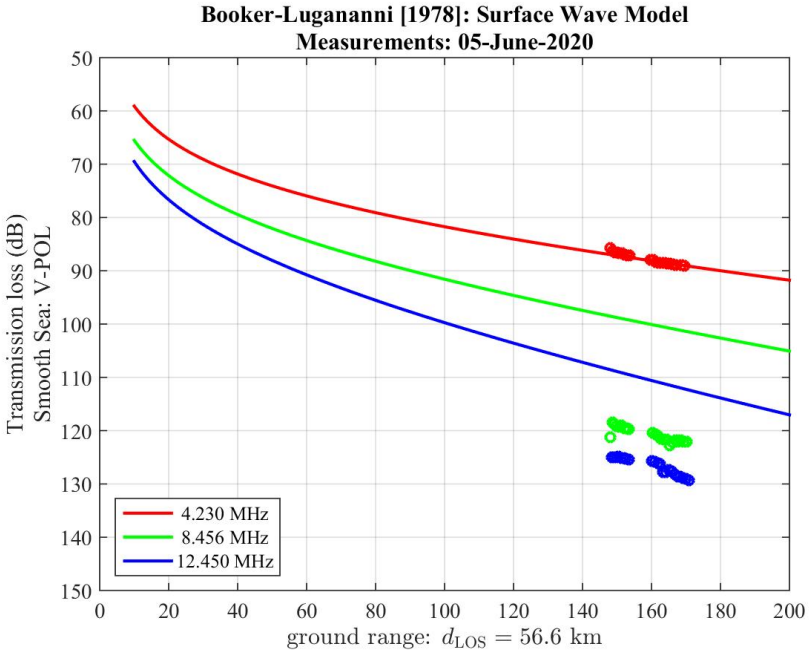


Figure 115: Comparing $L_g^{(1)}(f, r)$ predictions (curves) to Day 05 measurements (circles).

Equation 32) and sets the *relative* level of the 8.456 and 12.45 MHz measurements. This relative placement shows $L_g^{(1)}(f, r)$'s predictions have too little loss compared to the measurements at 8.456 and 12.45 MHz.

Equation 33 includes additional loss in $L_g^{(2)}(f, r)$ caused by propagation over a rough sea surface. Modeling this loss employs ocean-wave spectrums. Booker-Lugannani selected the Phillips spectrum. Numerical computation of $L_g^{(2)}(f, r)$ using the Phillips spectrum is evaded by interpolating Barrick's plots [7]. Figure 116 compares $L_g^{(2)}(f, r)$ caused by a 10-knot wind (Sea State 2) at 4.23, 8.456, and 12.45 MHz. As a function of range, the loss at 4.23 MHz decreases while 8.456 and 12.45 MHz show increasing loss. However, this Phillips spectrum only increases loss by a few dB and cannot overcome the 10-dB mismatch between theory and measurements. For comparison, Figure 117 shows the loss caused by the Neumann-Pierson spectrum. As with the Phillips spectrum, the additional loss caused by a 10-knot wind is only a few dB.

Remarks: (*i*) Sea-surface conductivity of 4 mhos/meter is "baked" into $L_g^{(1)}(f, r)$. Decreasing conductance increases transmission loss. (*ii*) Increasing wind speed increases transmission loss. Although a 30-knot wind better matches theory and measurements, this Sea State 6 has a wave heights ranging from 9 to 12 feet [7]. Such waves were not observed in the experiments.

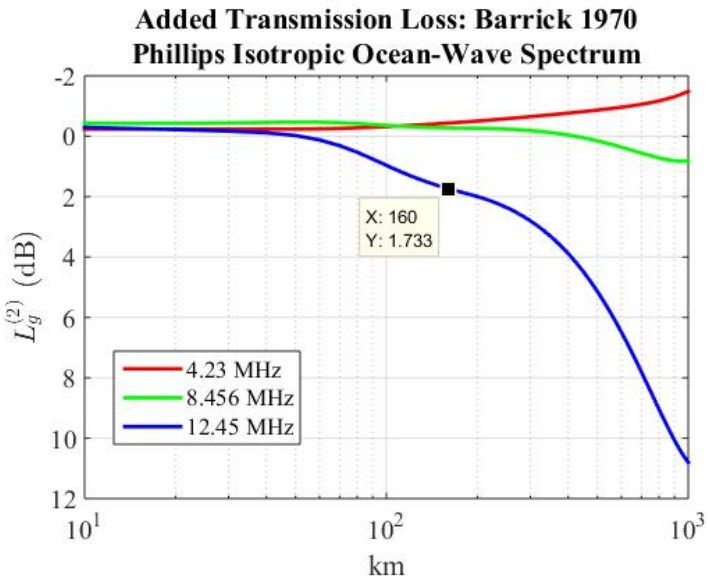


Figure 116: Additional transmission loss $L_g^{(2)}(f, r)$ caused by the rough ocean surface; Phillips spectrum.

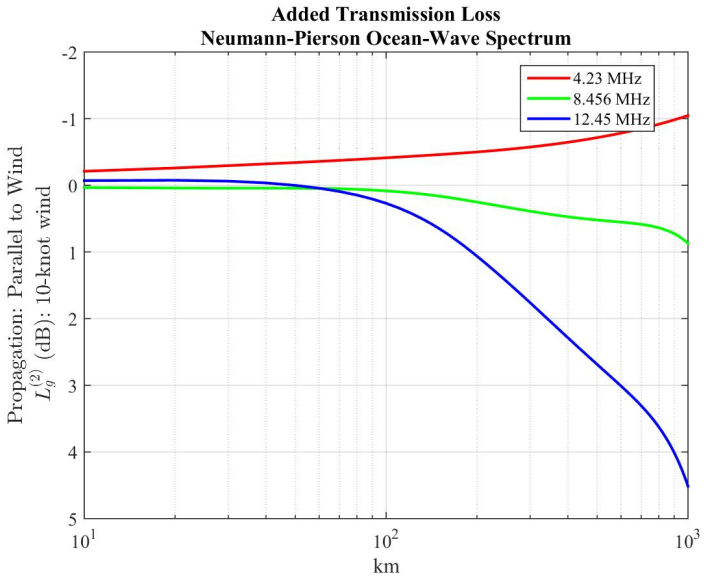


Figure 117: Additional transmission loss $L_g^{(2)}(f, r)$ caused by the rough ocean surface; Neumann-Person spectrum; direction of propagation is parallel to the wind.

C.3.3 AREPS

The preceding codes only model surface-wave propagation from vertical monopoles attached to the ocean surface and do not offer a ready extension encompassing mixed paths (e.g., starting from elevated terrain and propagation out to sea). One alternative to this limited modeling are the wave-equation solvers that approximate the electric field above the earth's surface.

One class of wave-equation solvers are the split-step parabolic equation methods, such as NIWC's *Advanced Refractive Effects Prediction System* (AREPS) [47]. Figure 118 illustrates the 2-D propagation predicted by AREPS. The circular inset shows the propagation along the line starting from a transmitter located on Building 40, NIWC-Pacific and heading south at 248.9° azimuth. The 2-D propagation loss along that line is a function of range and altitude. AREPS includes terrain from the *Digital Terrain Elevation Data* (DTED). The terrain shows the propagation starting from Building 40, traveling over Point Loma, and extending into the ocean.

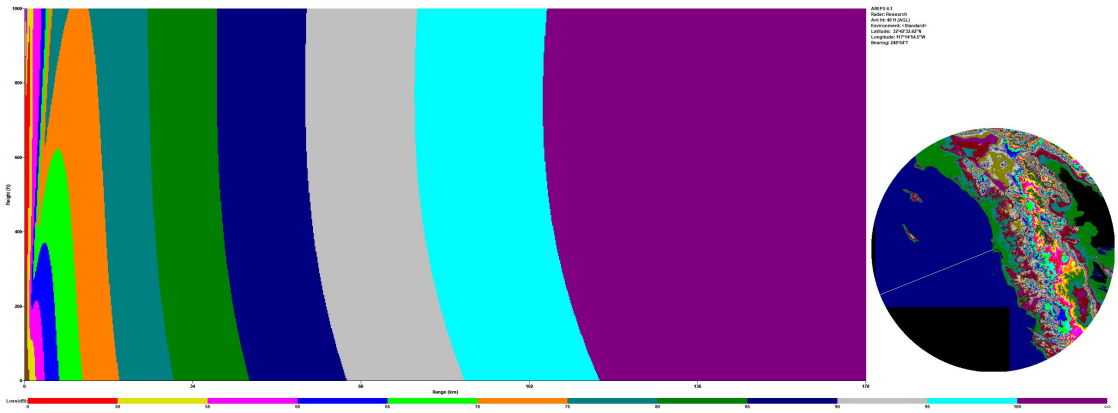


Figure 118: AREPS propagation loss at 12.450 MHz along 248.9° azimuth from the transmitter located on Building 40, NIWC.

AREPS is limited to troposphere propagation. Although AREPS includes the direct, reflected, and surface waves, mixed paths and terrain, the ionosphere is not in AREPS. Therefore, HF propagation only modeled near the surface—there are no skywaves.

Sampling this propagation at the receive antenna height ostensibly captures the direct, reflected, and surface waves out to the horizon, and the surface wave past the horizon. The ship's platform and heading effects are not modeled. This AREPS simulation employed a zero-gain isotropic antenna at the transmitter and an equivalent receive antenna by measuring the electric field. Figure 119 presents the transmission loss curves at 4.23, 8.456, and 12.45 MHz. The spacing of these propagation curves matches the Booker-Lugannani model. As such, these curves do not match the measured transmission losses—despite relative scaling—so the measurements are not plotted.

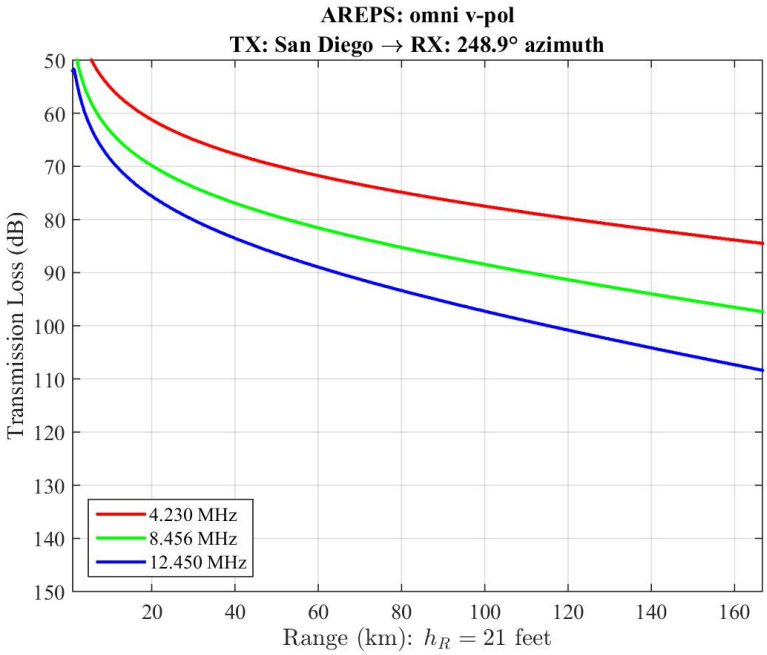


Figure 119: AREPS transmission loss along 248.9° azimuth starting from the transmitter located on Building 40, NIWC to a shipboard receive antenna $h_R = 21$ feet above the sea surface.

Remarks: (*i*) Varying sea-surface conductivity had little effect on transmission losses at the different frequencies. (*ii*) The ionosphere is not included in these simulations. (*iii*) VTRPE is another parabolic equation code that does include terrain, rough-surface scattering on the sea surface, antenna types, platform effects, and the ionosphere. VTRPE is discussed in Section C.5.

C.4 06-June-2020

This section compares the propagation loss *measured* on 06-June-2020 against the *predictions* produced by the following surface-wave models:

- LFMFSmoothEarth,
- FCCGW.

Section C.4.1 reports the LFMFSmoothEarth code, obtained from the ITU [33]. Using the same curves from Day 05, this code provides a relatively good fit to the measured propagation loss. Section C.4.2 introduces the FCCGW code obtained from [12]. This code implements a similar propagation method as LFMFSmoothEarth code but restricts the antennas to surface—there is no option for elevated antennas.

C.4.1 LFMFSmoothEarth

Figure 120 compares the transmission losses predicted by the LFMFSmoothEarth code to the measured transmission losses on Day 06. The predicted curves are the same as Day 05—this model does not include the day-to-day variability of the rough-surface scattering. The measurements at 4.23 and 8.456 MHz are similar to the measurements on Day 05. The variability at 12.45 MHz is not understood.

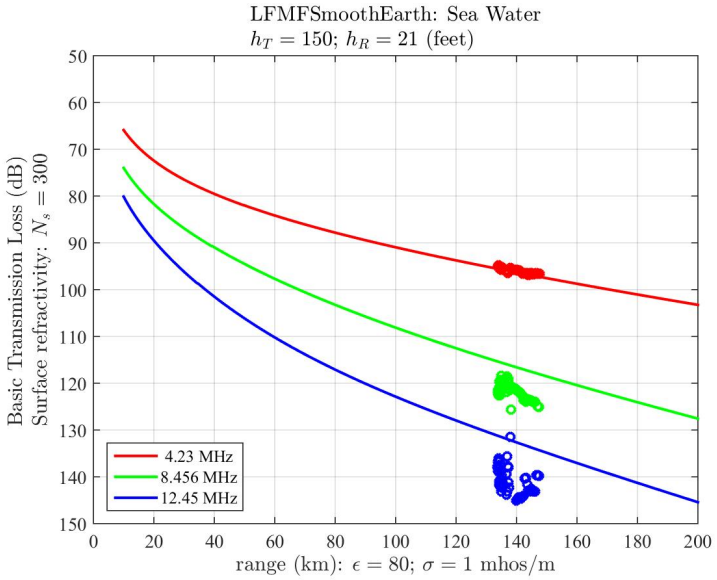


Figure 120: Comparing LFMFSmoothEarth (curves) to relative Day 06 measurements (circles).

C.4.2 FCCGW

The FCCGW code assumes [28]:

- Smooth spherical earth with an effective radius 4/3 larger than actual,
- Uniform dielectric constant and conductivity,
- Transmitting and receiving antennas on the surface of the earth.

The FCCGW code implements Norton's model with the distinction between the reflecting region and the diffraction region [43]. This code is likely subsumed by the LFMFSmoothEarth code where the latter admits elevated antenna heights. Figure 121 compares the transmission losses predicted by FCCGW and the measured transmission losses. Although both codes use the same conductivity $\sigma = 1$ S/m, LFMFSmoothEarth *sets* relative permittivity to $\epsilon = 80$ while FCCGW *computed* $\epsilon = 79.6441$ from the frequency, ocean temperature, ocean salinity, and atmospheric pressure.

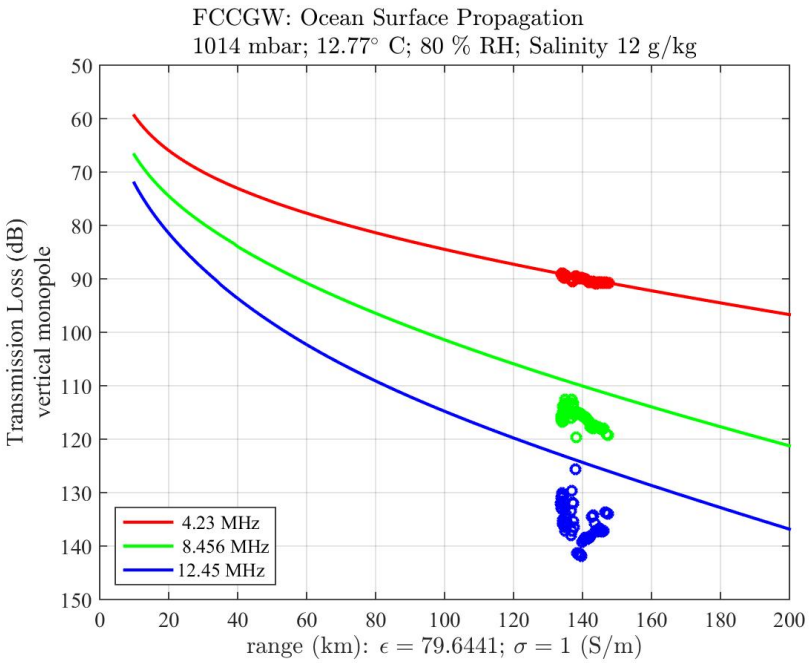


Figure 121: Comparing FCCGW (curves) to Day 06 measurements (circles).

Remarks: (*i*) Both codes derive from Barrick's model and employed almost identical ocean-wave dielectrics. (*ii*) Modeling antenna heights varied transmission loss by a few dB. (*iii*) The ionosphere is not included in these simulations. (*iv*) The sea surface is not included in these simulations.

C.5 Reconciling Theory and Measurements

This section starts with surface wave's problematic history to temper comparisons between the surface-wave codes and the measurements. Eckert presents a historical review documenting decades of errors in surface-wave analysis (references specific to [28]):

> Curves prepared by Rolf [13] in 1930 were based on promising theory but were actually misleading. Rolf relied on theoretical results published in 1909 by the physicist Arnold Sommerfeld [14], and these early results contained an error. Correct expressions for the field of an antenna over a flat earth had been worked out before 1930 by Sommerfeld himself as well as others, but disagreement with the 1909 result had not been noticed. Rolf used the earlier result thereby creating confusion. For a time, measurements like those in the Kirby and Norton report [15] were presented in relation to the Rolf curves although agreement was poor. It was five years before the error in the theory of Rolf's graphs was identified [16]. It was still later that an experiment was conducted conclusively showing the theory to be wrong [17].

Eckert's review is a cautionary tale for comparing theory and measurements and supports the following observation:

> *If theory and measurements do not agree, assume both are flawed.*
> Dr. John Meloling.

Consequently, this final section points out limitations in the channel-sounding measurements and the propagation codes to avoid erroneous comparisons. Comparisons are based on extracting the channel gain from the channel-sounding measurements assuming Equation 30 (repeated for convenience):

$$p_R(f,r) = p_T \cdot g_T(f) \cdot g_R(f) \cdot g_{\mathsf{CAL}} \cdot |h(f,r)|^2$$

with the assumptions

- Transmitter's power p_T does not vary with frequency,
- Calibration gain g_{CAL} does not vary with frequency,
- Antenna gains are independent of azimuth at zero elevation (CM-1),
- Transmit antenna gain $g_T(f)$ is well-modeled from the data sheet (Section C.1),

- Receive antenna gain $g_R(f)$ is well-modeled by the monopole model (Section C.2).

Because the antennas are not calibrated, so that only relative comparisons are possible as reported in Sections C.3 and C.4. These relative comparisons show measurements align with LFMFSmoothEarth and FCCGW codes using ocean surface conductance $\sigma = 1$ S/m that corresponds to low salinity. However, these codes do not model attenuation caused by a rough sea surface. The Booker-Lugannani code models surface-wave loss as the sum of the smooth earth loss and the rough surface loss [12]:

$$L_g(f,r) = L_g^{(1)}(f,r) + L_g^{(2)}(f,r) \quad [\text{dB}].$$

The smooth-earth loss $L_g^{(1)}(f,r)$ *fixes* ocean surface conductance at $\sigma = 4$ S/m. This loss had a worse fit to the measurements than LFMFSmoothEarth and FCCGW codes. The rough-surface losses $L_g^{(2)}(f,r)$ do increase loss with increasing sea state. The rough-surface losses improved the fit using Sea State 6 that corresponds to 9 to 12-foot waves—not observed during these experiments

Conclusions: (*i*) Measured and predicted transmission losses agreed with the ordering of the frequencies. (*ii*) Tweaking sea-surface codes to fit measurements is not a fruitful approach to reconcile theory and measurements. (*iii*) Credible comparisons require both end-to-end calibration (See Figure 4) and surface-wave codes with on-site geophysical observations.

Recommendations: The surface-wave codes listed in this report are limited to vertical monopoles attached to the sea surface [23]. Upgrades to the surface-wave codes include:

- Include *Digital Terrain Elevation Data* (DTED) with surface dielectrics to support ship-to-shore operations; Experimental costs and complexity are reduced using shore sites.
- Coupling between the antenna and surface wave includes antenna, platform, and terrain.
- Update codes with recent sea-surface spectrum [49], [54], [76].

However, the surface-wave channel is only one component of the HF channel. Norton's definition (See Section 1) excluded skywaves from the surface wave channel. The experiments include the surface wave and skywaves (See Section 4.3). Therefore, the last section discusses the necessity of modeling the entire HF channel—surface waves, ground waves, and skywaves—including antenna platforms coupling the HF environment.

C.6 The Surface Wave in Context

Section 1 pointed out that the surface wave is only one component of the HF channel. This section shows the surface wave in context in the entire HF channel. Figure 122 starts the discussion with a 2-D slice of surface-wave's diffraction over a smooth earth. The incident ray travels from the transmitter and hits the surface at the point of attachment Q_1 to generate the surface wave. This surface wave propagates *along* the surface while shedding rays *tangent* to the surface. The point of detachment Q_2 shows its tangent ray traveling to the receiver. The next figure puts this surface-wave schematic in the entire HF channel.

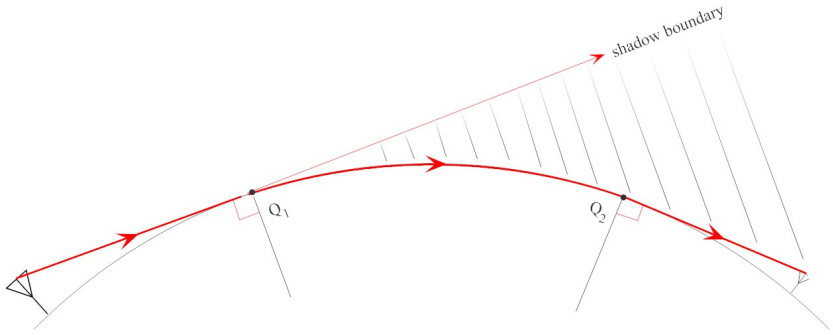


Figure 122: Surface-wave diffraction from an incident ray.

Figure 123 is a 2-D slice of the HF channel simulated by VTRPE [56]. The simulation shows the HF propagation from an NVIS antenna transmitting San Diego, CA. The vertical slice is cut along the azimuth due East at 05:00 06-Jul-1998 local time assuming sunspot index is 100. The transmitter's antenna is horizontally polarized and 25 meters above sea level. The antenna is assigned a 70° keyhole pattern steered to 45° at 8 MHz. The figure is dominated by the skywave showing:

- One skywave component radiates into space,
- A second skywave component refracts from the ionosphere to illuminate the surface 450 kilometers downrange.

Although the antenna's pattern dominates the propagation, the lower edge of the pattern shows the shadow boundary and a surface wave propagating to nearly 150 km.

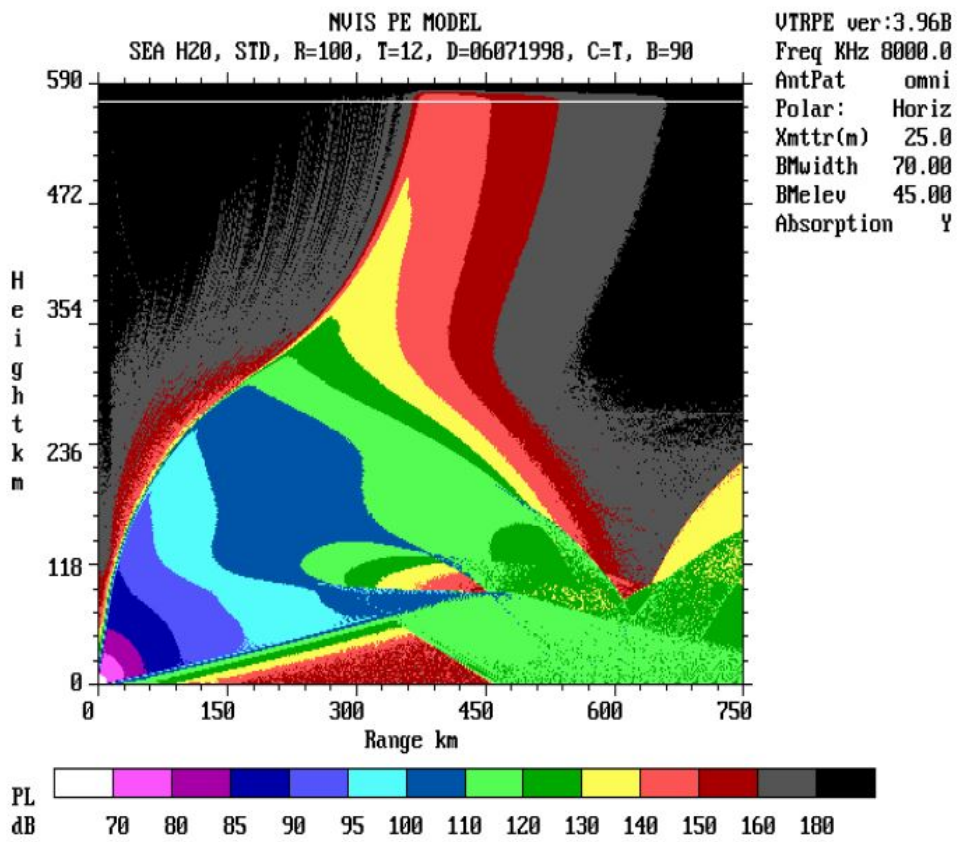


FIG. 6. NVIS-2

Figure 123: HF propagation at 8 MHz; keyhole antenna (Permission courtesy of Frank Ryan [56]).

This figure puts the surface-wave in context and points to following gaps limiting HF communications between the transmitter and a ground-level receiver: (*i*) The surface wave is limited to 150 km, (*ii*) the skywaves arrive 450 km downrange, (*iii*) A skip zone is forced between the surface wave channel and the skywave channel.

Conclusions: Employ VTRPE to understand the surface wave's domain of application and the limitations of the entire HF channel.